SANDIA REPORT
SAND2019-0727x
Unlimited Release
Printed mm 201x

Geotechnical Concerns of Bayou Choctaw Strategic Petroleum Reserve and Explanations

Byoung Yoon Park

Prepared by
Sandia National Laboratories
Albuquerque, New Mexico 87185 and Livermore, California 94550

Sandia National Laboratories is a multimission laboratory managed and operated by National Technology and Engineering Solutions of Sandia, LLC, a wholly owned subsidiary of Honeywell International, Inc., for the U.S. Department of Energy's National Nuclear Security Administration under contract DE-NA0003525.

Issued by Sandia National Laboratories, operated for the United States Department of Energy by National Technology and Engineering Solutions of Sandia, LLC.

Available to DOE and DOE contractors from

U.S. Department of Energy
Office of Scientific and Technical Information
P.O. Box 62
Oak Ridge, TN 37831

Telephone: (865) 576-8401
Facsimile: (865) 576-5728
E-Mail: reports@osti.gov
Online ordering: http://www.osti.gov/scitech

Available to the public from

U.S. Department of Commerce
National Technical Information Service
5301 Shawnee Rd
Alexandria, VA 22312

Telephone: (800) 553-6847
Facsimile: (703) 605-6900
E-Mail: orders@ntis.gov
Online order: http://www.ntis.gov/search

SAND2019-0727x
Printed mmmm 2019
Unlimited Release

Geotechnical Concerns of Bayou Choctaw Strategic Petroleum Reserve and Explanations

Byoung Yoon Park

Geotechnology & Engineering (Org. 8862)
Sandia National Laboratories
P.O. Box 5800
Albuquerque, NM 87185-MS0751

Abstract

Geotechnical concerns arise due to the close proximity of the some of the caverns to each other (e.g., Caverns 15 and 17) or to the edge of the salt dome (e.g., Cavern 20). There are nine abandoned caverns, one of which collapsed (Cavern 7) in 1954 and another (Cavern 4) which is believed to be in a quasi-stable condition. This report provides explanations for these geotechnical concerns. The structural integrity of the pillar between BC-15 and 17 is examined. No salt fall is expected through 2045. However, the dilatant damaged area increases with time, especially, at the chimney area of BC-17. One drawdown leach for both caverns could be allowed if they are normally operated as a gallery, depressurized simultaneously. The possibility of a loss in integrity of BC-20 is examined in the salt between the dome edge and the cavern. The edge pillar is predicted to have experienced tensile stress since September 1999, but the small tensile stressed area is predicted to disappear in 2018 because BC-20 is filled fully with brine rather than oil since 2/7/2013. Even though BC-20 is no longer used as an SPR cavern, we need to continue monitoring the cavern integrity. BC-4 is also currently filled with brine and will not hold pressure at the wellhead. The cavern extends upward into the caprock and has no effective salt roof. The results indicate that any sort of caprock roof collapse for BC-4 is not imminent but salt falls will likely occur from the near-roof portions of the cavern. The uncertainty due to salt falls illustrates the importance of continued monitoring of the area around BC-4 for behavior such as subsidence and tilt which may indicate a change in the cavern's integrity status.

ACKNOWLEDGMENTS

This research is funded by SPR programs administered by the Office of Fossil Energy of the U.S. Department of Energy.

The author would like to thank Steven R. Sobolik and Courtney G. Herrick of Sandia provided technical reviews. Barry Roberts of Sandia provided the seismic and sonar data for meshing the dome and caverns. Project manager Anna C. Snider Lord of Sandia supported this work. As always, the support of Diane Willard and Wayne Elias of DOE is greatly appreciated. Paul Malphurs of DOE also is greatly appreciated, as is his comprehensive review of this report. This report has been improved by these individuals.

CONTENTS

FIGURES

TABLES

NOMENCLATURE

3D	Three-Dimensional
BC	Bayou Choctaw
BC-4	Bayou Choctaw Cavern 4
BC-15	Bayou Choctaw Cavern 15
BC-17	Bayou Choctaw Cavern 17
BC-20	Bayou Choctaw Cavern 20
BH	Big Hill
CGZ	Clay and Gypsum Zone
DF	Dilatant Damage Factor
DOE	U.S. Department of Energy
EFF	Extended File Format
E-W	East-West
FE	Finite Element
GAZ	Gypsum-Anhydrite Zone
ID	Identification
M-D	Multi-Mechanism Deformation
MIT	Mechanical Integrity Test
MMB	Million Barrels
MVS	Mining Visualization System
LADNR	Louisiana Department of Natural Resources
N-S	North-South
OBI	Oil-Brine Interface
ONI	Oil-Nitrogen Interface
PLC	Power Law Creep
Sandia	Sandia National Laboratories
SPR	Strategic Petroleum Reserve
UTP	Union Texas Petroleum
WH	West Hackberry

Intentionally Blank

1. INTRODUCTION

1.1. Background

The U.S. Strategic Petroleum Reserve (SPR) stores crude oil in 60 caverns located at four sites located along the Gulf Coast. Most of the caverns were solution mined by the U.S. Department of Energy (DOE) and are typified as cylindrical in shape. In reality, the geometry, spacing, and depths of the caverns are irregular. Sandia National Laboratories (hereafter 'Sandia'), on behalf of DOE, is evaluating the mechanical integrity of the salt surrounding existing petroleum storage caverns in the Bayou Choctaw (BC) Salt Dome in Louisiana.

Geotechnical concerns arise due to the close proximity of the some of the caverns to each other (e.g., Caverns 15 and 17) or to the edge of the salt dome (e.g., Cavern 20) [Park et al. 2006]. In addition to the SPR caverns at BC, eight other caverns exist which store various hydrocarbons and are operated by private industry. Also, there are nine abandoned caverns, one of which collapsed (Cavern 7) in 1954 and another (Cavern 4) which is believed to be in a quasi-stable condition. The integrity of wellbores at the interbed between the caprock and salt is another concern because oil leaks occurred at the interbed in the Big Hill site [Park, 2014]. When oil is withdrawn from a cavern in salt using freshwater, the cavern enlarges. As a result, the pillar separating caverns in SPR fields is reduced over time due to usage of the reserve. The enlarged cavern diameters and smaller pillar web thicknesses reduce underground stability [Park and Ehgartner, 2011]. It is necessary to establish a limit for the remaining pillar thickness between caverns without threatening the structural integrity of the caverns.

1.1.1. BC-15 and 17

Bayou Choctaw Caverns 15 and 17 (BC-15 and 17) have a thin web between them, which has been the subject of several geomechanical studies over the lifetime of the project. The thin web requires that the caverns are operated as a gallery, depressurized simultaneously in order to prevent unintended breaching of the walls and uncontrolled coalescence of the caverns. These caverns are designated yellow category 2 because they can be drawn down, but require special treatment during workover [Lord et al., 2013]. Dilatant damage is predicted to occur at approximately three quarters-height of BC-15 in the web salt after the second drawdown leach (using the RESPEC dilatancy criterion for Cayuta salt [DeVries et al., 2003]). The damaged zone widens through five drawdown leaches. Once dilatant damage occurs on the walls of BC-15 and BC-17 after the second drawdown leach, the damaged zone continues to grow across the pillar. Therefore, the pillar may fail entirely after the second drawdown leach [Park and Ehgartner, 2011]. Only the first drawdown is predicted to occur without negative effects for the pillar between BC-15 and BC-17. Therefore, additional analyses considering the cavern geometries obtained from sonar surveys should be assessed before conducting the first drawdown leach.

1.1.2. BC-20

Bayou Choctaw Cavern 20 (BC-20) is located near the edge of the salt dome (Figure 1). Its proximity close to the edge of the dome raises concerns about potential tensile failure in the surrounding rock near BC-20 induced by the cavern volume closure due to salt creep. The location of BC-20 in the salt dome is similar to the cavern involved in the Bayou Corne Sinkhole shown in Figure 2 admonishing us that a risk of loss integrity of the side wall of BC-20 should be investigated. Due to the Bayou Corne cavern collapse, 150 homes had been evacuated for

nine months since August 3, 2012 [LSU, 2013]. This report evaluates the possibility of failure of the sidewall (indicated by yellow ovals in Figures 1) through a geomechanical analysis using a newly developed numerical model [Park and Roberts, 2015; Park et al., 2017].

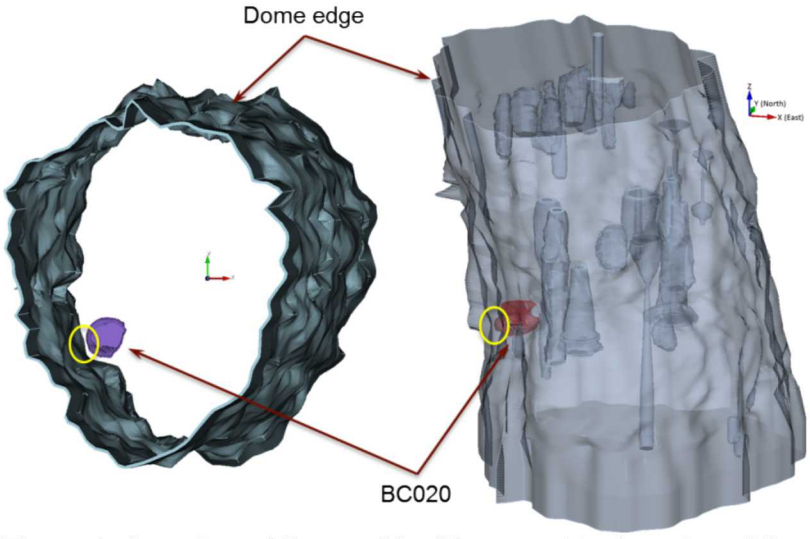

Figure 1. Location of Cavern 20 with respect to the edge of the salt dome

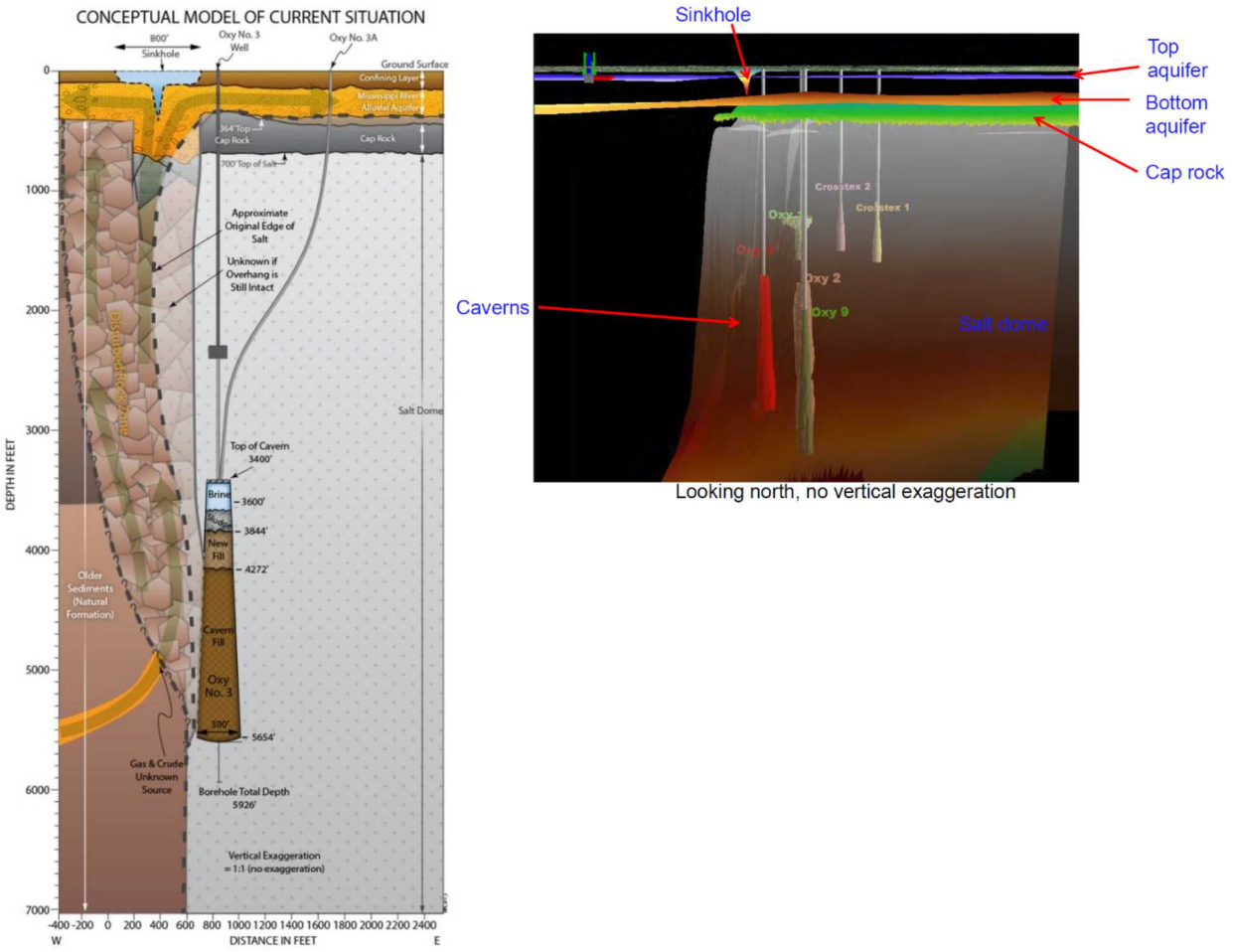

Figure 2. Conceptual diagram of failure/collapse of the sidewall of the brine-mined Oxy Geismar 3 salt cavern in the Napoleonville Salt Dome (left) and other caverns in vicinity of Oxy 3 (right). Formation of the Bayou Corne sinkhole occurred on August 3, 2012 [LSU, 2013]

1.1.3. BC-4

The U.S. Strategic Petroleum Reserve has expressed an interest in upgraded monitoring of BC abandoned Cavern 4 (BC-4) in light of the issues raised with the 2012 failure of the Oxy 3 salt cavern and related sinkhole formation near Grand Bayou, LA. Moreover, the State of Louisiana requires that operators-of-record for any salt cavern closer than 300 ft. from the edge of the salt stock provide plans for ongoing monitoring to confirm structural stability [LADNR 2013]. BC-4 is currently filled with brine and will not hold pressure at the wellhead. The cavern extends upward into the caprock and has no salt roof. A series of geotechnical reports [Hogan 1980; Todd and Smith 1988; Neal et al. 1993; Ehgartner 2007; Lord et al. 2015] have discussed the potential for roof collapse and possible outcomes. This report evaluates the structural stability in BC-4 through a geomechanical analyses using a newly developed numerical model [Park et al. 2017a; Park et al. 2018].

1.2. Objective

Sandia uses large-scale, three-dimensional (3D) computational models to simulate the geomechanical behavior of underground storage facilities consisting of solution-mined caverns in a salt dome. Recent advances in the state-of-art in geomechanics modeling have enabled 3D analyses to be performed. Three-dimensional analyses capture the actual geometry and layout of a cavern field and result in more realistic simulations. The complexities within the BC cavern field require such advanced simulations as the field has a long history of development resulting in 26 caverns of various shapes, depths, and states. This report attempts to model these conditions and addresses the resulting performance and stability issues.

This report describes a series of geomechanical simulations of BC SPR. As the first of the series, Park and Roberts [2015] developed a three-dimensional finite element mesh capturing realistic geometries of BC site has been constructed using the sonar and seismic survey data obtained from the field. The mesh consists of hexahedral elements because the salt constitutive model is coded using hexahedral elements. Park [2017a] described a model calibration to match the analysis results to the field observations as the second of the series. Park [2017b] updated the number of available drawdowns and the integrity of wellbores for the BC SPR caverns. This report provides explanations for the geotechnical concerns for the pillar between Caverns 15 and 17, the stability of Cavern 20 and the abandoned Cavern 4 as the third of the series and conclusions.

2. SITE DESCRIPTIONS

The BC salt dome, located in south-central Louisiana near Baton Rouge (Figure 3), was discovered in 1926. Since then over three hundred oil and gas wells have been drilled on and around the dome, as well as numerous shallow holes drilled into the caprock. Since 1937, Allied Chemical Corporation has drilled over twenty brine wells on the dome. In 1976, U.S. Department of Energy (DOE) purchased eleven of these leached caverns and was storing approximately twenty two million barrels of crude oil in three of the caverns (numbered 15, 18, and 19), forming part of the SPR Program [Hogan, 1980].

Since 1980, SPR caverns 18, 19, and 20 have been enlarged substantially; Union Texas Petroleum (UTP) Caverns 6 and 26 have been constructed, and Caverns 101 and 102 have been leached by DOE. Cavern 102 was traded to UTP in a swap for Cavern 17, now used for SPR oil storage. In 1992 UTP converted its brine Cavern 24 to natural gas storage. UTP had leached in 1993 along the northeast dome edge [Neal et al., 1993]. The UTP caverns have gone through several changes in ownership - first UTP, then Petrologistics, and now Boardwalk Pipeline Partners (hereafter call "Boardwalk") . The DOE re-purchased Cavern 102 from Boardwalk to use for SPR in 2012.

Data from the 300 oil and gas wells were used to construct contour maps and cross sections of the salt dome and the overlying caprock. Figure 4 shows a plan view of the BC site with salt contour lines defining the approximate location of the salt dome edge. The locations of the six SPR caverns, nine Boardwalk caverns, one inactive cavern, and seven abandoned caverns are included. A vertical cross section through Cavern 4 and Cavern 18 provides a geologic representation near the middle of the dome as shown Figure 4.

The surface and near-surface sediments overlying the BC dome are of Pleistocene through Holocene age. The oldest sediments consist of proglacial sands and gravels with some clay layers. These sediments are overlain by alternating sequences of sand, silts, and clays [Hogan, 1980].

Two distinct zones are found in the caprock at BC: an upper zone, termed the clay and gypsum zone (CGZ); and a lower zone, called the massive gypsum-anhydrite zone (GAZ). The CGZ is composed of layers of gypsum intercalated with clay. The proportion of clay to gypsum is highly variable, with generally more clay than gypsum. The GAZ is predominantly gypsum-anhydrite with minor amounts of clay, sand, and gypsum [Hogan, 1980].

The top of the BC salt dome lies between 600 and 700 ft below the surface. The east flank dips gently downward to 1,500 feet where the dip increases to approximately 80º between 2,000 and 6,000 ft. The west flank of the dome is overhung between 1,000 and 5,000 ft. Below 6,000 to 8,000 ft, the slope of the salt surface diminishes to about 60º [Hogan, 1980].

The lithology surrounding the salt dome contains up to 30,000 ft of silts, sands, shales, limestones, and evaporites. These sediments were deposited in a variety of sedimentary environments including desert basin, evaporating flat, ocean basin, and delta [Hogan, 1980].

The stratigraphy near the BC salt dome is shown in Figure 5. The top layer of overburden, which consists of sand, silts, and clays, has a thickness of 500 ft. The caprock, consisting of gypsum, anhydrite, and sand, is 160 ft thick. The bottom of the deepest cavern (Cavern 27) is at a depth of 6,280 ft. For the vertical direction constraint at the bottom of the model, sufficient thickness

between the lowest cavern bottom and the model bottom is necessary to not affect the structural reaction by the bottom boundary. Therefore, the depth of the salt dome is considered to be 6,400 ft below the surface. All SPR caverns are located below 2,000 ft below ground surface.

The faults shown in Figures 4 and 5 will be ignored in the present finite element (FE) model because the faults do not extend into the salt thus are not expected to affect the structural behavior of the SPR caverns. And, by ignoring the shear zones, the models of overburden and the cap rock layers are able to be simplified.

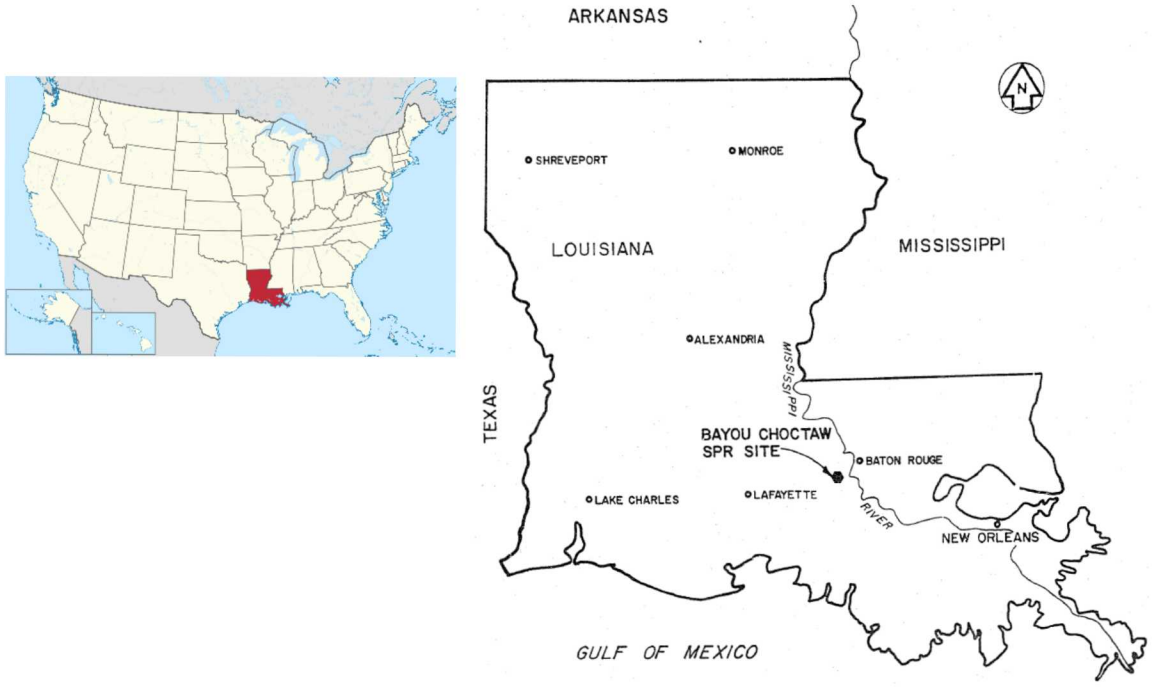

Figure 3. Bayou Choctaw SPR site location map

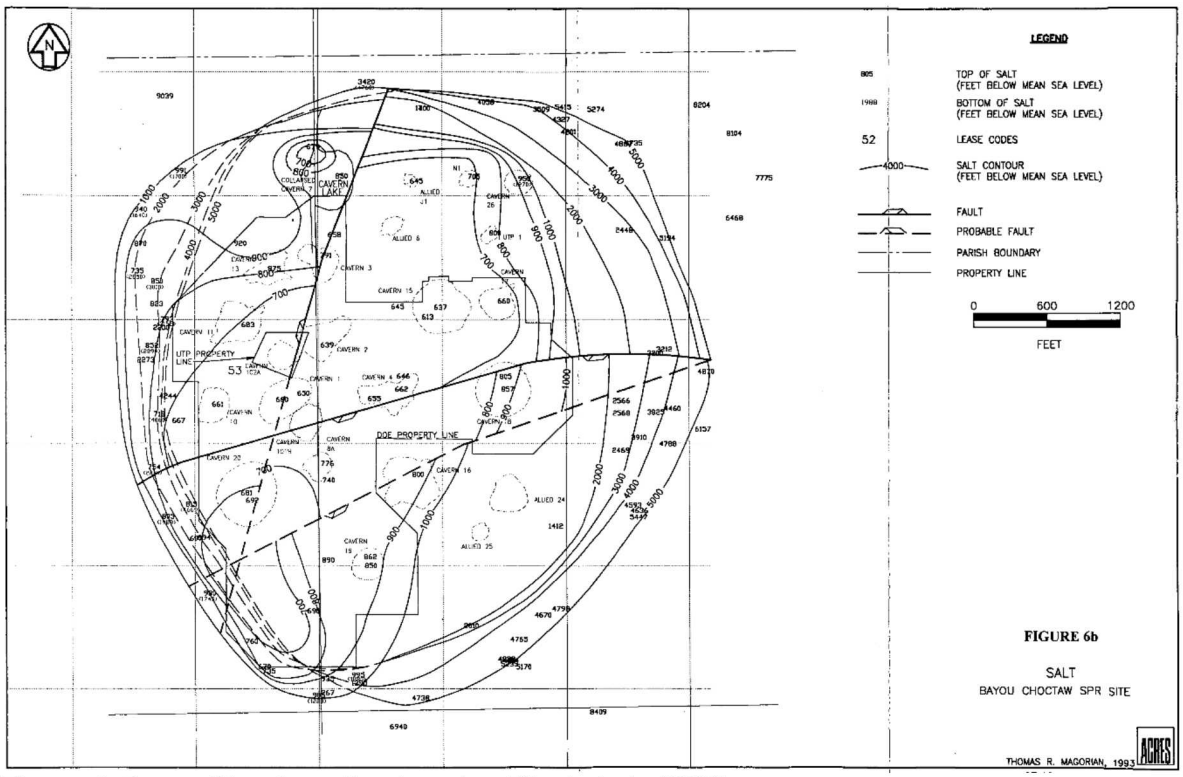

Figure 4. Bayou Choctaw site plan view [Neal et al., 1993]

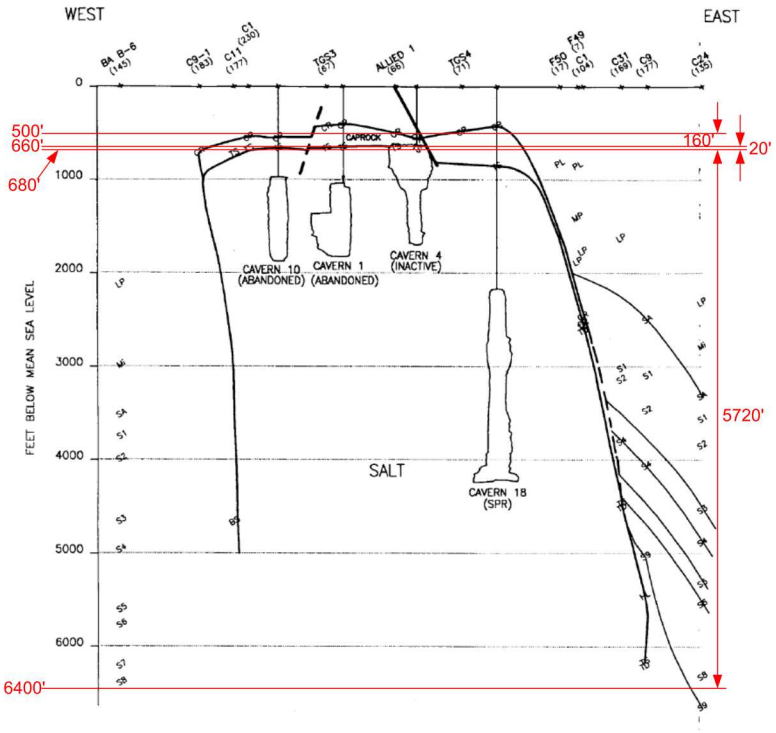

Figure 5. Stratigraphy near the Bayou Choctaw salt dome [Neal et al., 1993] and the thickness of each layer used for modeling.

Intentionally left blank

3. GOEMETRICAL CONDITIONS

3.1. Basic Rule

Finite element codes such as SIERRA/ADAGIO[1] are designed to conduct simulations with finite elements that are either tetrahedral or hexahedral. Two constitutive material models, i.e. the Power Law Creep (PLC) model and the Multi-Mechanism Deformation (M-D) model, are available in ADAGIO to represent salt behavior. These two material models are programmed in SIERRA/ADAGIO assuming eight-node hexahedral elements. Therefore, the mesh for the BC SPR site must be constructed with hexahedral elements. Hexahedral elements include six convex quadrilateral sides, or facets, with the eight corners where these facets intersect being the eight nodes for an element. The cavern boundaries such as the ceiling, wall, and floor are obtained from sonar measurements, and the irregular geometries of these boundaries ultimately require various shapes of facets. Similarly, the geometry of the flank of the salt dome, obtained from seismic measurements, also consists of complicated shapes of facets. To construct a mesh with convex hexahedral elements for a geological volume keeping the complicated geometry as much as possible, the following rules were established and followed:

1. Each perimeter (cavern and dome) consists of the same number of vertices at each depth interval
2. The reference distance between vertices on a perimeter is:
    a. about 20 ft for caverns
    b. about 80 ft for dome
3. The vertical thickness of an element level is kept constant at 20 ft
4. A cavern volume increase of 15% is used for each drawdown leach

Modeling of the leaching process of the caverns is performed by deleting a pre-meshed block of elements along the walls of the cavern so that the cavern volume is increased by 15 percent per drawdown. The 15% volume increase is typical for a standard freshwater drawdown, although salt quality can vary that amount. Also, typical leaching processes tend to increase cavern radius more at the bottom of the cavern than at the top, with very little change to the roof and floor of the cavern. For the purposes of this modeling effort for Bayou Choctaw, leaching is assumed to add 15% to the volume of the cavern, and is assumed to occur uniformly along the entire height of the cavern, with no leaching in the floor or roof of the caverns. Each leaching layer, or “onion skin,” is built around the perimeter of the meshed cavern volume using the rules stated previously. The detailed steps and methodologies to construct the FE mesh were provided by Park and Roberts [2015]; and Park et al. [2017].

1 ADAGIO is the most recently Sandia-developed 3D solid mechanics code. It is written for parallel computing environments, and its solvers allow for scalable solutions of very large problems. ADAGIO uses the SIERRA Framework, which allows for coupling with other SIERRA mechanics codes.

3.2. Salt Dome

The top of the dome lies between 600 and 700 ft below the surface. The salt surface on the top of the dome is relatively flat, sloping gently outward to a depth of approximately 1000 ft where the angle suddenly steepens sharply. The cross-sectional area within the 1000 ft contour is about 284 acres. The east flank dips gently downward to 1500 ft where the dip increases to approximately 80° between 2000 and 6000 ft. The west flank of the dome is overhung between 1000 and 5000 ft. Below 6000 to 8000 feet on both flanks, the slope of the salt surface begins to flatten toward 60°. The change in the dip of the salt mass is demonstrated by the sectional area of the dome at 5000 feet which is 371 acres. By 9000 ft, however, the area has increased to 742 acres. Calculations show an average dome growth rate between 2.8×10^{-4} to 3.5×10^{-4} in/year since the end of the Pliocene. The steepest dip is found on the west flank where there is the pronounced caprock and salt overhang. Other small overhangs are indicated on the east and north flanks [Hogan, 1980].

The three-dimensional seismic survey over the Bayou Choctaw salt dome used in this study was shot originally in 1994, and the objective of the original processing appears to have been deep petroleum targets along the flanks of the salt dome [Rautman et al., 2009]. Sandia has completed the interpretation and first-pass modeling of the Bayou Choctaw salt dome using 3-D seismic information. The seismic volume was licensed from Seitel Data, Ltd., and it comprises approximately 16 square miles of data centered directly above the Bayou Choctaw salt dome. After examining the as-received processed data, Sandia determined to reprocess the un-composited field data to improve resolution of the shallower portion of the stratigraphic section, including the upper portion of the salt stock. Geologic interpretation of the resulting custom-processed information has been on-going for some time. However, Sandia have completed a first-pass modeling effort of the interpreted data [Rautman et al., 2008].

Roberts [2015] generated the salt dome image using the seismic data and 4DIM[2] tool. Park and Roberts [2015] constructed the three-dimensional hexahedral FE mesh using the seismic data and the CUBIT mesh generation tool as shown Figure 6. The 3D-coordinates of vertices are resampled from the seismic image. The real salt dome top is not flat as shown in the seismic image in Figure 6. The uneven top surface will create poorly shaped elements. To avoid poor shapes, the vertex data above the elevation of -1320 ft are removed (a process called ‘trimming’). The salt dome leans to the west. The coordinates of vertices at every 20 ft element level from level -1300 ft through -680 ft are calculated considering the leaning. In a similar manner, the vertex data below the elevation of -5880 ft are trimmed off. The vertex data for the lower salt blocks are translated vertically downward from the vertex data of the bottom of trimmed salt dome block (-5880 ft). The leaning slope of dome is not considered for the lower salt block. The dome mesh consists of 286 element levels each 20 ft thick. The bottom elevation is -6400 ft.

2 Four-Dimensional Interactive Model Player developed by C Tech.

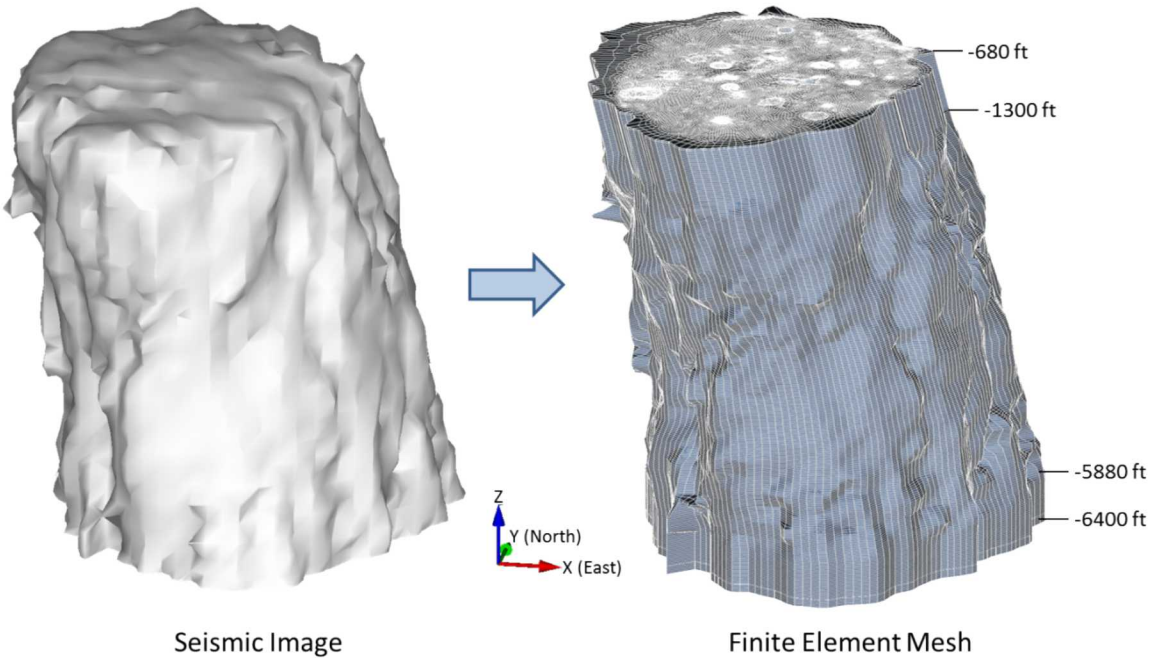

Figure 6. Images of Bayou Choctaw salt dome obtained from the seismic survey (left) and hexahedral finite element mesh using the seismic survey data

3.3. Lithologies Surrounding the Salt Dome

3.3.1. Overburden

The surface and near surface sediments overlying the Bayou Choctaw dome are of Pleistocene through Holocene age. The oldest sediments consist of proglacial sands and gravels with some clay layers. These sediments are overlain by an alternating sequence of sands, silts, and clays [Hogan, 1980]. The bottom of overburden layer (top of the dome) is not flat as shown in Figure 5. The bottom is simplified as a flat to avoid creating poor-shaped elements. Figure 7 shows the meshed overburden block that is 12,000 ft long, 11,000 ft wide, and 500 ft thick. The thickness of each element layer is 20 ft in this model, so the mesh has 25 element levels vertically. Each element is hexahedral.

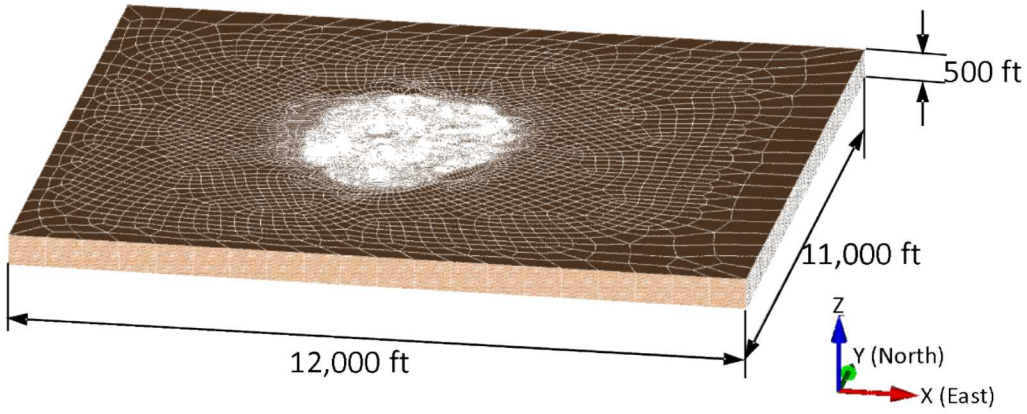

Figure 7. Overburden meshed block

3.3.2. Caprock

Two distinct zones are found in the caprock at Bayou Choctaw: an upper zone, termed the clay and gypsum zone; and the lower zone, called the massive gypsum-anhydrite zone. The clay and gypsum zone is composed of layers of gypsum intercalated with clay. This zone is up to 150 ft thick and lies within 400 to 433 ft of the surface. The massive gypsum-anhydrite zone is the lower unit and consists of gypsum-anhydrite with some clay and sand. A discontinuous massive layer of gypsum-anhydrite, 20 to 60 ft thick, marks the top of this zone which lies within 500 to 600 ft of the surface. Faults and fractures in the caprock, formed by salt dissolving and collapse at the salt/caprock contact, result in a highly permeable and discontinuous unit with little structural strength [Hogan, 1980].

Figure 8 shows the BC caprock image generated using the seismic data and 4DIM tool, and hexahedral FE mesh. Since this image was developed from contours which were hand-drawn, some of the surfaces appear a flat. The bottom of the caprock surface is based on the topography of the salt dome top. The actual caprock top and bottom are not flat. The uneven top and bottom will produce poorly shaped elements. To avoid a poor shape, the vertex data for the caprock are translated vertically upward from the vertex data of the flat surface of salt dome top as shown in Figure 6. The thickness of each element layer is 20 ft in this model, so the mesh has 8 element levels vertically because the caprock is simplified as a flat slice block 160 ft thick as shown in Figure 5.

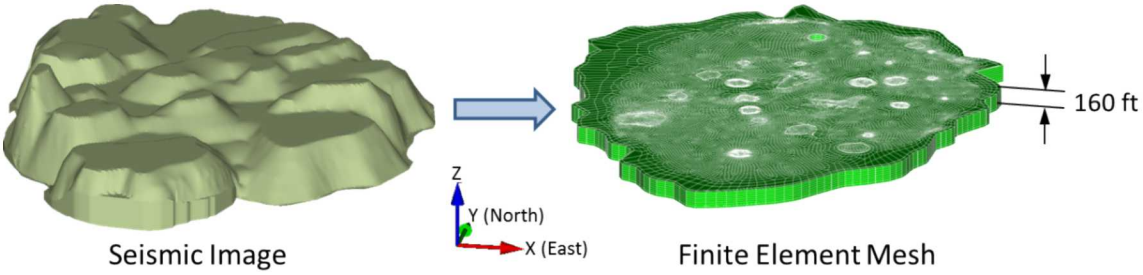

Figure 8. Image of Bayou Choctaw caprock obtained from the seismic survey (left) and hexahedral finite element mesh

3.3.3. Interbed

Oil leaks were found in wellbores of Caverns 105 and 109 at the Big Hill (BH) SPR site. According to the field observations, two instances of casing damage occurred at the depth of the interbed between the caprock bottom and salt top. A three dimensional finite element model was constructed to investigate horizontal and vertical displacements in each well as it crosses the various interbeds. The analysis results indicate that the casings of Caverns 105 and 109 failed from shear stress that exceeded the casing shear strength due to the horizontal movement of the salt top relative to the caprock, and tensile stress due to the downward movement of the salt top from the caprock. The salt top subsides because the volumes of caverns in the salt dome decrease with time due to salt creep closure, while the caprock does not subside at the same rate as the salt top because the caprock is thick and stiff. This discrepancy causes deformation of well. ADAGIO has a contact surface algorithm for modeling contact and sliding behavior between two solid surfaces. However, this algorithm has a limitation on the number of elements in the model.

The number of elements in the BH model was over the limitation. In place of a contact surface, a thin soft layer of elements is used for the interface between lithologies. The thin soft element layer is assumed to behave mechanically like a contact surface from a perspective of relative displacement between two lithologies [Park, 2014].

A similar interbed layer is implemented in the BC model to represent the salt/caprock contact. The collapse zone at the BC salt/caprock contact, is a highly permeable and discontinuous unit with little structural strength [Hogan, 1980]. The contact zone is modeled by the thin soft element layer interbed block to evaluate the caverns' geomechanical effect on wellbore integrity. Figure 9 shows the BC interbed FE mesh. The real interbed between the salt dome and caprock is not flat. The uneven interbed could cause poorly shaped element to be generated. To avoid the poor shape, the vertex data for the interbed are translated vertically upward from the vertex data of the simplified flat surface of salt dome top. The thickness of interbed layer is assumed to be 20 ft, so it has one element level.

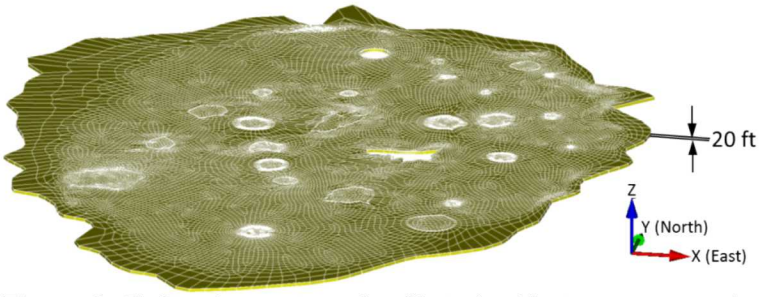

Figure 9. Finite element mesh of interbed between caprock and salt top

3.3.4. Interface between dome and far-field

The Bayou Choctaw salt dome is a piercement structure which has penetrated Mesozoic through Quaternary sediments. As in other types of intrusions, the salt dome must displace the overlying sediments as it pushes upward. Any sediment deposited above the dome will be either pushed aside and/or lifted up, increasing the chance of erosion occurring on the loosened material. The mechanical failure of the sediments surrounding the dome has caused faults to develop both radially from and tangentially to the dome in a series of graben-horst structures [Hogan, 1980].

To consider the faults surrounding the dome, the interface block is inserted between the dome and sediments surrounding the dome which consists of the caprock, interbed, and salt dome blocks. As with the interbed block in Section 3.3.3, a thin, soft layer of elements is used for the interface between lithologies, i.e. this model contains an interface block between the dome and surrounding sediments (hereafter 'surrounding rock' or 'far-field rock') as shown Figure 10.

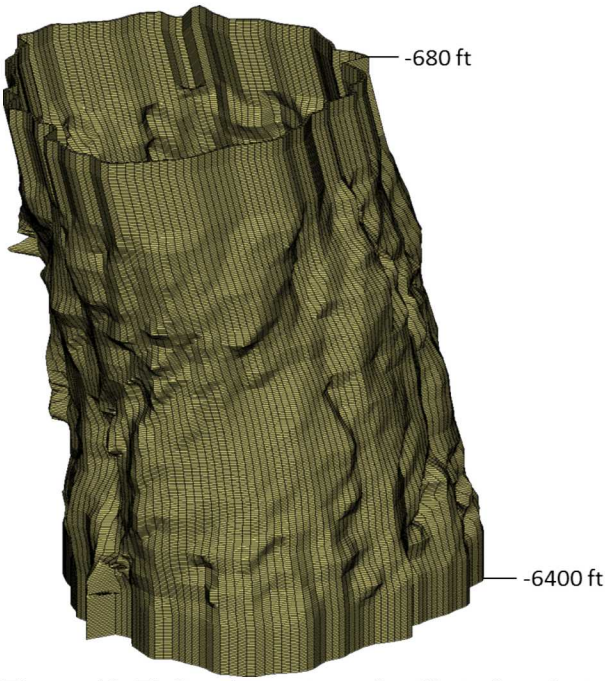

Figure 10. Finite element mesh of interface between dome and far-field

3.3.5. Far-field

The Bayou Choctaw salt dome lies within the Gulf Coast geosyncline, an area of sediment deposition from the Mesozoic era to the present. In the site area, the geosyncline contains up to 30,000 ft of silts, sands, shales, limestones, and evaporites. These sediments were deposited in a variety of sedimentary environments including desert basin, evaporating flat, ocean basin, and delta. Salt domes within the geosyncline occur in two regions: a northern belt through northern Louisiana and Mississippi, and a southern belt along the Gulf Coast and offshore. The Bayou Choctaw dome is on the northern edge of the southern coastal belt of salt domes. The largest tectonic feature near the site is the Baton Rouge fault system which lies approximately five miles to the north. The fault trends from Breton Sound, Louisiana, to Matagorda Bay, Texas, a distance of more than 500 miles. In Louisiana the Baton Rouge fault marks the northern limit of the southern Gulf Coast salt domes [Hogan, 1980].

For simplification, the rock surrounding the salt dome is assumed to be made of an isotropic, homogeneous, linear elastic material in this model. The surrounding rock block encircles the interface, caprock, interbed, and salt dome blocks. The lengths of the confining boundaries are 11,000 ft in the N-S direction and 12,000 ft in the E-W direction as shown Figure 11. The diameters of the caverns are much smaller than the dome diameter. The model boundary distances (surrounding rock dimensions) can be regarded as being an infinite distance away from the caverns (i.e. fixed boundaries can be applied).

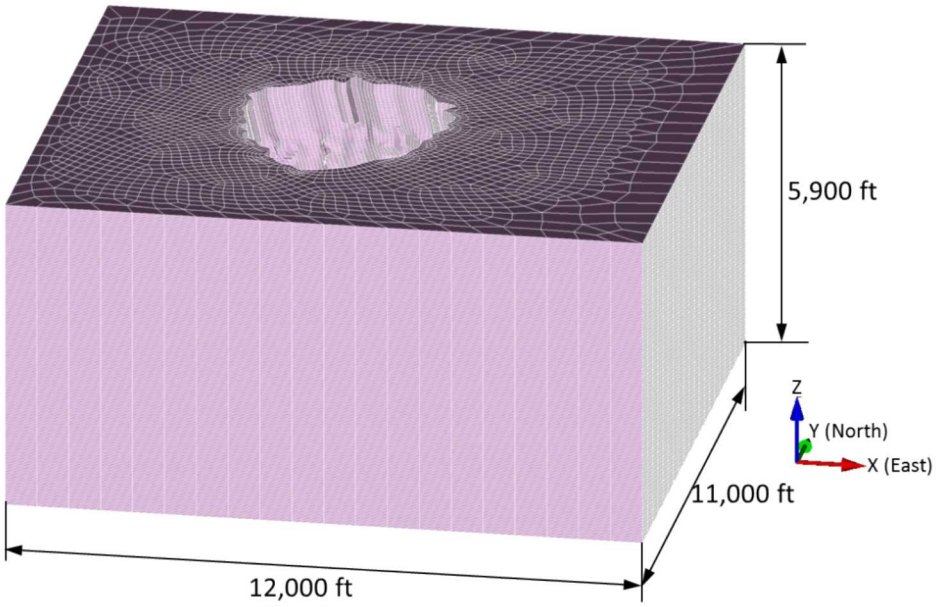

Figure 11. Finite element mesh of surrounding rock (far-field)

3.4. Caverns

3.4.1. Sonar Data Manipulation

Representations of the BC caverns based on sonar data were incorporated into the geomechanical model to provide a more realistic depiction of the caverns. To facilitate this, the cavern sonar data were resampled to a nodal spacing more appropriate for the geomechanical model. The actual sonar data was provided from the sonar contactors. An additional processing code SONAR7[3] was used to turn these contractor files into a format compatible with the MVS[4] geologic modeling software suite. This is a mature process which has been used for many years at Sandia. This step is necessary to provide a full three-dimensional surface model of the sonar data. The assigned vertices in the FE mesh created in CUBIT need to be at specific depth intervals which may not correspond to the actual sonar sampling locations. Continuous three-dimensional surface models of the survey data are created, which allows sampling at any depth needed. This resampling step is performed through an algorithm coded using Python. Then, the resampled node coordinates data sets for the caverns are generated as the output in this step. The resampled nodal data are converted into CUBIT vertex data through Microsoft Excel manipulation. The mesh is constructed using cavern slice blocks of 20-ft thick layers generated using the coordinates of vertices.

Table 1 lists the level of cavern top and bottom, cavern volumes, and the dates when the sonar data were obtained. The cavern volumes calculated from SONAR7 and CUBIT are different. The SONAR7 volumes are calculated from the full three-dimensional surface model of the sonar data,

3 A data conversion program developed by Sandia. SONAR7 converts sonar data sets with various formats provided by different vendors into the extended file format (EFF) and other MVS compatible formats.

4 MVS (Mining Visualization System) is C Tech's flagship product for state-of-the art analysis and visualization. MVS was designed from the ground up to meet the demanding requirements of underground and surface mining analysis. Its tools are also used by civil engineers and advanced environmental modelers.

while the CUBIT volumes are calculated from the FE discretized mesh. Typically, the CUBIT-generated volumes are slightly less than those from SONAR7 because the curved surfaces are converted into flat facets with four nodes. The volume differences are usually less than 5% except for BC-3, 10, 11, 13, 18, and N1. BC-3, 10, 11, and 13 are abandoned, so and their volume discrepancies are not expected to significantly affect the global salt behavior because they were all plugged with their wellheads cut off below ground surface and buried. The BC-N1 has a very irregular shape. It is far from the SPR caverns, so it is also not expected to influence the behaviors of the SPR cavern. The bottom part of BC-18 is much larger than the upper, and the resulting distortion of the geometry to create the FE mesh for this cavern accounts for the volume discrepancy. The 3D hexahedral element meshes for 26 caverns constructed using various functions in CUBIT are shown in Figure 12.

Table 1. Levels of cavern tops and bottoms, cavern volumes, and sonar survey dates. Blue, green, and gray fonts indicate the SPR, Boardwalk, and abandoned caverns, respectively.

Cavern ID	Sonar Survey Date for Mesh Data	Top Elevation (ft)	Bottom Elevation (ft)	Volume (bbl)		Difference (B-A)/A
				Sonar7 (A)	Cubit (B)	
BC-1	5/30/1980	-1040	-1780	8,321,703	7,979,595	-4.1%
BC-2	7/28/1983	-780	-1520	9,168,111	9,413,900	2.7%
BC-3	7/13/1977	-1020	-1840	5,016,299	4,176,331	-16.7%
BC-4	7/30/2013	-640	-1680	6,254,862	6,125,965	-2.1%
BC-6	11/1/2006	-1240	-1560	865,285	845,144	-2.3%
BC-7	Collapsed in 1954	0	-1960	2,900,000	2,872,777	-0.9%
BC-8	5/31/1980	-1300	-1960	3,022,481	2,927,863	-3.1%
BC-10	9/13/1973	-1000	-1980	6,357,213	5,574,316	-12.3%
BC-11	3/10/1978	-1080	-1740	8,907,671	7,400,907	-16.9%
BC-13	8/13/1977	-1120	-1860	4,042,210	3,325,433	-17.7%
BC-15	4/15/2009	-2600	-3260	16,493,972	16,141,623	-2.1%
BC-16	6/28/2004	-2620	-3220	11,427,940	11,231,618	-1.7%
BC-17	4/16/2009	-2600	-3960	11,395,042	11,120,677	-2.4%
BC-18	1/6/2009	-2140	-4160	18,323,973	16,776,640	-8.4%
BC-19	4/14/2009	-2980	-4200	11,994,283	11,823,169	-1.4%
BC-20	12/13/2013	-3820	-4180	9,418,726	9,392,715	-0.3%
BC-24	4/17/1992	-3100	-4320	5,954,764	5,914,635	-0.7%
BC-25	10/30/2007	-2580	-5660	17,153,669	16,601,697	-3.2%
BC-26	10/11/1996	-2300	-3320	2,395,796	2,395,466	0.0%
BC-27	10/28/2007	-5940	-6280	1,370,853	1,313,614	-4.2%
BC-28	10/29/2007	-4700	-6240	2,222,859	2,218,799	-0.2%
BC-J1	7/27/2006	-2860	-3900	1,243,321	1,186,069	-4.6%
BC-N1	12/5/2003	-1920	-3480	1,880,690	1,753,729	-6.8%
BC-UTP	10/14/2006	-2380	-3480	1,567,808	1,500,687	-4.3%
BC-101	2/1/2005	-2580	-4780	12,454,068	12,188,119	-2.1%
BC-102	2/22/2012	-2640	-5220	9,678,299	9,602,558	-0.8%

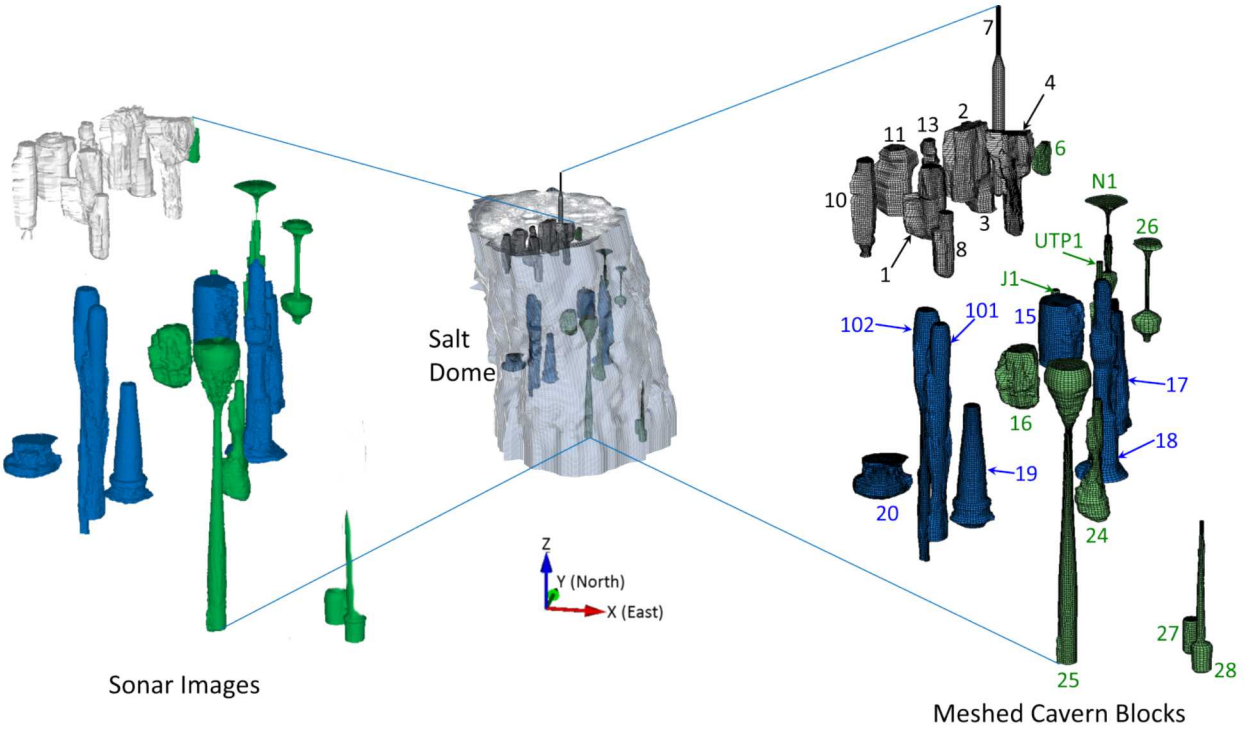

Figure 12. Sonar Images and hexahedral finite element meshed block of 26 caverns in the Bayou Choctaw salt dome. Caverns in gray, green, and blue indicate the abandoned, Boardwalk, and DOE SPR caverns, respectively. The cavern ID numbers are also shown.

3.4.2. Non-SPR Caverns

From a perspective of mesh generation, the caverns in the BC salt dome are classified into two groups, non-SPR and SPR caverns. The non-SPR caverns are classified further into two groups, normal and abnormal caverns.

The following caverns are classified as non-SPR caverns:

- Normal group: BC-1, BC-2, BC-3, BC-6, BC-8, BC-10, BC-11, BC-13, BC-16, BC-24, BC-25, BC-26, BC-27, BC-28, BC-J1, BC-N1, and BC-UTP
- Abnormal group: BC-4, BC-7

The normal caverns are those whose entire cavern volumes exist within the salt dome. The abnormal cavern BC-4 was leached into the salt dome and the top of the cavern extended into the caprock layer. BC-7 collapsed in 1954 and was filled with overburden material which formed a lake on the surface above the cavern. Therefore, the cavern boundary extends into three lithologic layers such as the salt dome, caprock and overburden layers.

Figure 13 shows the BC-1 cavern cavity with an extra skin layer as an example of normal non-SPR caverns. The non-SPR caverns, because they are abandoned and private caverns, do not require the explicit meshing of a drawdown leach. However, one onion skin (extra skin layer) is constructed to check the analysis results at the cavern wall, roof, and floor. The cavern skin can be separated from the entire mesh. The amount of numerical result data in the skin block is much less than in the whole mesh. Examining the result in the skin volumes makes storage and analysis efforts more efficient. The small amount of data can be handled easily to check various

structural behaviors of the cavern. In the same reason, every cavern has an extra skin as the outermost skin. The detailed steps and methodologies to construct the cavern meshes were provided by Park and Roberts [2015].

Figure 13. BC-1 cavern cavity with an extra skin

3.4.3. Abnormal Caverns

BC-4 is an abnormal shape cavern in the non-SPR caverns. The cavern is leached through three lithological layers, i.e. the caprock, interbed and salt layers. BC-4 stability has been the object of continuing concern because of its geologic similarity to collapsed BC-7 (now sinkhole lake on the surface). Sonar results in 1992 show minimal change since 1980, suggesting that significant caprock dissolution has not occurred and that overburden collapse is unlikely. However, continuing surveillance is prudent [Neal et al., 1993]. Figure 14 shows the BC-4 cavern cavity with caprock roof, that are based on the sonar data surveyed in 2003, along with a surrounding interbed skin and salt skin layer used in the geomechanical model for detailed stress analysis; these geometries are used to create the finite element mesh for the calculations.

BC-7 was drilled in 1942 to a total depth of 1951 ft and developed into a cavern for the production of brine. The depth to the original top of the cavern is not known. The cavern volume was calculated from production data to be 2.9 MMB. Normal brining operations continued into the early 1950's when cavern pressure was lost. It is assumed that pressure was lost when the cavern roof was leached to the top of the salt. Brining continued by the airlift method until January, 1954 when the cavern collapsed. This resulted in the formation of a crater on the ground surface about 800 ft in diameter which filled with water and is now called Cavern Lake. The cavern's collapse resulted from leaching of the salt to the salt/caprock contact followed by the failure of the caprock and overlying sediments [Hogan, 1980]. Cavern 7 collapse began at the wellhead, eventually filling the cavern with overburden [Hogan, 1980; Neal et al., 1993]. In this model, the elevation of the top of BC-7 is assumed to be the same as the elevation of the caprock top, -500 ft then, the height of the cavern is calculated to be 1451 ft. Based on production records, the diameter of BC-7 is calculated to be 120 ft. The coordinates of BC-7 well is estimated to be (-719, 1710) from Figure 4. The measured depth of the lake was -100 ft in 1956

[The Aerospace Corporation, 1980]. The lake depth (about 100 ft) is small relative to the model height (6400 ft) and the lake diameter (about 800 ft) is large relative to the lake depth, so the lake can be regarded as a part of the surface, and the lake geometry is simplified as flat in the surface of this model. The cavern is assumed to be cylinder shape with 120 ft diameter. The cavern roof in the caprock layer is assumed to be a conical frustum with 40 ft top diameter. A 40 ft diameter cylinder extends through the overburden layer from the ground surface to the top of the caprock. The cavern slice blocks in the caprock and interbed layers are separated from the cavern body in salt due to different material properties. The cavern height is 1460 ft rather than 1451 ft because the model meshes are discretized by 20 ft element level. The frustum shape with 120 ft and 40 ft diameters is used for the cavern roof and floor, so the amount of the cavern volume is close to 2.9 MMB. Figure 15 shows BC-7 cavern cavity with overburden, caprock, interbed and salt extra skins. The detailed steps and methodologies to construct the cavern meshes were provided by Park and Roberts [2015].

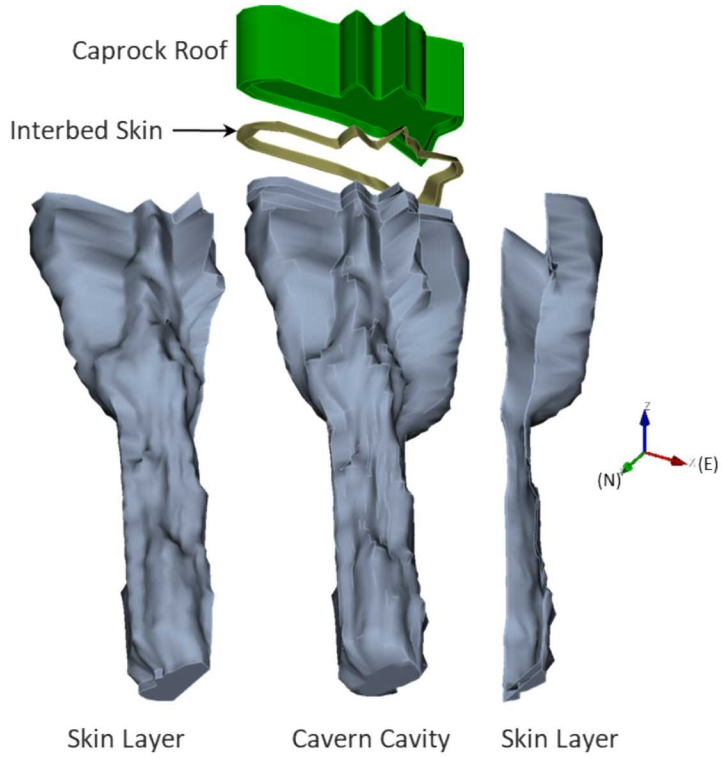

Figure 14. BC-4 cavern cavity with cavern roof, interbed skin, and salt skin layers

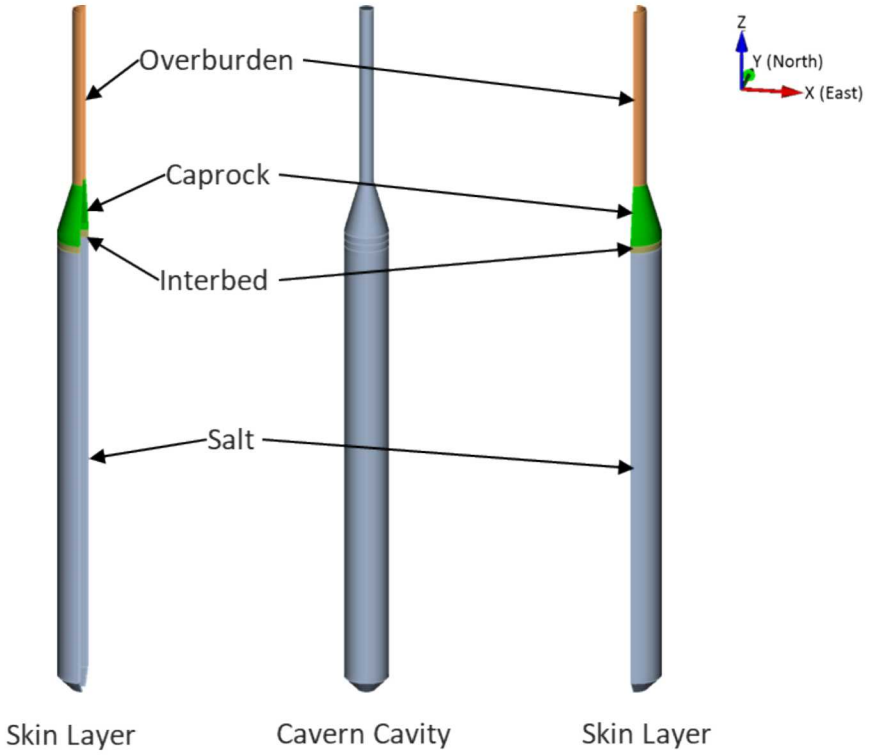

Figure 15. BC-7 cavern cavity with overburden, caprock, interbed and salt skin layers

3.4.4. SPR Caverns

As mentioned in Section 3.1, modeling of the leaching process of the caverns is performed by deleting a pre-meshed block of elements along the walls of the cavern so that the cavern volume is increased by 15 percent per drawdown. Figure 16 through Figure 22 show the volumes for each SPR cavern as developed from sonar data, along with drawdown skins (leaching layers) and extra skin. In this simulation, each SPR cavern is modeled as having five drawdown layers to be removed to account for the future oil drawdown activities. However, BC-15 and 17 are close to each other. More than four onion skins would induce poor mesh element shapes. Thus, three drawdown leaches are considered. BC-20 is close to the dome edge (less than 100 ft away). This close proximity creates two problems. The first is a physical problem, in that the closeness to the salt dome boundary poses potential cavern collapse issues (this issue is one of the driving factors for developing the current meshing technique). The second is a meshing problem; the addition of even one onion skin in the narrow pillar between the cavern wall and the dome edge will induce generation of poor mesh element shapes. Thus, BC-20 is considered a zero drawdown-leach cavern like the non-SPR caverns.

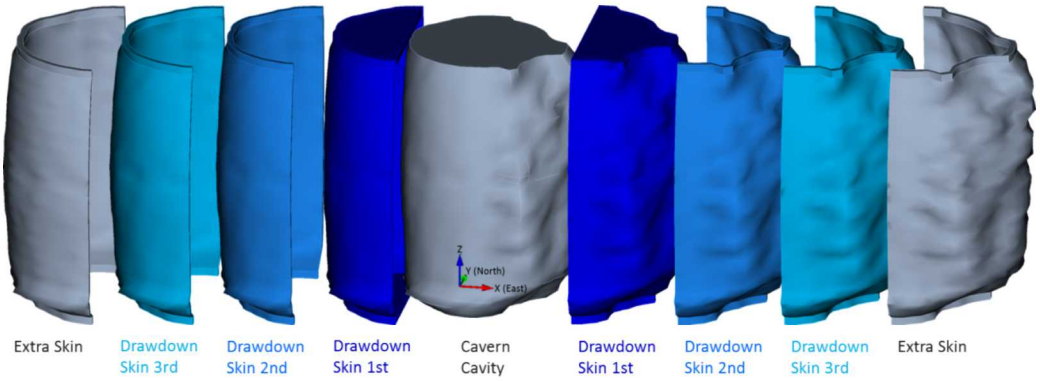

Figure 16. BC-15 cavern cavity with three drawdown skins (leaching layers) and extra skin

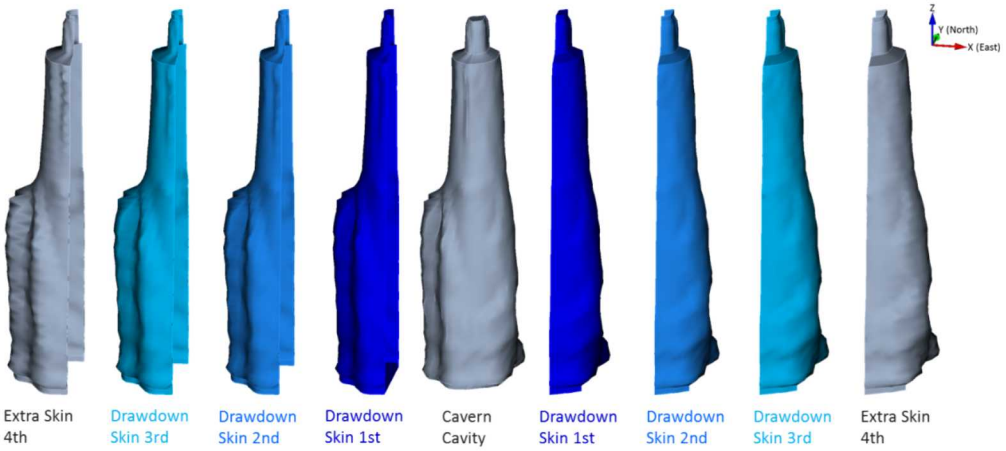

Figure 17. BC-17 cavern cavity with three drawdown skins (leaching layers) and extra skin

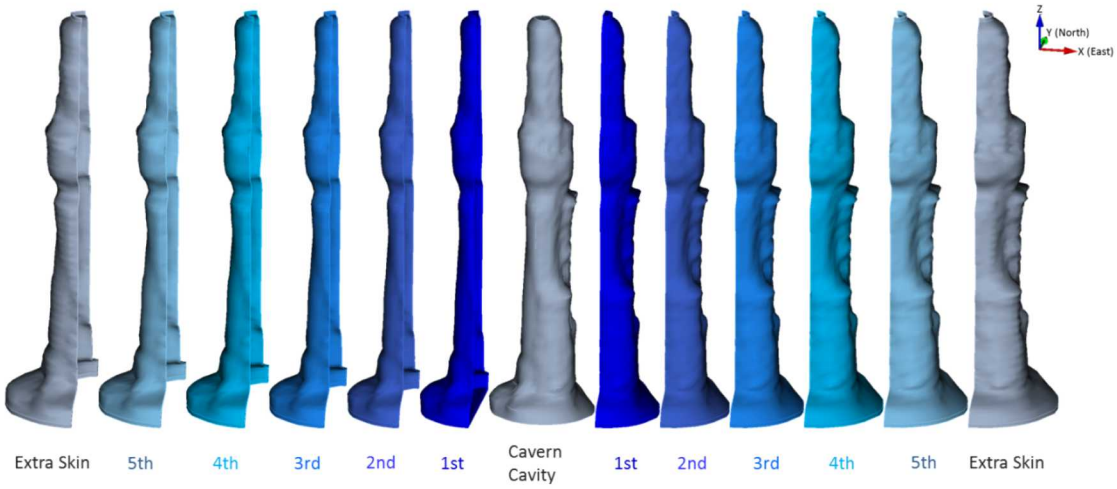

Figure 18. BC-18 cavern cavity with five drawdown skins (leaching layers) and extra skin

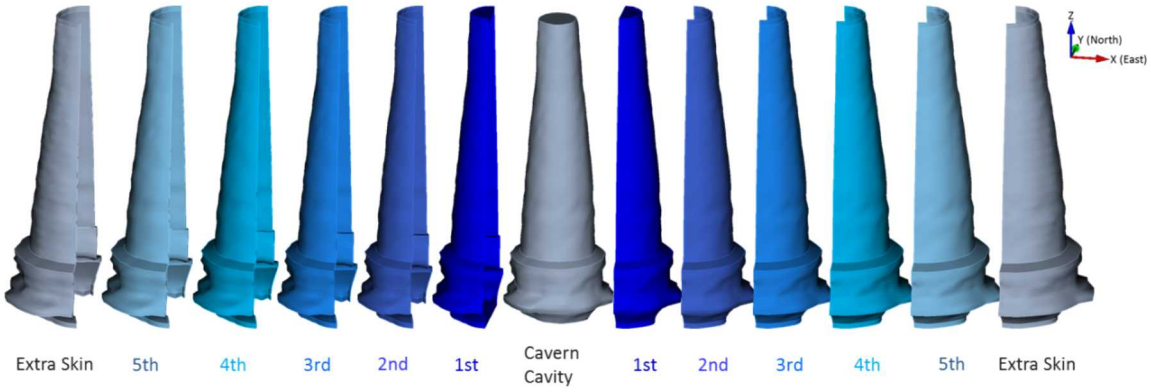

Figure 19. BC-19 cavern cavity with five drawdown skins (leaching layers) and extra skin

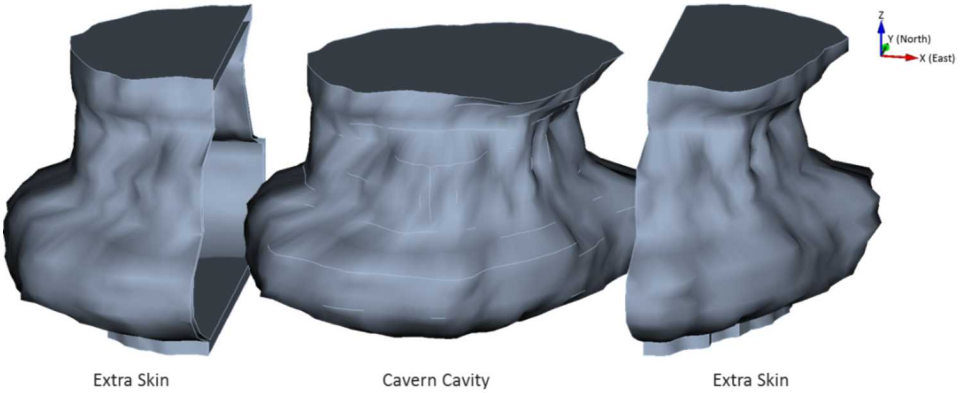

Figure 20. BC-20 cavern cavity with extra skin

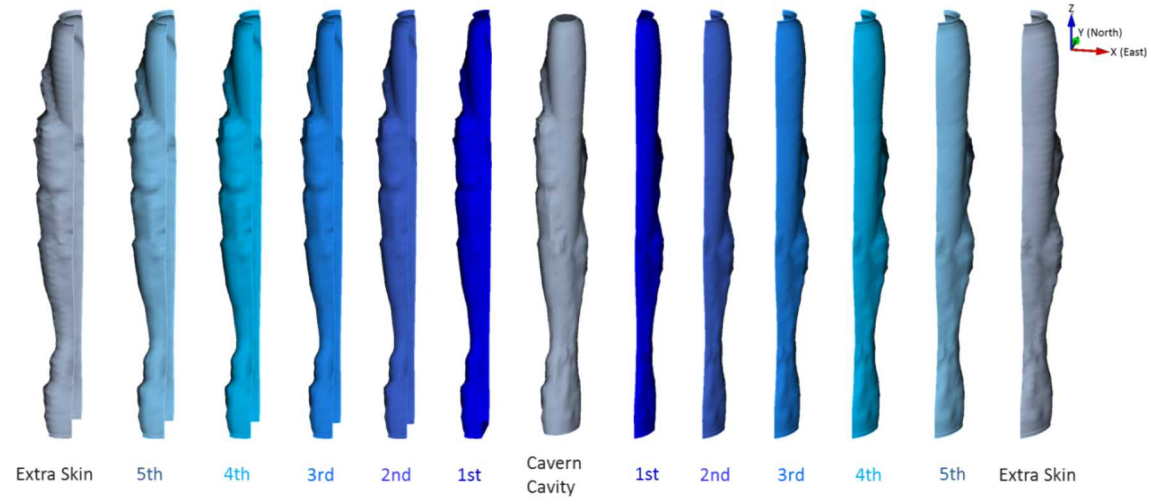

Figure 21. BC-101 cavern cavity with five drawdown skins (leaching layers) and extra skin

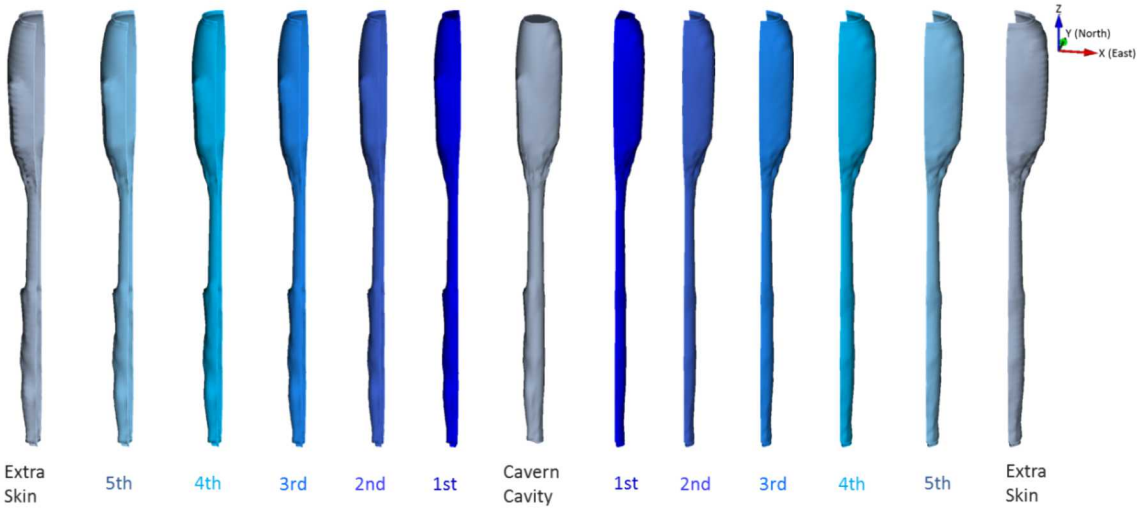

Figure 22. BC-102 cavern cavity with five drawdown skins (leaching layers) and extra skin

3.5. Entire Mesh

The BC-dome, caverns, caprock, interbed, interface, and surrounding rock blocks are combined into the entire BC-model as shown Figure 23, which also shows the overview of the hexahedral finite element mesh of the stratigraphy and cavern field at BC SPR site. The mesh consists of 7,796,127 nodes and 7,758,720 elements with 170 element blocks, 3 node sets (on the boundaries of the entire mesh, to enforce zero normal displacement boundary conditions), and 55 side sets (on the interior surfaces of the caverns and skin layers, to enforce cavern pressure boundary conditions).

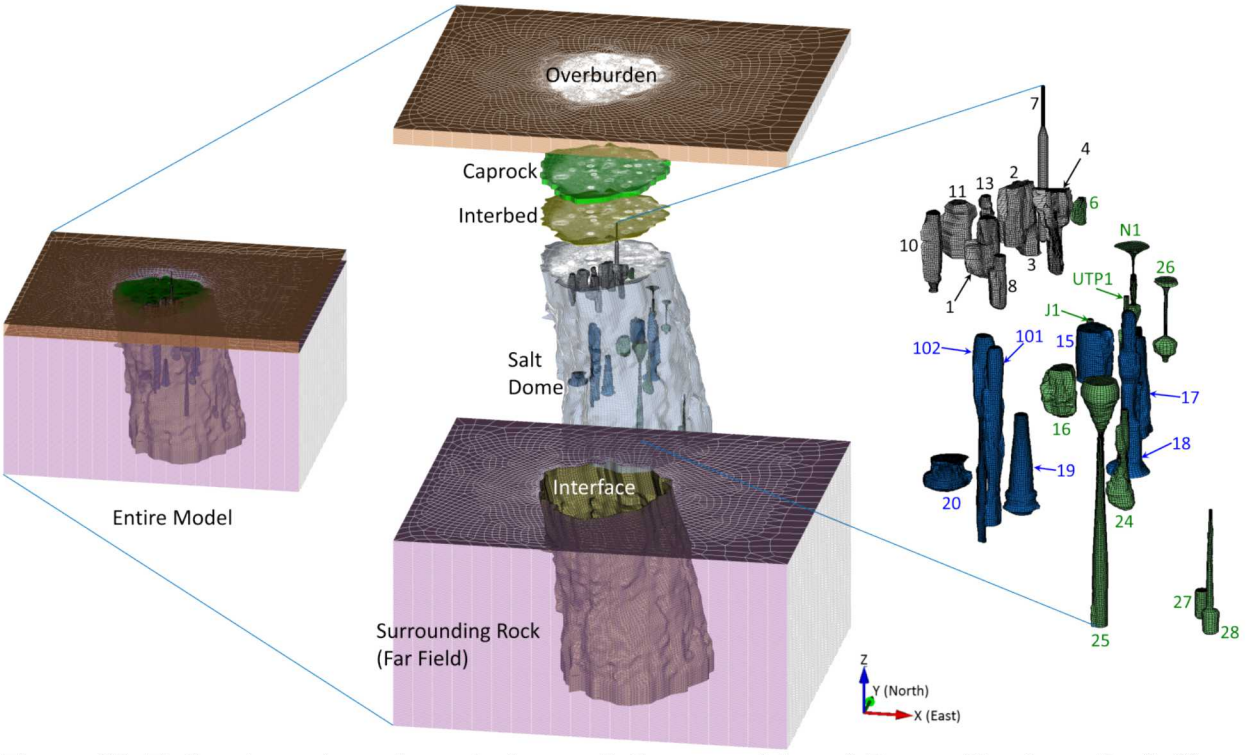

Figure 23. Finite element mesh capturing realistic geometries of Bayou Choctaw site (left), an overview of the meshes of the stratigraphy (middle), and caverns (right). The U.S. Strategic Petroleum Reserve stores crude oil in the seven blue caverns. The other caverns are the Boardwalk caverns (green) and abandoned caverns (gray). The cavern ID numbers are also shown.

4. MECHANICAL CONDITIONS

4.1. Wellhead Pressure

4.1.1. SPR Caverns

The modeling simulates the cavern responses forward in time from the initial cavern creation. The actual wellhead pressure histories of BC-15, 17, 18, 19, 20, 101, and 102 have been recorded since 1/1/1990 as shown Figure 24. Pressure drops occurred during workovers and fluid transfers. For the purposes of the present simulation, it is assumed that initial leaches of the caverns started on 1/1/1989 and the caverns were leached to full size over a one-year period.

The peak wellhead pressures over 1000 psi in Figure 24 were created during mechanical integrity tests (MIT). To investigate well casing integrity for oil leakage, nitrogen gas is injected into the well. Nitrogen gas pressure at the wellhead causes pressure peaks because the nitrogen density is much smaller than oil density. The nitrogen gas pushes the oil-nitrogen interface (ONI) down to the casing shoe, so the nitrogen replaces the oil between the wellhead and ONI. The density difference between oil and nitrogen can be offset by increased wellhead pressure, and then the resulting cavern pressure is only slightly different than under normal oil wellhead pressure. The cavern volumetric closure rate due to salt creep depends on the difference between cavern internal and lithostatic pressures. The peak pressures due to MIT do not affect the cavern internal pressure much, so the peak pressures can be ignored. The wellhead histories in Figure 24 were modified for use in the simulation as shown Figure 25. The real wellhead pressure plus oil/brine pressure gradient were applied on the inside boundary of each SPR cavern.

The wellhead pressure of BC-101 was recorded since 6/1/1991, so it is assumed that the initial leach of BC-101 started on 6/1/1990 with a one year leaching period.

Boardwalk previously owned BC-102. The DOE purchased BC-102 to use for SPR in 2012. The wellhead pressure has been recorded since 11/9/2012. BC-102 was filled with ethane while operated by Boardwalk. We have no access to the Boardwalk pressure data during that time. In this simulation, it is assumed that the initial leaching of the cavern started on 1/1/1989, was leached to full size over a one-year period, and the wellhead pressure was kept constant at 900 psi during Boardwalk's operations until 11/8/2012. The recorded wellhead pressure since 11/9/2012 is applied in the simulation.

Figure 26 shows the wellhead histories, which consist of the actual (1/1/1990 - 7/17/2017) and the assumed future (7/18/2017 - 7/17/2047) pressure records used for SPR caverns in this simulation. The previous five-year (7/18/2010 - 7/17/2015) wellhead pressure history of each cavern as shown in Figure 25 is replicated to simulate the next five years (7/18/2017 - 7/17/2022), during which no drawdowns are assumed to take place, and the next five-year drawdown cycles thereafter (7/18/2022 - 7/17/2047). The next set of drawdown leaches is assumed to start at 7/18/2022.

BC-102 does not have an entire record for the previous five-year (7/18/2010 - 7/17/2015) period, so the two-year history (7/1/2014 - 11/8/2016) is replicated to make the assumed past history (7/1/2010 - 11/8/2012) as shown Figure 27. The assumed past and actual histories are assembled to make the five-year (7/18/2010 - 7/17/2015) history. The five-year history is replicated to simulate the next five years (7/18/2017 - 7/17/2022), during which no drawdowns are assumed to take place, and the next five-year drawdown cycles thereafter (7/18/2022 - 7/17/2047).

The actual wellhead pressure histories as shown Figure 25 are recorded at the oil-side wellhead, i.e. oil-side wellhead pressure. BC-20 is located near the edge of the salt dome. Its proximity close to the edge of the dome raises concerns about potential tensile failure in the surrounding rock near BC-20 induced by the cavern volume closure due to salt creep. Therefore, BC-20 is no longer used as an SPR cavern since 2/7/2013. At present, BC-20 is filled fully with brine rather than oil. The wellhead pressure history for BC-20 in Figure 26 is the brine-side wellhead pressure rather than oil-side since 2/7/2013. The previous three-year (8/1/2014 - 7/17/2017) wellhead pressure history of BC-20 is replicated for the future (7/18/2017 - 7/17/2047) simulation as shown in Figure 26.

Before a cavern's initial leach starts, the model has a stabilization period (1/1/1900 - 12/31/1988). To avoid the numerical shock, gravity is applied gradually into the mesh for ten seconds. After that, the model is allowed to consolidate with gravity for a simulation period of 89 years so that every element is stabilized numerically.

The analysis simulates caverns that were leached to full size over a one-year period by means of gradually switching from salt to fresh water in the caverns. It is assumed that the SPR caverns were filled with petroleum and non-SPR caverns are filled with either a liquid or gaseous petroleum product or brine after the initial leaching. Creep is permitted to occur over the entire simulation period (1/1/1990 - 7/17/2047). On 7/18/2022 and subsequently every 5 years thereafter, the SPR caverns are instantaneously leached to produce an increased volume of 15% during each leach cycle to simulate drawdowns. Modeling of the leaching process in the caverns is accomplished by deleting elements along the walls of the caverns so that the volume increased by 15% with each leach. Leaching is assumed to occur uniformly along the entire height of the cavern. However, loss of salt due to leaching in the floor or roof of the caverns is not simulated in the model. The 5-year period between each drawdown allows the stress state in the salt to return to a steady-state condition, as will be evidenced in the predicted closure rates. The simulation was run out to 7/17/2047 to investigate the structural behavior of the dome for 57 years, as the process of salt creep continues to reduce the caverns' volume.

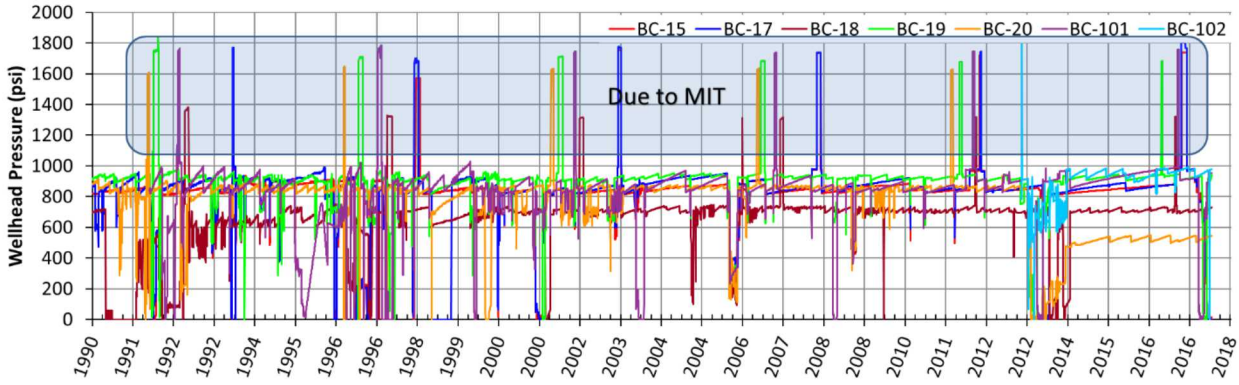

Figure 24. Wellhead pressure histories for the seven Bayou Choctaw SPR caverns provided by the field office

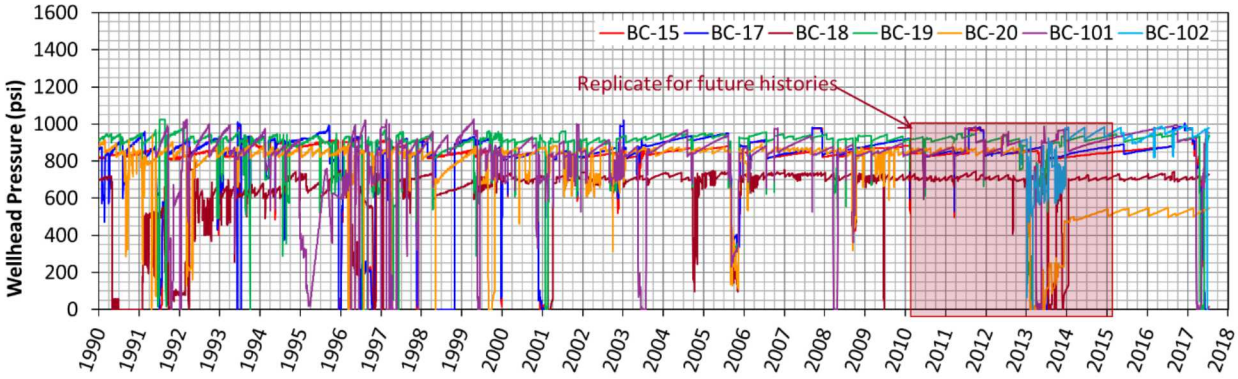

Figure 25. Modified wellhead pressure histories for the seven Bayou Choctaw SPR caverns

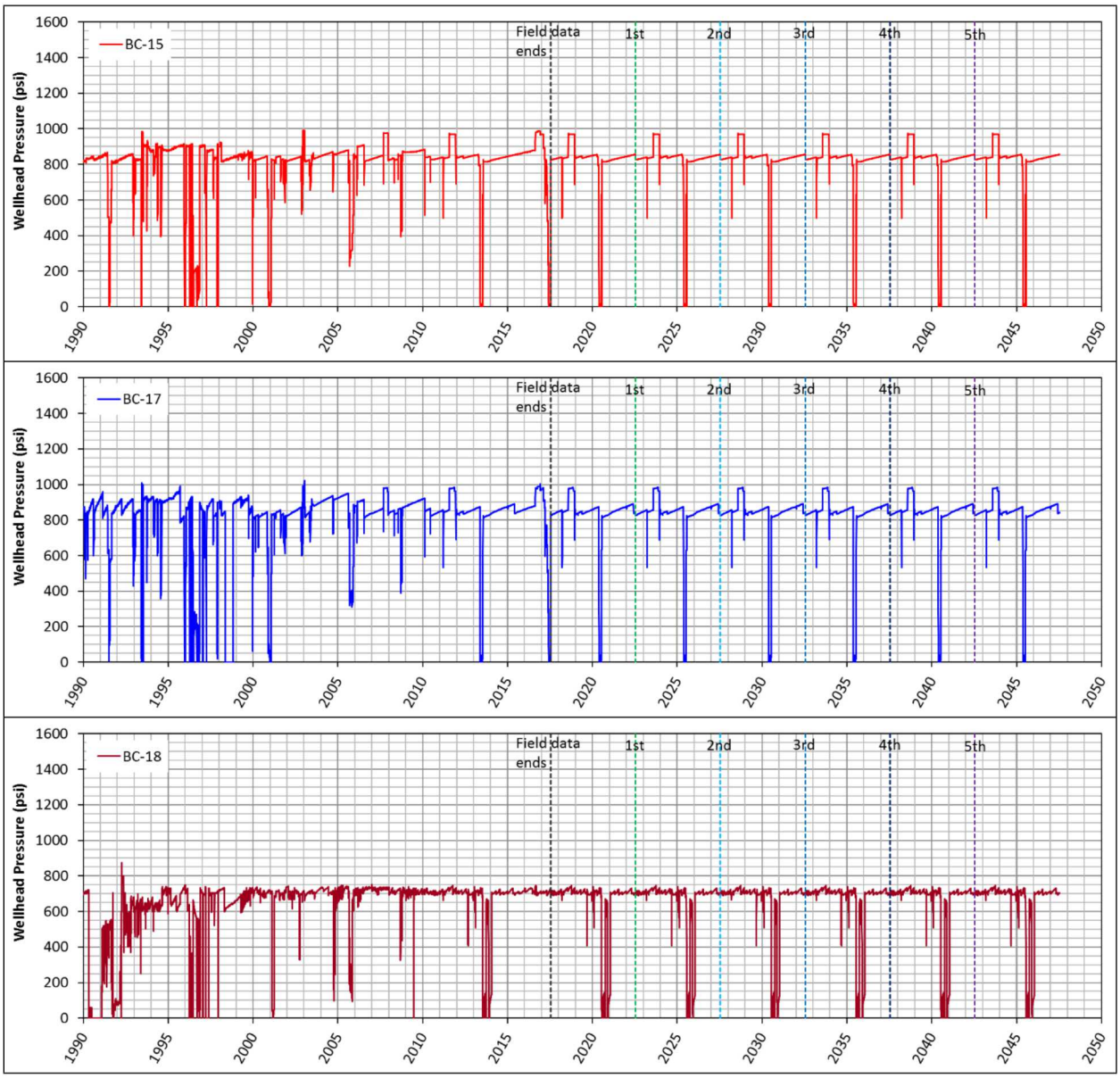

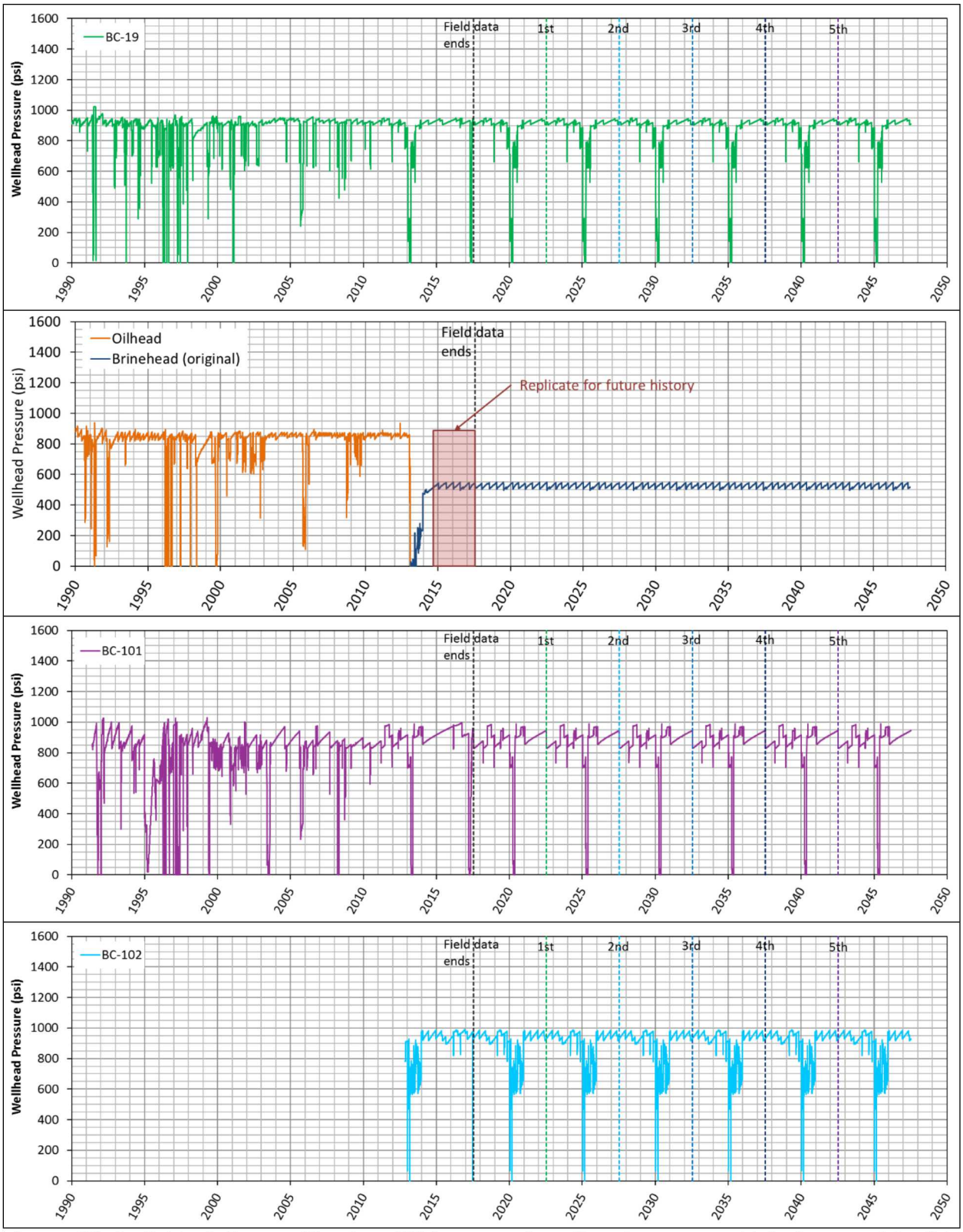

Figure 26. Individual Bayou Choctaw SPR caverns' wellhead pressure histories used in this analysis

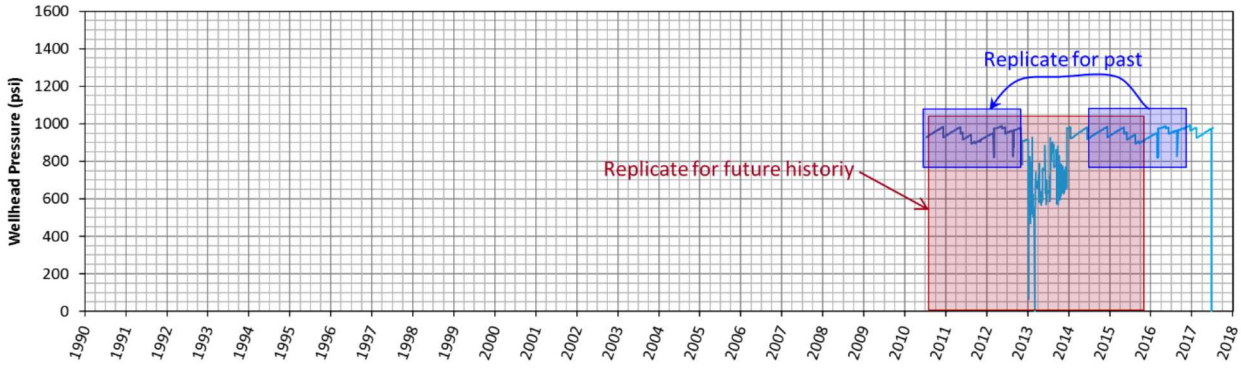

Figure 27. Replicate the two-year history for the past to make five-year replication

4.1.2. Boardwalk Caverns

BC-6, 16, 24, 25, 26, 27, 28, J1, N1, and UTP1 are owned by Boardwalk. The wellhead pressure history data has not yet been provided by Boardwalk because of ongoing litigation between the U.S. government and Boardwalk. In this simulation, it is assumed that the initial leaches of the caverns started on 1/1/1989 and they were leached to full size over a one-year period. The wellhead pressure is assumed to be a constant 900 psi over time.

4.1.3. Abandoned Caverns

The abandoned caverns were all plugged with the exception of BC-4. The wellheads were cut off below the surface and buried.

The abandoned caverns were filled fully with brine before plugging. Figure 28 shows pressure distributions on the inside and outside of BC-1 before and after plugging as an example. The lithostatic pressure gradient with depth (1.0 psi/ft) is larger than the brine pressure gradient (0.52 psi/ft). The gradient difference drives the cavern volumetric closure due to salt creep. The brine volume does not decrease over time because there are no leaks, while the cavern volume decreases due to creep until an equilibrium state is reached. The hydrostatic pressure in the cavern increases until pressure equilibrium, i.e. the pressure head increases for some time after the plugging. The pressure head, which is an additional hydrostatic pressure due to the cavern volumetric closure, is calculated to be 578 psi at equilibrium [Park, 2017a]. In the same manner, the pressure heads of the abandoned caverns at equilibrium state are calculated as listed in Table 2. These values are used over time as wellhead pressures in the analysis. Although there are no more pressure increases after equilibrium is reached, pressure differences do occur on the top and bottom of cavern due to gradient with depth. Therefore, the bottom area shrinks (1504 psi vs. 1680 psi) while the top area expands (1119 psi vs. 942 psi) like a bubble, so a risk of fracturing in the roof could occur.

BC-4 still has a wellhead and is actively monitored with sonars and well logging runs. In addition, the area around BC-4 is monitored with GPS, tiltmeters, and subsidence surveys to detect any changes at the surface which may reflect degrading conditions underground. It cannot hold fluid due to communication with the caprock, so zero wellhead pressure is conservatively applied in the analysis.

BC-7 was drilled in 1942 to a depth of 1951 ft. The depth to the original top of the cavern is not known. The cavern volume was calculated from production data to be 2.9 MMB. Normal brining

operations continued into the early 1950's when cavern pressure was lost. It is assumed that pressure was lost when the cavern roof was leached to the top of the salt. Brining continued by the airlift method until January 1954 when the cavern collapsed. This resulted in the formation of a crater about 800 ft in diameter which filled with water and is now called Cavern Lake. The measured depth of the lake was 100 ft in 1956 [The Aerospace Corporation, 1980]. The lake depth is small relative to the model height (6400 ft) and the lake diameter (about 800 ft) is large relative to the lake depth, so the lake is regarded in this model as a part of the surface and its geometry is simplified as flat. The cavern's collapse resulted from leaching of the salt to the salt/caprock contact followed by the failure of the caprock and overlying sediments [Hogan, 1980]. Cavern BC-7's collapse began at the well-head and the void filled with overburden [Hogan, 1980; Neal et al., 1993]. In this model, it is assumed that the cavern volume no longer decreases due to salt creep because the overburden material in the cavern void has been compacted by salt lithostatic pressure to be able to counteract the salt's movement. Therefore, the cavern internal is regarded as a solid made of overburden material in this model.

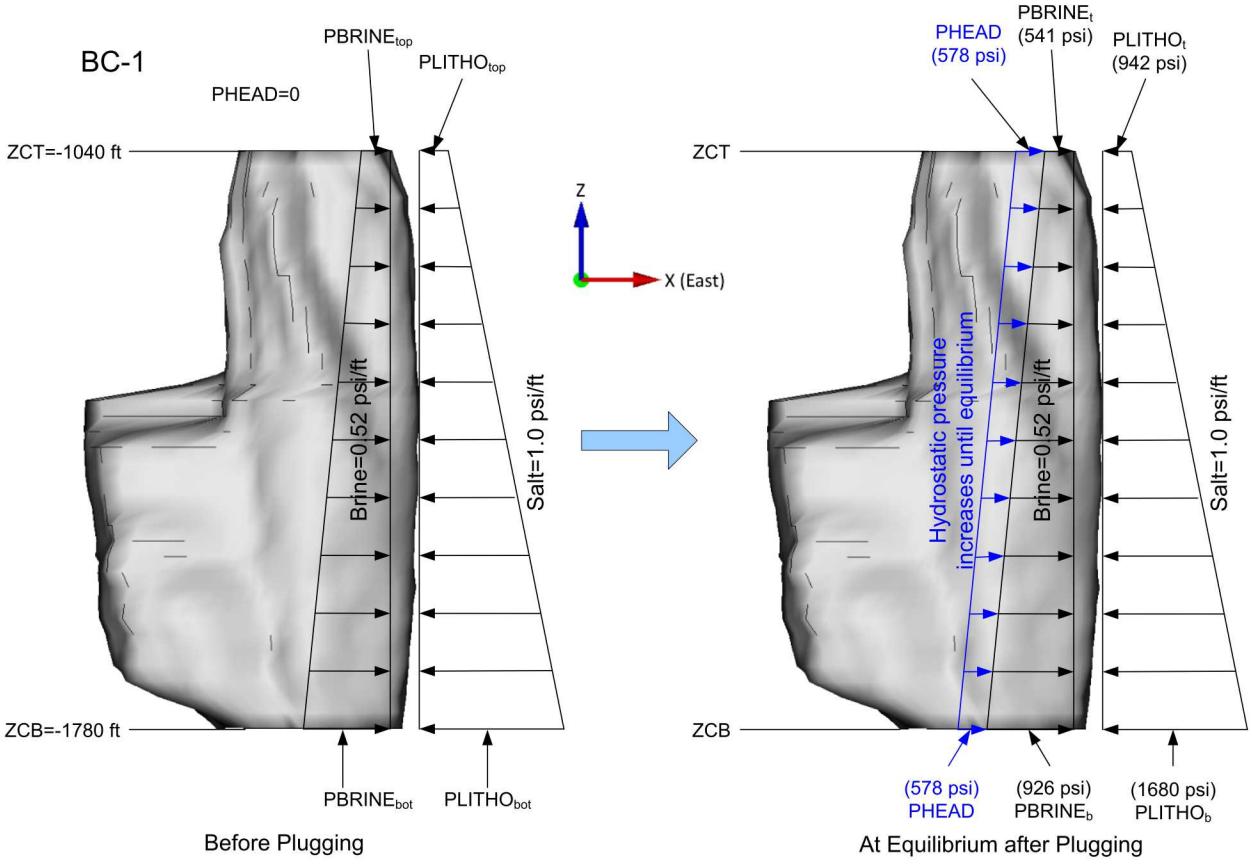

Figure 28. Pressure distribution change before and after plugging in BC-1

Table 2. Calculated pressure heads for the abandoned caverns at equilibrium [Park, 2017a]

Cavern ID	Depth of cavern top (ft)	Depth of cavern bottom (ft)	Lithostatic pressure at cavern top (psi)	Lithostatic pressure at cavern bottom (psi)	Brine pressure at cavern top (psi)	Brine pressure at cavern bottom (psi)	Pressure head at equilibrium (psi)
BC-1	-1040	-1780	942	1680	541	926	578
BC-2	-780	-1520	683	1421	406	791	454
BC-3	-1020	-1840	922	1740	531	957	587
BC-8	-1300	-1960	1202	1860	676	1020	683
BC-10	-1000	-1980	902	1880	520	1030	616
BC-11	-1080	-1740	982	1640	562	905	578
BC-13	-1120	-1860	1022	1760	583	968	616

4.2. Oil-Brine Interface

4.2.1. SPR Caverns

Previous analyses [Part et al., 2006; Park and Ehgartner, 2008; Park and Ehgartner, 2010] assumed that the SPR caverns were filled fully with oil. In actuality, the caverns were not always fully filled with oil. Brine fills the bottom of the caverns, and the proportion changes with time depending on cavern operations. The difference between pressure gradients of oil (0.37 psi/ft of depth) and brine (0.52 psi/ft of depth) cannot be ignored [Park, 2017a]. Therefore, the amount of oil and brine in a cavern over time needs to be considered. Figure 29 shows the oil-brine interface (OBI) depth history of SPR caverns used in this analysis. Historical data (1/1/1990 – 7/17/2017) were obtained from the BC field office. It is assumed that the OBI depth of each cavern does not change after 7/17/2017 for the rest of the simulation. As for BC-20, the OBI depth is zero ft (surface) since 2/7/2013, because it is filled fully with brine even the brine-side wellbore.

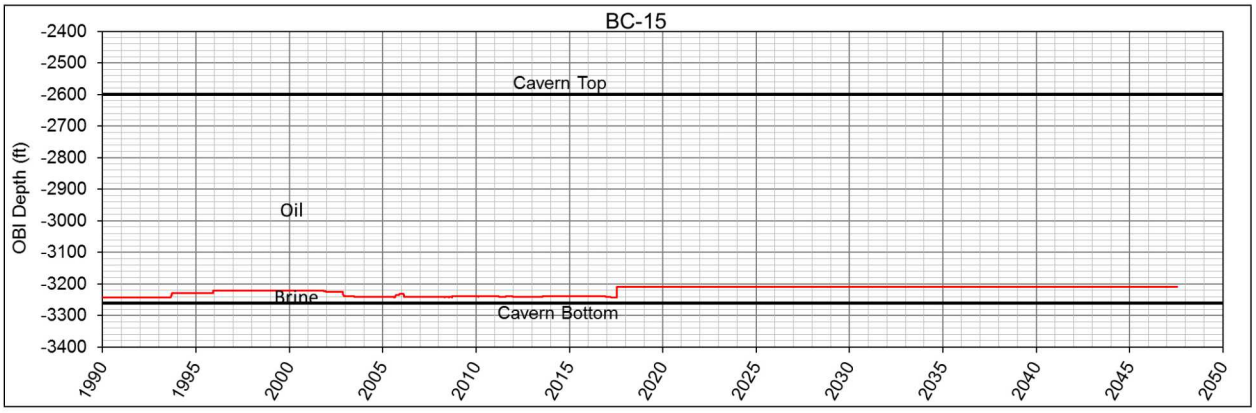

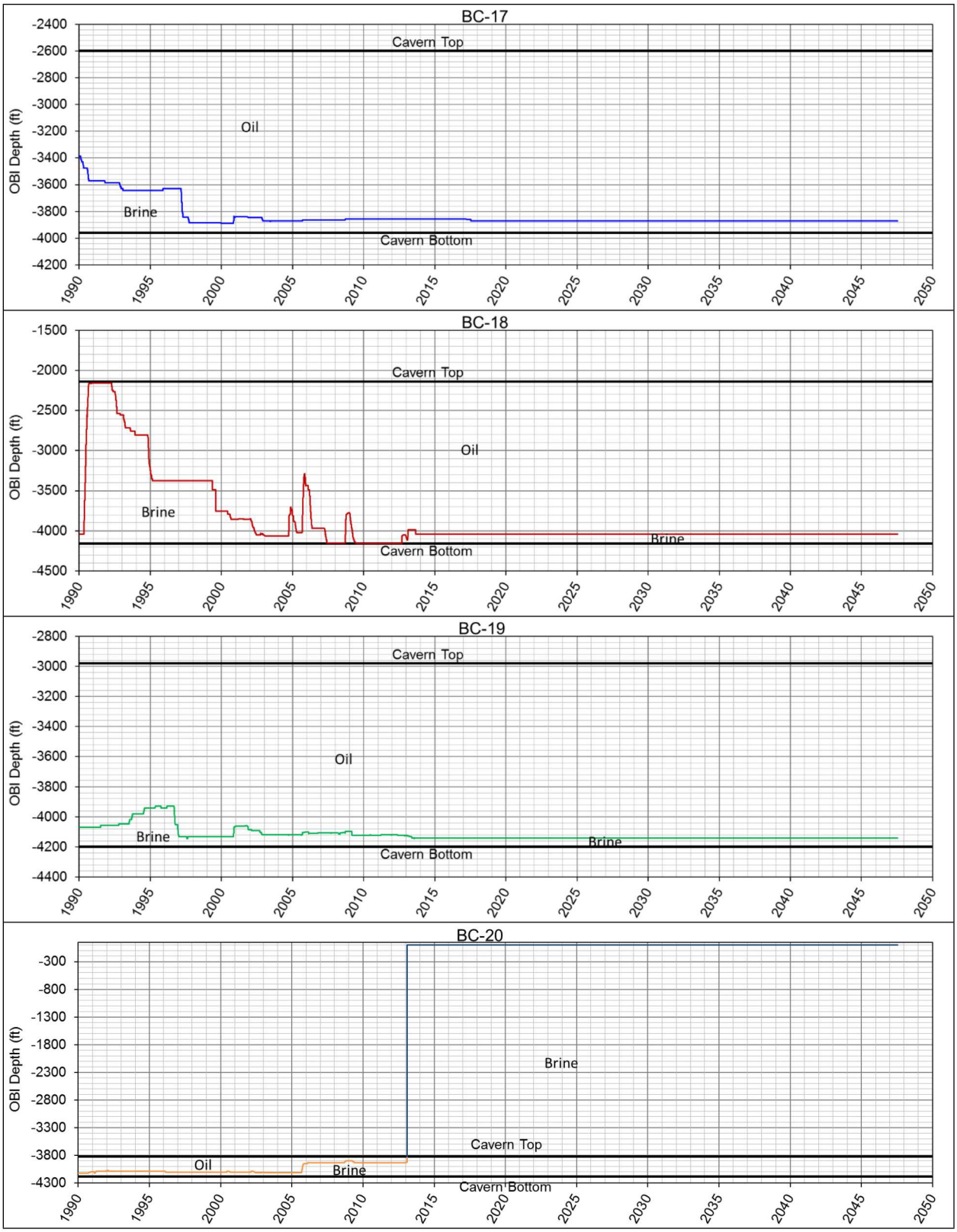
BC-17
Cavern Top
Oil
Brine
Cavern Bottom
OBI Depth (ft)
-2400
-2600
-2800
-3000
-3200
-3400
-3600
-3800
-4000
-4200
1990
1995
2000
2005
2010
2015
2020
2025
2030
2035
2040
2045
2050
BC-18
Cavern Top
Oil
Brine
Brine
Cavern Bottom
OBI Depth (ft)
-1500
-2000
-2500
-3000
-3500
-4000
-4500
BC-19
Cavern Top
Oil
Brine
Brine
Cavern Bottom
OBI Depth (ft)
-2800
-3000
-3200
-3400
-3600
-3800
-4000
-4200
-4400
BC-20
Brine
Cavern Top
Oil
Brine
Cavern Bottom
OBI Depth (ft)
-300
-800
-1300
-1800
-2300
-2800
-3300
-3800
-4300

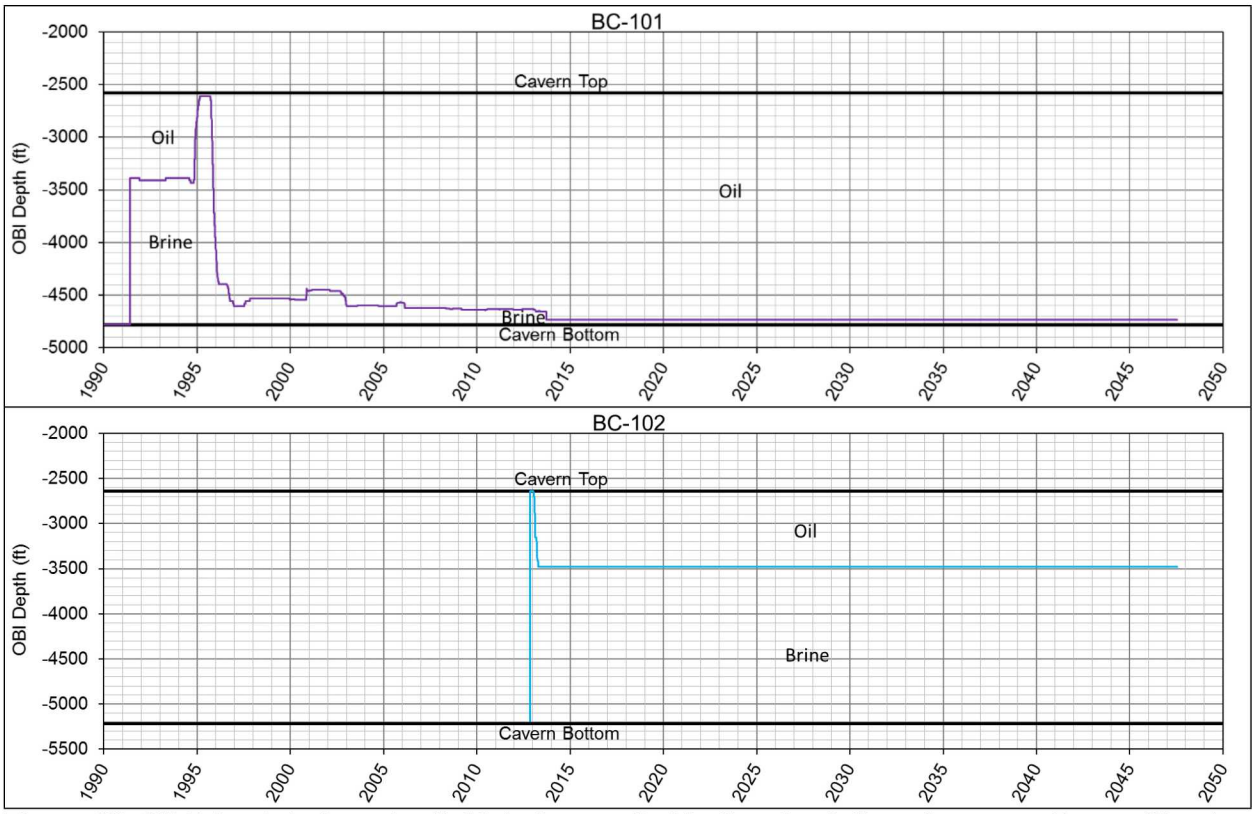

Figure 29. Oil-Brine Interface depth histories applied in the simulations for seven Bayou Choctaw SPR caverns

4.2.2. Boardwalk Caverns

BC-6, 16, 24, 25, 26, 27, 28, J1, N1, and UTP1 are owned by Boardwalk. The wellhead pressure history data has not yet been provided by Boardwalk, due to ongoing litigation between the U.S. government and Boardwalk. In this simulation, it is assumed that the initial leaches of the caverns started on 1/1/1989, that the caverns were leached to full size over a one-year period, and that the wellhead pressure was a constant 900 psi over time. The products held within Boardwalk caverns and their pressure gradients with depth applied in the analysis are listed below in Table 3.

Table 3. Products held within Boardwalk caverns and pressure gradient of depth

Cavern ID	Product	Pressure gradient with depth (psi/ft)
BC-6	Propylene	0.22
BC-16, N1, UTP1	Ethylene	0.54
BC-24	Natural gas	0.18
BC-J1	Ethane	0.25
BC-25, 26, 27, 28	Brine	0.52

4.3. Temperature

The finite element model includes a depth-dependent temperature gradient which starts at 84.0°F (28.9°C) at the surface and increases at the rate of 1.38°F/100 ft (2.51°C/100 m). The temperature profile is based on the average temperature data recorded in well logs from BC prior to leaching [Ballard and Ehgartner, 2000]. The temperature distribution is important because the creep response of salt is temperature dependent. Radial temperature gradients due to cavern cooling effects from the cavern contents are not considered in these calculations. Previous 2D cavern studies have shown the predicted cavern deformation to be insensitive to the developed radial thermal gradients [Hoffman, 1992].

4.4. Boundary Condition

Figure 30 shows the assembled mesh and the boundary conditions. The lengths of the confining boundaries are 11,000 ft in the N-S direction and 12,000 ft in the E-W direction. The boundary dimensions are determined by more than two times of the dome's range in each direction. The salt dome is modeled as being subject to a regional far-field stresses acting from an infinite distance away. The sizes of the caverns are horizontally much smaller than the dome. Therefore, the North and South sides of far-field boundary are fixed in Y-direction, and the East and West sides are fixed in X-direction. The bottom is fixed vertically. The top surface and four sides are vertically free. The acceleration of gravity used in the model is 9.81 m/s^2 (32.174 ft/s^2).

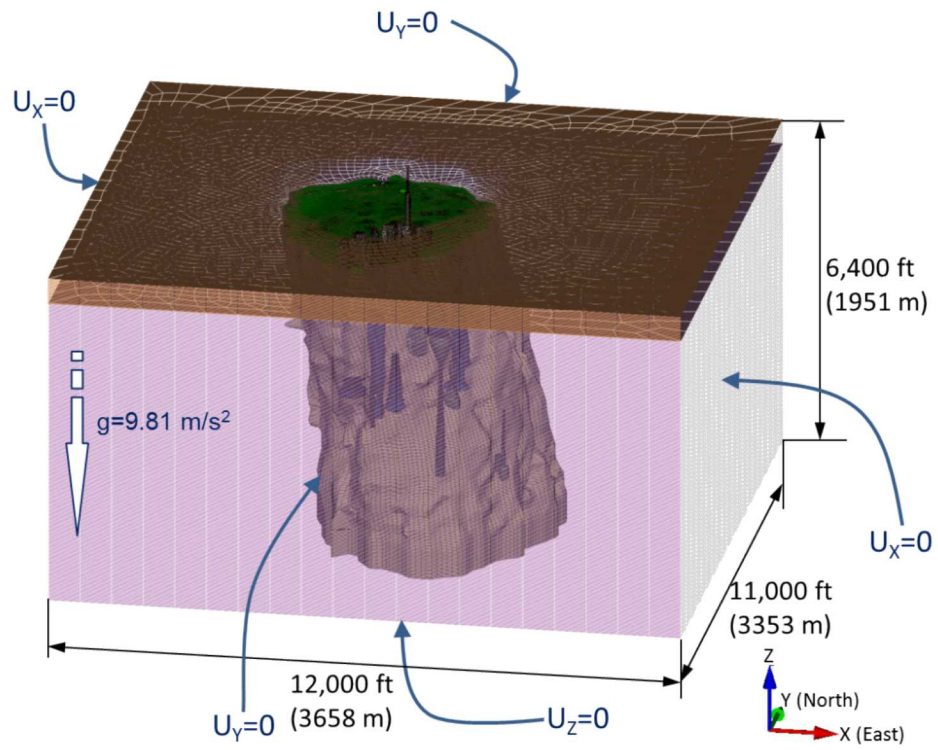

Figure 30. Boundary conditions of Bayou Choctaw Model

5. MATERIAL AND PROPERTIES

5.1. Salt

Creep is the time-dependent deformation of a material. Traditionally, a creep curve is thought to consist of three stages as shown in Figure 31. Experimental data obtained from a uniaxial stress laboratory creep test where the stress is held constant are typically of this form. In the first stage (primary), the creep rate decreases with time. In the second stage (secondary), the creep rate is constant (steady-state), and in the third stage (tertiary), the creep rate increases through progressive fracture formation and eventually terminates by failure of the specimen. Most uniaxial and triaxial compression tests do not reach the tertiary creep stage simply because of the amount of time required to get there. Empirically derived creep laws historically have described the shape of the creep curve through mathematical functions that consider the creep as the sum of transient and steady-state contributions. Transient creep is in general the response of the material to incremental and decremental stress changes. This definition, thus, includes the transient of primary creep response to the initial loading in a standard creep test [Munson and Dawson, 1982].

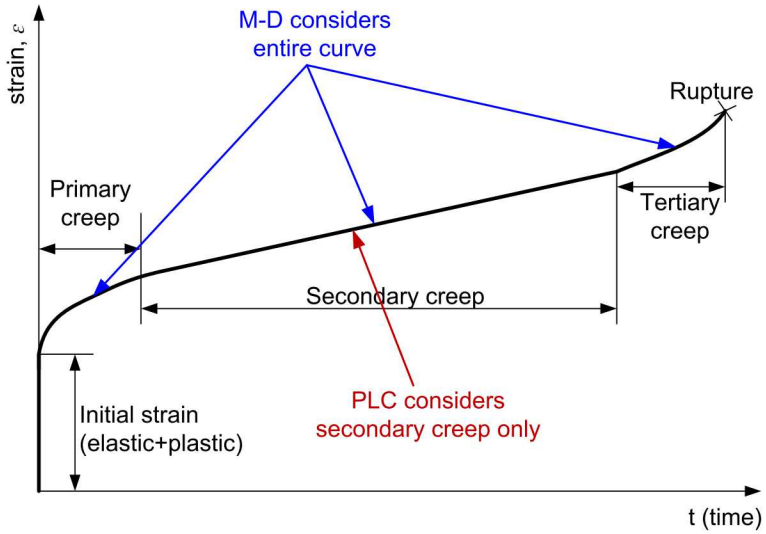

Figure 31. Comparison between M-D and Power Law Creep models

Principles gained from our understanding of the constitutive behavior of WIPP salt will form the principal basis for the analysis strategy. Not only do the constitutive equations of the M-D model define the necessary material parameters, but they also permit the formulation of rules of the analysis. In developing the constitutive description, we concern ourselves only with the temperature and stress range encountered in mining and storage cavern operations, typically low temperature and low to moderately high stresses. For these conditions, creep is envisioned as arising from the contributions of three appropriate micromechanical mechanisms as determined from salt deformation mechanism-map [Munson, 1979]. These mechanisms are (1) a dislocation climb controlled creep mechanism at high temperatures and low stresses, (2) an empirically specified, but undefined mechanism at low temperatures and low stresses, and (3) a dislocation slip controlled mechanism at high stresses [Munson, et al., 1989]. These mechanisms act in

parallel, which means the individual steady-state creep rates can be summed over the three mechanisms to give the total steady-state creep rate, as follows [Munson, 1998]:

$$\dot{\varepsilon}_s = \sum_{i=1}^{3} \dot{\varepsilon}_{s_i} \tag{1}$$

The steady-state creep rates for the individual mechanisms, respectively, are given by:

$$\dot{\varepsilon}_{s_1} = A_1 e^{-\frac{Q_1}{RT}} \left[\frac{\sigma}{\mu(1-\omega)}\right]^{n_1} \tag{2}$$

$$\dot{\varepsilon}_{s_2} = A_2 e^{-\frac{Q_2}{RT}} \left[\frac{\sigma}{\mu(1-\omega)}\right]^{n_2} \tag{3}$$

$$\dot{\varepsilon}_{s_3} = \left|H(\sigma-\sigma_0)\right| \left(B_1 e^{-\frac{Q_1}{RT}} + B_2 e^{-\frac{Q_2}{RT}}\right) \sinh\left[\frac{q\left(\frac{\sigma}{1-\omega} - \sigma_0\right)}{\mu}\right] \tag{4}$$

where the numerical subscripts refer to the appropriate mechanism, the A's and B's are structure factors, Q's are activation energies, R is the universal gas constant, T is the absolute temperature, μ is the shear modulus, q is the stress constant, σ_0 is a stress limit, and H is a Heaviside step function with argument (σ - σ_0). It has been shown [Munson, et al., 1989] through multiaxial experiments that the proper equivalent stress measure is $\sigma = |\sigma_1 - \sigma_3|$.

The equivalent total strain rate is treated through a multiplier on the steady-state rate, as

$$\dot{\varepsilon}_{eq} = F\dot{\varepsilon}_s \tag{5}$$

where the multiplier involves three branches of the transient creep curve: work-hardening, steady-state, and recovery, respectively, as follows:

$$F = \begin{cases} e^{\Delta\left(\left(1-\frac{\zeta}{\varepsilon_t^*}\right)^2\right)} & ;\ \zeta < \varepsilon_t^* \\ 1 & ;\ \zeta = \varepsilon_t^* \\ e^{-\delta\left(\left(1-\frac{\zeta}{\varepsilon_t^*}\right)^2\right)} & ;\ \zeta > \varepsilon_t^* \end{cases} \tag{6}$$

Here, Δ is the work-hardening parameter, δ is the recovery parameter, ζ is the state parameter, and ε^*_t is the transient strain limit. The state parameter rate is given by

$$\dot{\zeta} = (F-1)\dot{\varepsilon}_s \tag{7}$$

The transient strain limit is defined by

$$\varepsilon_t^* = K_0 e^{cT} \left(\frac{\sigma}{\mu(1-\omega)}\right)^m \tag{8}$$

where K_0 and c are constants and m is a material constant.

The work-hardening, Δ, and recovery, δ, parameters are described through linear functions, as follows:

$$\Delta = \alpha_w + \beta_w \log \frac{\sigma}{\mu(1-\omega)} \quad (9)$$

$$\delta = \alpha_r + \beta_r \log \frac{\sigma}{\mu(1-\omega)} \quad (10)$$

where the α's and β's are constants. Throughout these equations, although it is taken as zero for our purposes here, ω is the damage parameter.

Table 4. Parameter values used in ADAGIO input deck [Park, 2017a]

Mechanism	Parameter	Symbol	Unit	Values in Input Deck
Conventional	Gravity	gr	ft/s^2	32.174
	Universal gas constant	R	cal/(mol·K)	1.986
	Temperature	T	K	Varies with depth*
	Density	ρ/gr	lb·s^2/ft^4	4.4627** (2300 kg/m^3)
Elasticity	Young's modulus	E	psf	647447400 (31.0 GPa)
	Shear modulus	μ	psf	258978960 (12.4 GPa)
	Bulk modulus	K	psf	431631600 (20.7 GPa)
	Poisson's ratio	v	-	0.25
Dislocation climb controlled creep mechanism at high temperatures and low stresses (Eq. 2)	Structure factor	A_1	1/s	1.445×10^{22}
	Activation energy	Q_1/R	K	12588.89‡
	Stress exponent	n_1	-	5.5
Empirically specified but undefined mechanism at low temperatures and low stresses (Eq. 3)	Structure factor	A_2	1/s	***A2F***†×1.667×10^{12}
	Activation energy	Q_2/R	K	5035.55‡
	Stress exponent	n_2	-	5.0
Dislocation slip controlled mechanism at high stresses (Eq. 4)	Structure factor	B_1	1/s	1048941
	Structure factor	B_2	1/s	0.005229
	Stress limit	σ_0	psf	429613 (20.57 MPa)
	Stress constant	q	-	5335
Transient strain (Eq. 8)	Material constant	m	-	3.0
	Constant	K_0	-	***K0F***††×62750
	Constant	c	1/K	0.009198
Work-hardening and recovery (Eq. 9&10)	Constant	α	-	-17.37
	Constant	β	-	-7.738
	Recovery	δ	-	0.58
	Damage	ω	-	0.0
Structure factor multiplication factor from WIPP 25°C salt		*SMF*	-	0.172353
Scalar multiplier of time step needed for stability		*AMULT*	-	0.95
System parameters for numerical convergence		*ANGLE*	-	0.1
		epstol	-	0.005
		grwfac	-	1.05
		shkfac	-	1.0
		ITHPE		0.0

Note:
- * – Temperature value is assigned on every node in the mesh
- ** -The value (lb/ft^3/gr) will be multiplied by gravity in the system
- ‡ – ADAGIO requests the value be divided by universal gas constant
- † – A_2 multiplication factor to examine the A_2 factor effect

- †† - K_0 multiplication factor to examine the K_0 factor effect

The values of *A2F* and *K0F* have been calibrated through a number of back-fitting analyses and determined as listed Table 5.

Table 5. Multiplication factors applied to the A_2 and K_0 values listed in Table 4 [Park, 2017a]

Cavern ID	*A2F*	*K0F*
Salt except SPR cavern skin layers	**10.0**	**0.10**
BC-15 salt skin layers	0.01	0.03
BC-17 salt skin layers	0.12	0.10
BC-18 salt skin layers	0.04	0.03
BC-19 salt skin layers	10.0	0.10
BC-20 salt skin layers	25.0	0.03
BC-101 salt skin layers	10.0	0.10
BC-102 salt skin layers	10.0	0.10

5.2. Lithologies Encompassing Salt

An elastic model is assumed for the lithologies encompassing the salt dome. The surface overburden layer, which is mostly comprised of sand, is assumed to exhibit elastic material behavior. The sand layer is considered isotropic, and has no assumed failure criteria. The values of the required model parameters for the overburden are not available for BC, so the McCormick Ranch Sand properties used in the West Hackberry (WH) analysis [Ehgartner and Sobolik, 2002] were used. The caprock layer, consisting of gypsum, anhydrite and sand, is also assumed to behave elastically. Samples of caprock from core holes at BC were tested by Dames and Moore [1978] to determine physical properties. The tested samples were from massive gypsum-anhydrite units at depths of 602 ft and 645 - 648 ft in Core Hole 1 and 558 - 642 ft in Core Hole 2 [Hogan, 1980]. The rock surrounding the salt dome is sedimentary rock that consists mostly of sandstone and shale, which is assumed isotropic, homogeneous, elastic rock. The values of the required model parameters of the surrounding rocks are also not available. Typical values for the Young's moduli of sandstones and shales range from 6×10^4 to 1×10^7 psi [Carmichael, 1984]. For simplifying the analysis, a median value of the Young's modulus of sandstone, 5.076×10^6 psi, is assumed. The mechanical properties used in the present analysis are listed in Table 6.

Table 6. Material properties of the lithologies encompassing the salt dome used in the analysis [Park et al., 2006]

	Unit	Overburden	Caprock	Surrounding Rock
Young's modulus	psf	2.0885×10^6 (0.1 GPa)	3.2832×10^8 (15.72 GPa)	7.3099×10^8 (35.0 GPa)
Density	lb/ft^3	116.99 (1874 kg/m^3)	144.77 (2319 kg/m^3)	156.07 (2500 kg/m^3)
Poisson's ratio	-	0.33	0.288	0.33

5.3. Interbed and Interface

The interbed and interface are pseudo-materials which represent contact surface. ADAGIO has a contact surface algorithm for modeling contact and sliding behavior between two solid surfaces. However, this algorithm has a limitation on the number of elements in the model. The current

model is over that limitation. In place of a contact surface, a thin soft layer of elements is used for the interbed between the caprock and salt top. The thin soft element layer uses the overburden material properties and is assumed to behave mechanically like a contact surface with friction coefficient of 0.2 from a perspective of relative displacement between two lithologies. Thus the overburden material properties (Table 7) are used for the interbed layer.

The interface between the dome and surrounding rock is a vertical layer, while the interbed is a horizontal layer. In this analysis, it is assumed that the interface behaves like a thin soft element layer in a manner similar to the interbed, but the horizontal pressure applied on the dome surface has to be the same as it arise from the surrounding rock. Therefore, the density and Poisson's ratio of the surrounding rock are used for the pseudo material of the interface. To implement a soft element, 1% of the surrounding rock's elastic modulus is used for the interface. The mechanical properties used in the analysis are listed in Table 7.

Table 7. Material properties of the interbed and interface used in the analysis [Park, 2017a]

	Unit	Interbed	Interface
Young's modulus	psf	2.0885×10^6 (0.1 GPa)	7.3099×10^6 (0.35 GPa)
Density	lb/ft^3	116.99 ($1874\ kg/m^3$)	156.07 ($2500\ kg/m^3$)
Poisson's ratio	-	0.33	0.33

6. SALT DAMAGE CRITERIA

Potential damage to or around the SPR caverns was evaluated based on two failure criteria: dilatant damage and tensile failure.

Dilatancy is attributed to micro-fracturing or changes in the pore structure of the salt, resulting in an increase in permeability. A dilatancy is considered as the onset of damage to rock salt. A dilatant damage criterion is used to delineate potential zones of damage in the salt formation surrounding the SPR facility. Dilatant damage criterion typically relates two stress invariants to access failure and/or dilation of pressure-dependent materials: the first invariant of the Cauchy stress tensor, I_1, and the second invariant of the deviatoric stress tensor, J_2. These two invariants are defined mathematically as:

$$I_1 = \sigma_1 + \sigma_2 + \sigma_3 \tag{11}$$

$$J_2 = \frac{(\sigma_1 - \sigma_2)^2 + (\sigma_2 - \sigma_3)^2 + (\sigma_3 - \sigma_1)^2}{6} \tag{12}$$

where, σ_1, σ_2, and σ_3 are the maximum, intermediate, and minimum principal stresses, respectively.

Two reports [Price, et. al, 1981; Ingraham et al., 2014] contain the triaxial extension test data to determine the dilatant criterion of the BC salt as listed in Table 8. The experimental dilatant strengths listed in Table 8 are plotted in I_1–$\sqrt{J_2}$ space as shown Figure 32. Exponential fitting-curve to the data is defined by the following equation:

$$\sqrt{J_2} = a \cdot e^{n \cdot I_1} + c \tag{13}$$

The values of the parameters are calculated as follows:

a = -17210 psi

n = -1.086 x 10^{-5} (1/psi)

c = 17359 psi

A dilatant damage factor (*DF*) for the BC salt can then be defined by:

$$DF = \frac{a \cdot e^{n \cdot I_1} + c}{\sqrt{J_2}} \tag{14}$$

If $DF \le 1$, the shear stresses in the salt ($\sqrt{J_2}$) are large compared to the mean stress (I_1) and dilatant behavior is expected, i.e. the onset of dilatant damage is predicted to occur. If $DF > 1$, the shear stresses are small compared to the mean stress and dilatancy is not expected.

For purpose of these analyses, the tensile strength of the salt is conservatively assumed to be zero in order to check for tensile failure. Tensile cracking in rock salt initiates perpendicular to the largest tensile stress direction. The potential for tensile failure exists if the maximum principal stress (σ_1) is numerically zero or tensile (positive value of σ_1). To calculate the dilatancy damage and tensile failure potential in salt, the post-processing code ALGEBRA is used with the output of the FE code ADAGIO to determine spatial locations of dilatant damage.

Table 8. Triaxial extension test data on BC rock salt [Price et al., 1981; Ingraham et al., 2014]

	Well I.D.	Depth (top of specimens, ft)	Dilation Stress State				References
			I_1		$J_2^{1/2}$		
			(MPa)	(psi)	(MPa)	(psi)	
Extension Test	BC019A	2582.0	1.8	259	0.9	124	Price et al., 1981
	BC019A	2579.0	19.0	2760	5.0	727	Price et al., 1981
	BC102B	1068.9	89.1	12923	17.4	2518	Ingraham et al., 2014
	BC102B	1077.4	62.1	9005	12.4	1792	Ingraham et al., 2014
	BC102B	1084.4	105.4	15286	23.2	3361	Ingraham et al., 2014
	BC102B	1090.8	92.4	13407	8.8	1278	Ingraham et al., 2014
	BC102B	1093.9	76.8	11136	17.8	2581	Ingraham et al., 2014

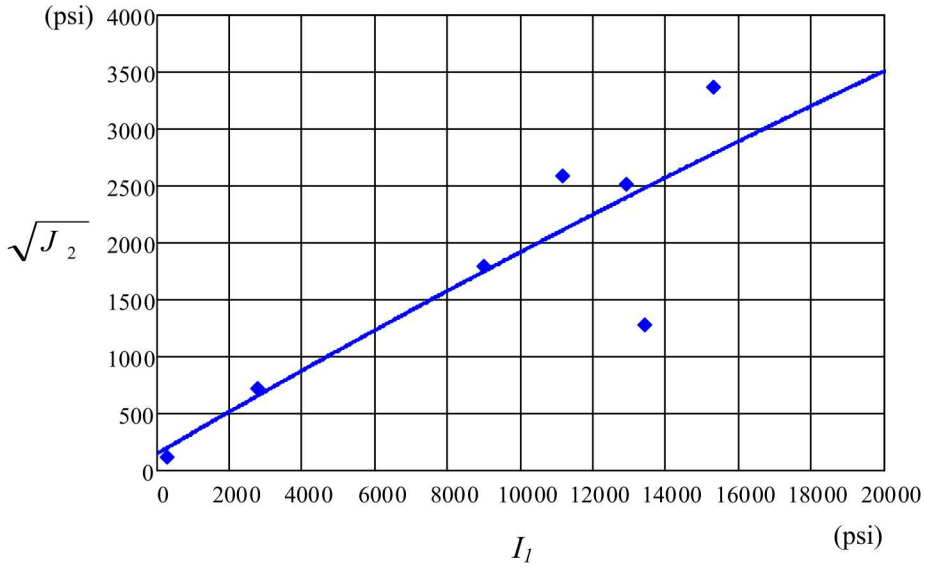

Figure 32. Dilatant damage criterion for Bayou Choctaw salt (Dots indicate experimental data)

7. ANALYSES RESULTS

7.1. Cavern 15 and 17

Caverns 15 and 17 have been identified by the Louisiana Department of Natural Resources (LADNR) as being within 200 ft of each other, thus requiring additional documentation of their suitability for continued safe operation as gas storage caverns. Because BC-15 and 17 have a thin web between them, the caverns are normally operated as a gallery, depressurized simultaneously in order to prevent unintended breaching of the wall and uncontrolled coalescence of the caverns [Sobolik et al., 2014].

Modeling of the leaching process of the caverns is performed by deleting a pre-meshed block of elements along the walls of the cavern so that the cavern volume is increased by 15 percent per drawdown as mentioned in Section 3.4.4. The pillar between BC-15 and 17 is shown for illustrative purposes in Figure 33. The pillar does not include the skins in Figure 16 and Figure 17 because the analysis results in the skins will be shown as those surrounding two caverns. A quick way to evaluate the potential for damage is by the use of history plots of the extreme values of maximum principal stress (σ_1) and dilatant damage factor (*DF*) in the salt surrounding two caverns and the pillar through each of the drawdown leaching operation.

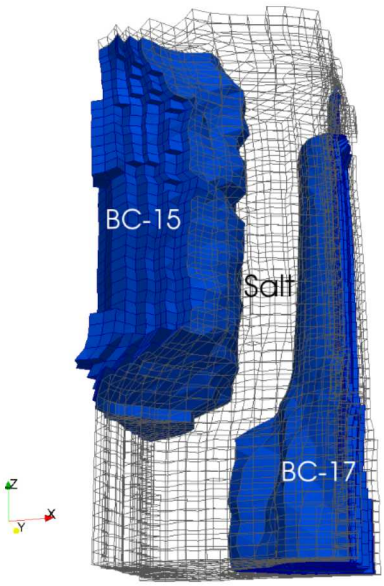

Figure 33. The pillar – the salt between BC-15 and 17 excluding skins shown in Figure 16 and Figure 17

Figure 34 and Figure 35 shows the predicted volumetric closure normalized to initial cavern volume, maximum σ_1, and minimum *DF* over time in the salt volume surrounding BC-15 and 17, respectively. In the numerical analysis, σ_1 is calculated in every element in the salt dome at each time step. The maximum σ_1 means the maximum value among all σ_1 values calculated in all elements in a specific volume (in this case, each skin layer and the pillar) at a specific time. In the plot, a positive value (+) indicates a tensile stress. In the similar manner, *DF* is calculated in every element in the salt dome at each time step. The minimum *DF* means the minimum value

among all *DF* values calculated in all elements in a specific volume at a specific time. As mentioned in Section 6, when $DF \leq 1$, the onset of dilatant damage is predicted to occur. Figure 38 shows the contour plots of *DF* on specific dates. Areas in a dilatancy damaged condition are shown in red.

The cavern volumes of BC-15 and 17 are predicted to decrease by 0.25% and 1.15%, respectively, over 32.5 years (1/1/1990 - 7/17/2022). The volume decrease of BC-15 is relatively smaller than other SPR caverns' because the cavern locates at the relatively shallow depth.

As for BC-15, the maximum σ_1 never reaches a positive or tensile value through three drawdowns, while the minimum *DF* is predicted to be less than 1 during every workover. The first *DF* less than 1 (calculated to be 0.9) occurs on 1/1/1996 during the third zero wellhead pressure (see Figure 26). The value dips below the threshold value of 1.0 that signifies the onset of dilatant damage, and does it for only a brief period (during a workover). The dilatant damaged areas in red are shown in the left panel of top row in Figure 38. The areas are located near the top of the cavern at the corner of the roof. The lowest predicted value for the minimum *DF* was 0.82 during a workover on 6/1/2020.

As for BC-17, the maximum σ_1 reaches a positive or tensile value (calculated to be 5) on 1/1/1996 during the third zero wellhead pressure (see Figure 26), and the minimum *DF* is predicted to be less than 1(calculated to be 0.76), simultaneously. The second positive maximum σ_1 with *DF* less than 1 occurs during the workover (5/19/2045 - 7/23/2045 as shown Figure 26). The areas in tensile stress state indicated by arrows are shown in Figure 37.

Figure 38 shows the contour plots of *DF* on specific dates to show the area (elements) in dilatant damage state in the cavern skin layers when the *DF*s are less than 1 during workovers. The dilatant damaged area (in red) increases with time in the both cavern skin layers. The contour plots for times 1996.00 through 2020.42 (no drawdown leach period) show the dilatant damaged area is growing even though the caverns are normally operated as a gallery, depressurized simultaneously. *This means we need to continue monitoring the cavern's behavior such as unexpected pressure down*.

The contour plots at times 2025.42, 2030.42, and 2035.42 show the dilatant damaged areas during the workovers for the 1st, 2nd, and 3rd drawdowns, respectively. The damaged area is growing rapidly. This means the drawdown leach affects obviously the cavern stabilities as we expected. The plot at 2045.50 shows the damaged area is still growing without drawdown after the 3rd drawdown.

The damaged areas on the walls of BC-15 and 17 tend to appear at the pillar side. This means the pillar sides of two caverns are relatively unstable structurally. The chimney and lobe of BC-17 are structurally unstable for the cavern pressure change. The plot at 1998.38 (the middle panel, top row) shows the *DF* contours when the workover (zero wellhead pressure) was conducted in BC-17 but not BC-15 (see Figure 26). The cavern skin layer color changes to blue ($DF > 2.5$), i.e. the damaged area disappears when the internal pressure in BC-15 returns to the normal operation's.

Figure 37 shows the contour plots of σ_1 on specific dates to show the area (elements) in tension in the cavern skin layers during workovers. The areas in tensile stress state are predicted to appear at 1996.00 and 2045.50 only. The areas are also under the dilatant stress condition. Therefore, salt fall potential is predicted to occur at the locations indicated by the arrows.

Figure 36 shows the predicted maximum σ_1, and minimum *DF* over time in the salt pillar as shown Figure 33. The maximum σ_1 never reaches a tensile (positive) value, and the minimum *DF* never reaches the dilatant damage stress state either until the end of the simulation. This means the inside of pillar is structurally more stable than the cavern skin layers. Therefore, we need to focus on the outside of pillar rather than the inside when examine the structural state. However, the predicted maximum σ_1 peak values increase toward positive, the minimum *DF* peak values decrease toward 1.0, i.e. the pillar is becoming structurally unstable with time.

No salt fall is expected between 1996 and 2045 because there is no tensile stressed area ($\sigma_1 > 0$) between them as shown Figure 35. However, the microcrack area increases with time as shown Figure 38, especially, at the chimney area of BC-17. BC-15 and 17 are normally operated as a gallery, depressurized simultaneously. If unexpected unbalanced internal pressures of two caverns occurs, the structural instability of the pillar between them may increase rapidly. Therefore, we need to continue carefully monitoring the cavern's behavior such as unexpected pressure drop. In conclusion, one drawdown leach could be allowed from a geomechanics perspective.

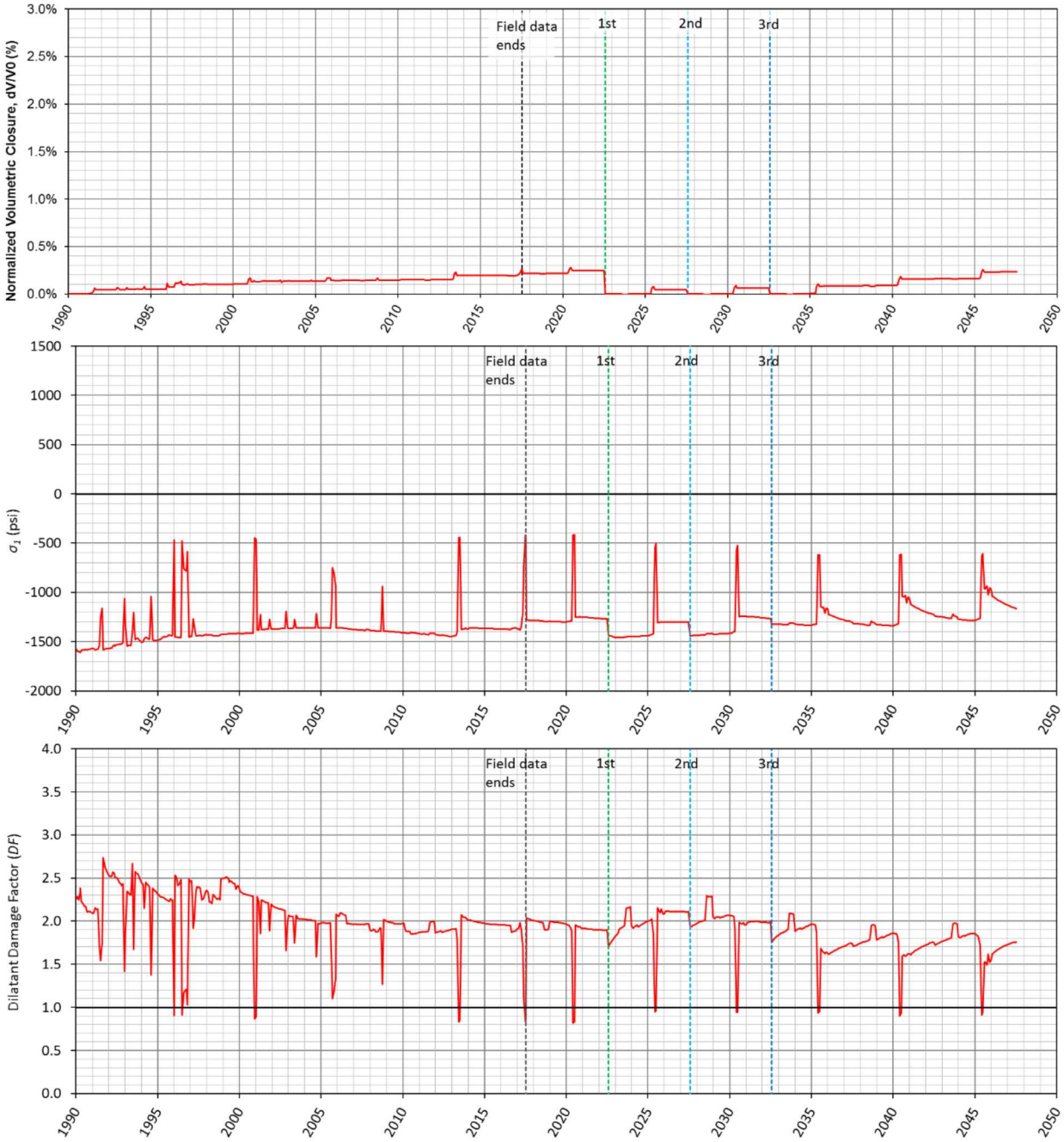

Figure 34. Predicted volumetric closure normalized to initial cavern volume of BC-15 (top), maximum σ_1 (middle) and minimum dilatant damage factor (bottom) over time in the salt surrounding BC-15

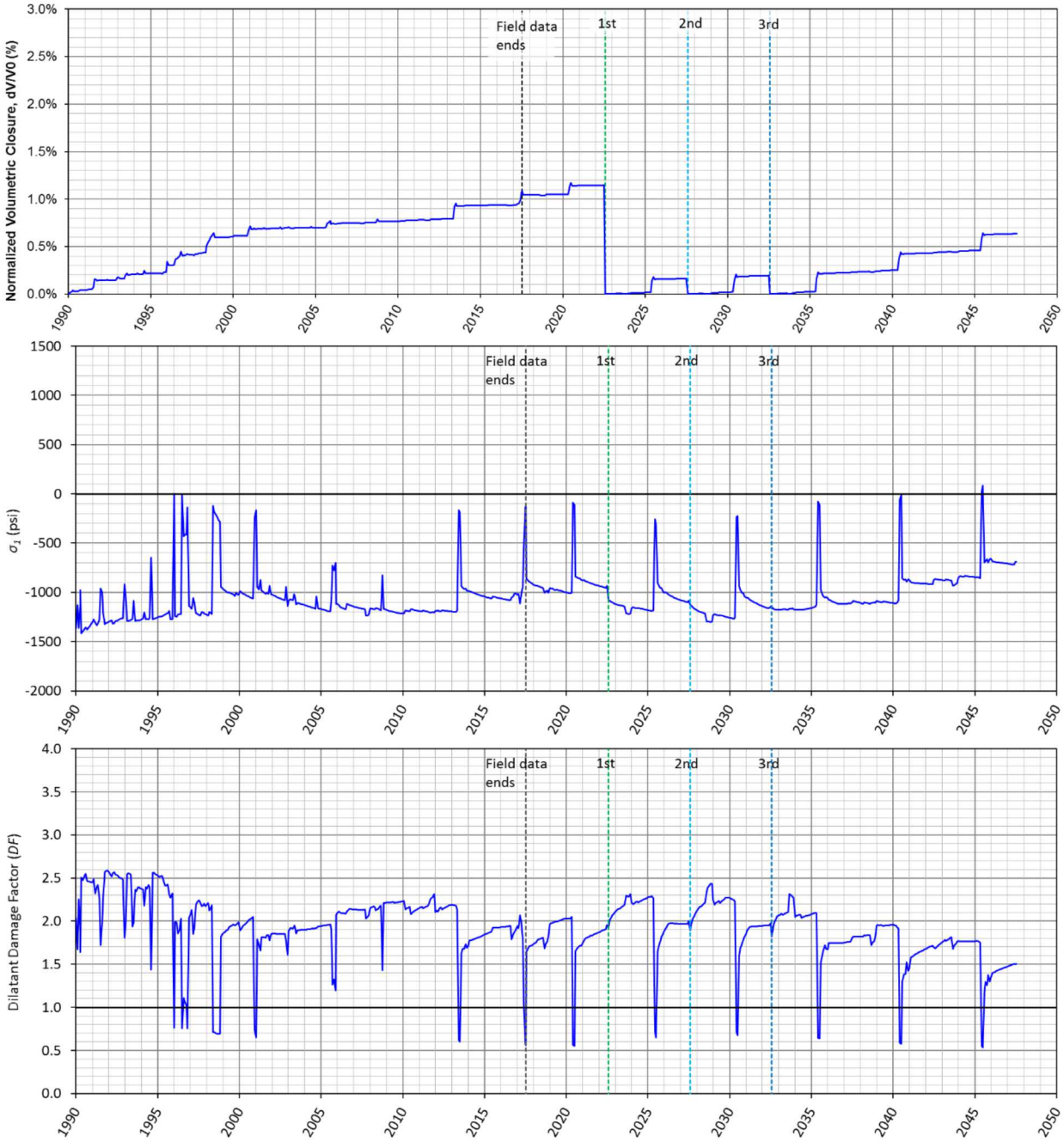

Figure 35. Predicted volumetric closure normalized to initial cavern volume of BC-17 (top), maximum σ_1 (middle) and minimum dilatant damage factor (bottom) over time in the salt surrounding BC-17

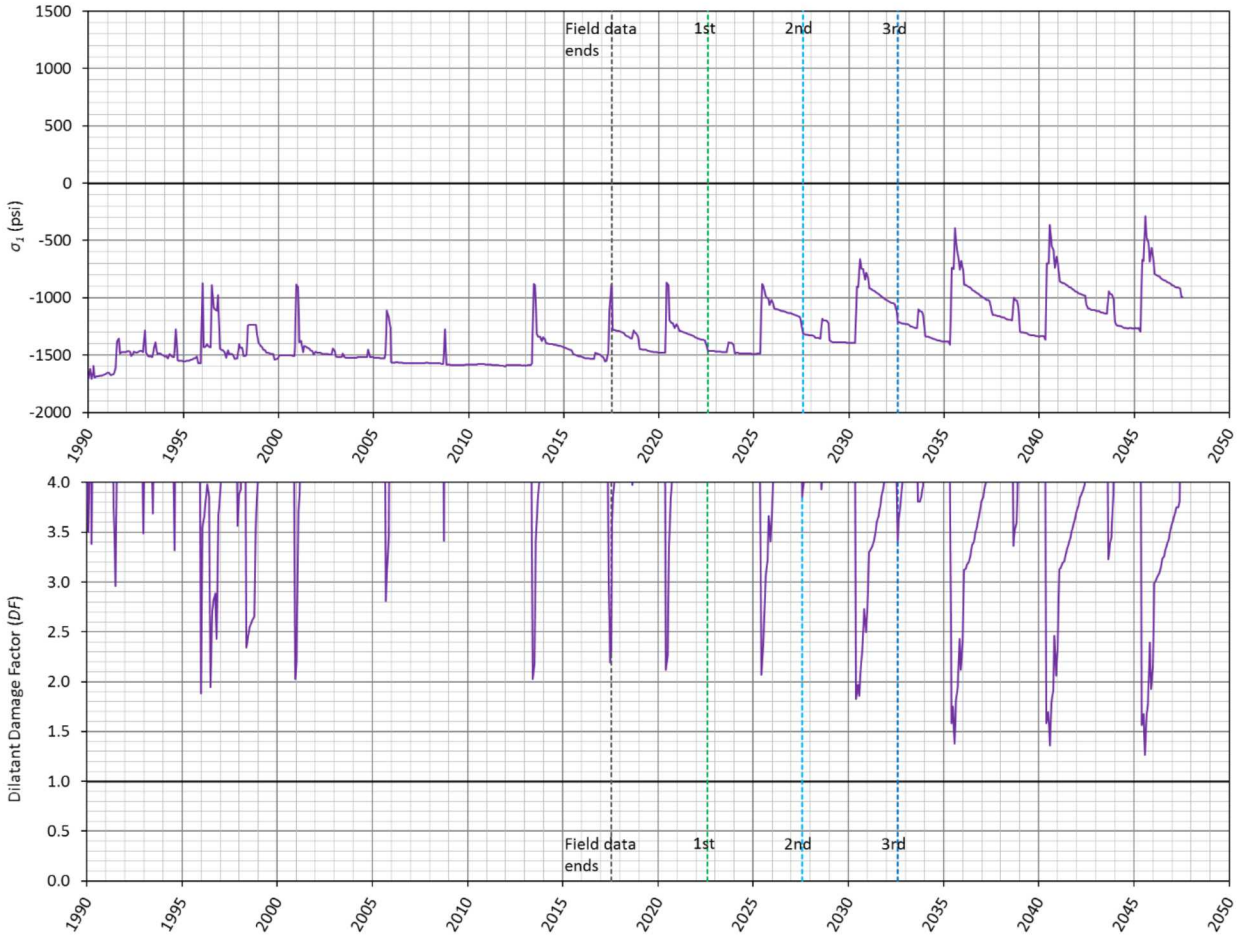

Figure 36. Predicted maximum σ_1 (top) and minimum dilatant damage factor (*DF*) over time in the pillar as shown Figure 33

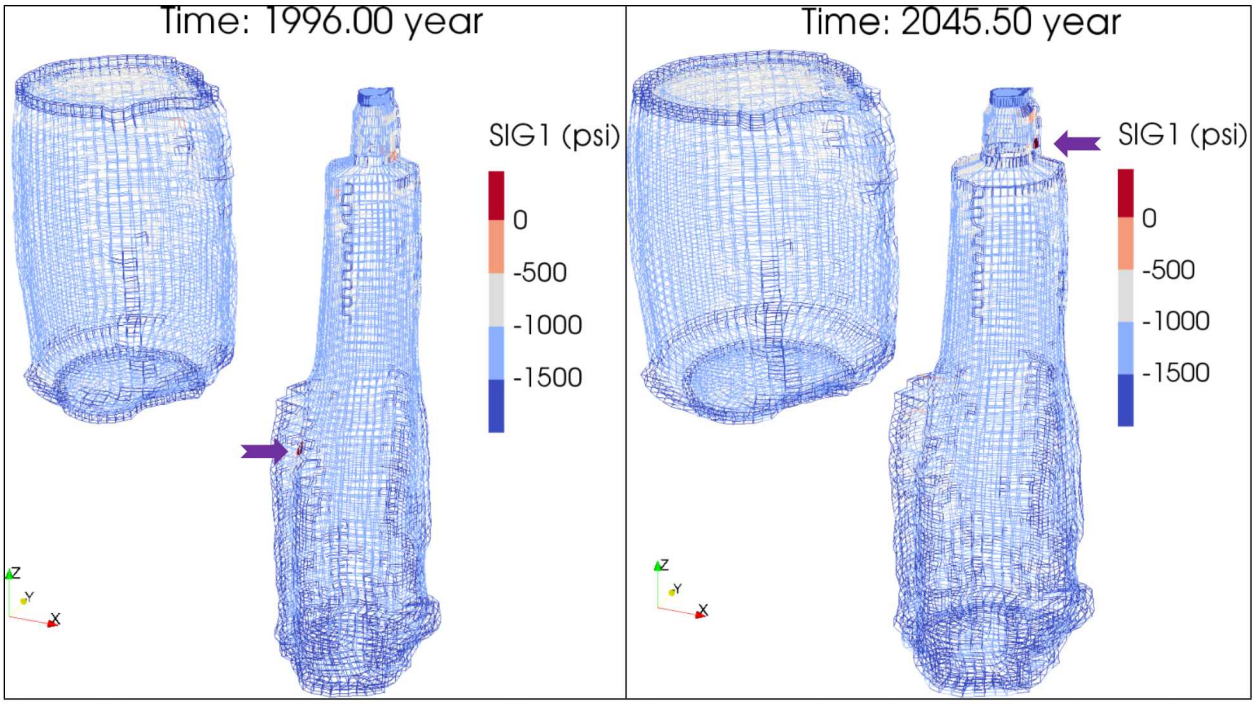

Figure 37. Contour plots of σ_1 on specific dates. Areas in tensile state are shown in red. Arrows are pointing to the tensile areas.

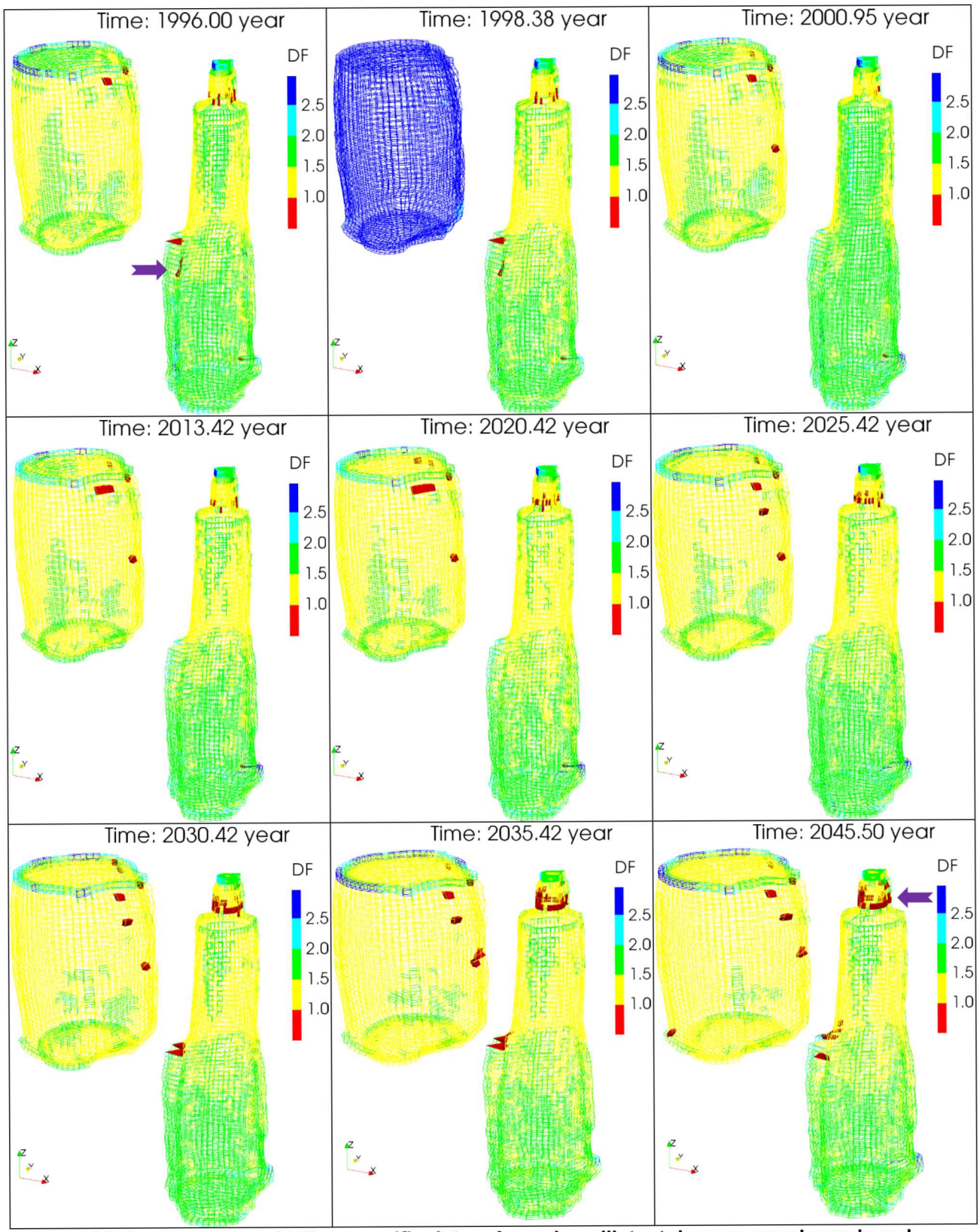

Figure 38. Contour plots of *DF* on specific dates. Areas in a dilatant damage are shown in red

7.2. Cavern 20

7.2.1. Cavern Volume Closure

BC-20 is close to the dome edge, so no drawdown leaching operations are allowed. At present, the brine-side wellbore is filled fully with brine rather than oil. Therefore, the cavern volume closure is calculated using the wellhead pressure and OBI depth changes, using the maximum wellhead pressure of 550 psi employed since 2013 as the future operating pressure.

Figure 39 and Figure 40 show the predicted volumetric closure normalized to initial cavern volume and the decrease in storage volume, respectively, in BC-20 over 57 years of time. The cavern volume decreases by 2.2%. The initial cavern cavity volume was 9.39 MMB on 1/1/1990 and is predicted to be 9.18 MMB on 7/17/2047. Note that the 1st, 2nd, etc., in the plots means the other SPR cavern's drawdown leach start dates, not for BC-20. Figure 41 shows the predicted cavern deformations multiplied by factor of 20 on 1/1/1990, 4/1/2017, and 7/17/2047, respectively. The 3D displacement at each node is calculated between 1/1/1990 and the specified dates. We see the cavern top and wall shrink inward with time. The surrounding rock is made of sandstone that is relatively stiff and does not creep. Since the surrounding rock is undergoing little deformation and the Cavern 20 is shrinking volumetrically as creep progresses, tensile stress may occur and increase over time in the salt between the dome edge and cavern wall.

The interface between the salt dome and surrounding sandstone is assumed competent. If this is indeed true, then it is more likely that the salt in the edge pillar will experience tensile stresses. However, if the interface is not competent, and consists of a rubblized mixture of salt, sandstone, and other materials, then salt creep may actually cause the material outside the interface to migrate inward with the creeping salt. This could also present a potential instability issue for BC-20. The assumption of a competent interface is sufficient for now to determine the potential for cavern instability problems.

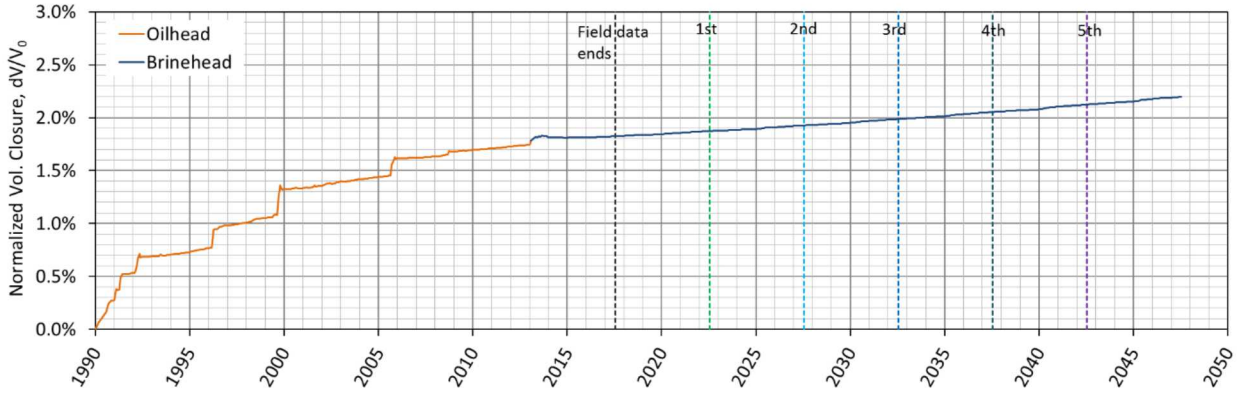

Figure 39. Predicted volumetric closure normalized to initial cavern volume of BC-20

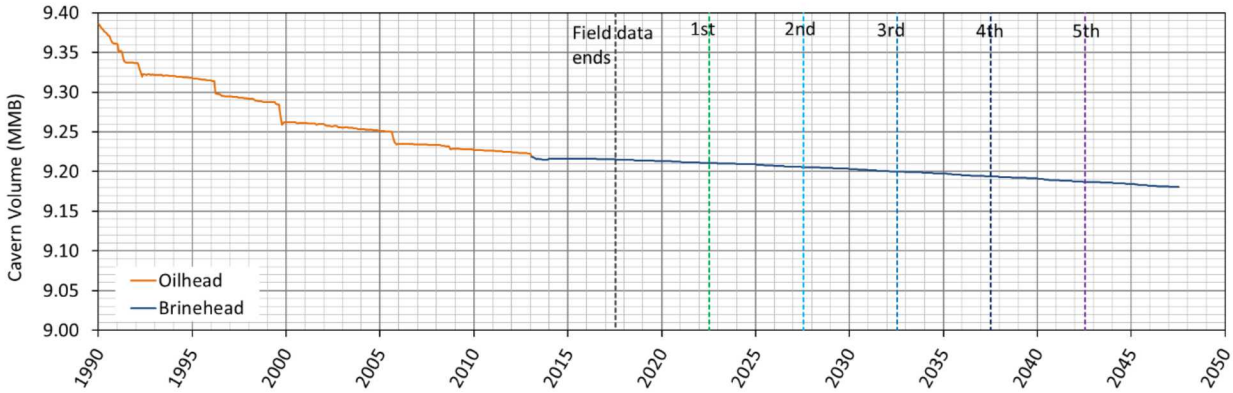

Figure 40. Predicted volumetric change of BC-20 due to salt creep closure over time

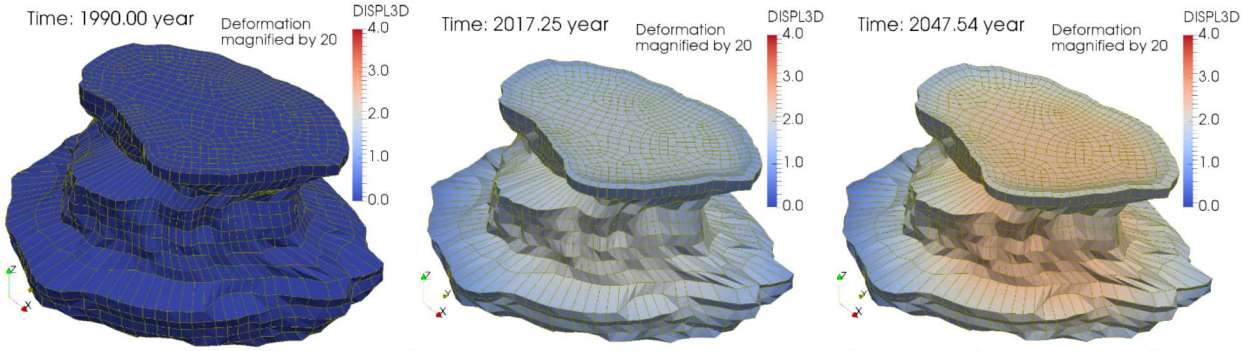

Figure 41. Predicted cavern deformations multiplied by 20x on 1/1/1990, 4/1/2017, and 7/17/2047 from left

7.2.2. Principal Stresses and Dilatant Damage Factor

There are two ways in which the salt surrounding the caverns can be damaged: by dilatant damage, resulting from micro-fracturing that increases permeability and the potential for crack propagation, and by tensile stresses that produces open fractures in the salt. A quick way to evaluate the potential for damage is by the use of history plots of the extreme values of dilatant damage factor (*DF*) and maximum principal stress (σ_1) in the salt surrounding the cavern through each of the drawdown leaching operation.

The edge pillar, the salt between the dome edge and BC-20, is shown for illustrative purposes in Figure 42. Figure 43 shows the predicted maximum σ_1, and minimum *DF* over time in the edge pillar. In the numerical analysis, σ_1 is calculated in every element in the salt dome at each time step. The maximum σ_1 means the maximum value among all σ_1 values calculated in all elements in a specific volume (in this case the edge pillar) at a specific time. In the plot, a positive value (+) indicates a tensile stress. In the similar manner, *DF* is calculated in every element in the salt dome at each time step. The minimum *DF* means the minimum value among all *DF* values calculated in all elements in a specific volume at a specific time. As mentioned in Section 6, when $DF \leq 1$, dilatant damage occurs.

Figure 43 (top) shows the predicted maximum σ_1 with time in the edge pillar before (orange curve) and after (blue curve) 2/7/2013 when BC-20 is filled fully with brine. The edge pillar is predicted to have experienced tensile since September 1999. The maximum σ_1 changes from

positive (tension) to negative (compression) in January 2018 and remains negative until the simulation ends. The predicted tensile stressed area was created in 1999 and disappears in 2018 as shown Figure 44.

Figure 43 (bottom) shows the predicted minimum *DF* with time in the edge pillar before (orange curve) and after (blue curve) 2/7/2013. The edge pillar is predicted to have experienced dilatant damage during the periods of 4/2/1996 8/1/1996, 9/19/1999–11/19/1999, 6/12/2002–7/13/2002, 10/11/2002–11/17/2005, 6/2/2008–10/3/2013, and 5/3/2014–2/1/2016. The minimum *DF* changes from less than one (damaged) to larger than one on 2/1/2016, and is predicted to remain larger than one throughout the remainder of the simulation, i.e. the edge pillar remains in a non-dilatant state after February 2016.

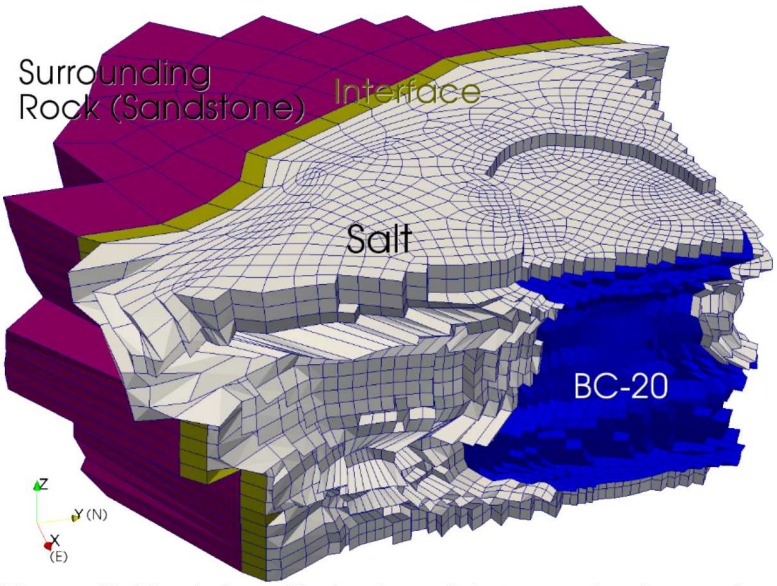

Figure 42. The 'edge pillar' – the salt between the dome edge and cavern 20

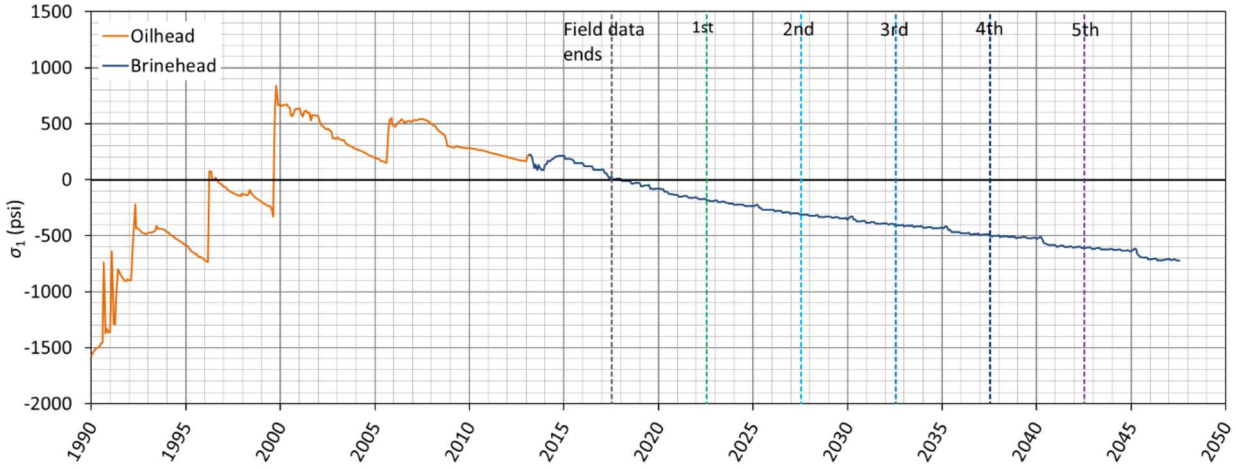

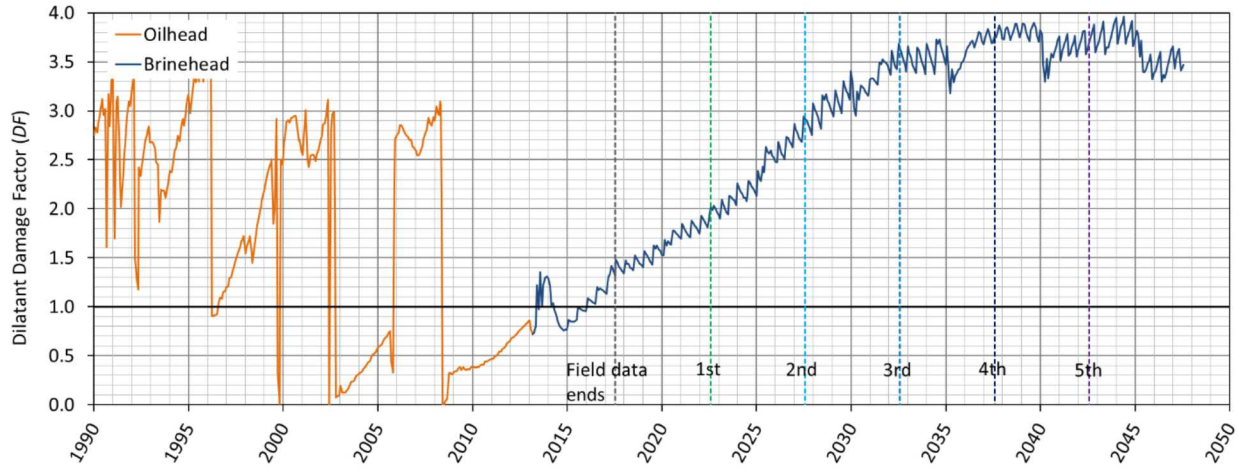

Figure 43. Predicted maximum σ_1 (top) and minimum dilatant damage factor (*DF*) over time in the salt between dome edge and BC-20.

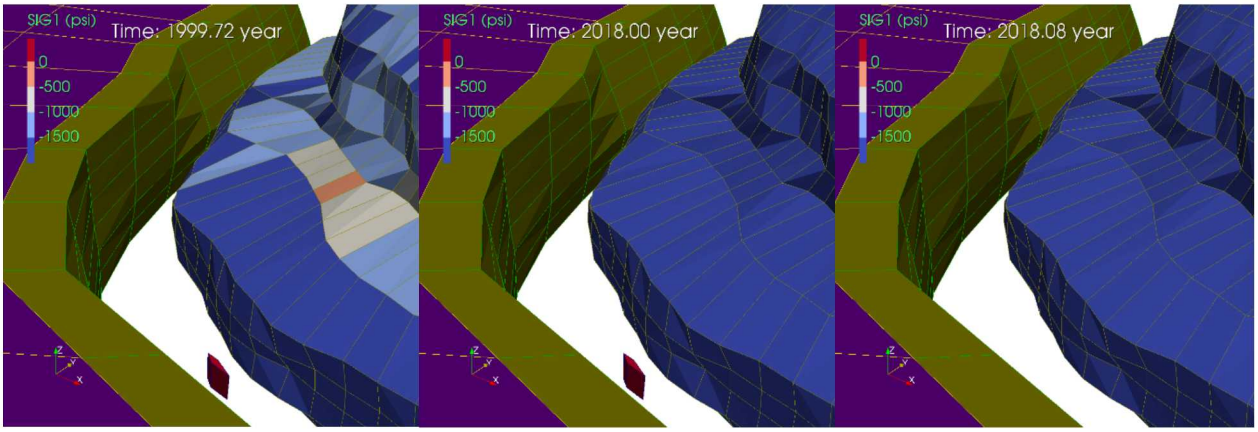

Figure 44. Plots of σ_1 on specific dates for normal operation. Areas in a tensile stress state are shown in red. To show the tensile stressed area in red clearly, the salt between the dome edge and Cavern 20 is omitted.

The initiation of tensile stress and dilatant damage ($DF \leq 1$) are predicted to occur on the same date (9/19/1999) as shown in Figure 43. The element in which both tensile stress and dilatant damage state, is located at -4080 ft depth in the edge pillar as shown Figure 45. The cavern wall is at its closest distance to the dome edge at this location.

The element in tensile stress state appears at time 1999.72 (Figure 45). The jumps of σ_1 appear when the wellhead pressures drop suddenly according to the simulated pressure history shown in Figure 26. On the other hand, *DF* becomes larger than 1, a non-dilating stress state, when the wellhead pressure returns to the normal operation pressure at time 1999.89 as shown in Figure 46, the stress condition of the element no longer predicts dilatant damage even though it is still in tensile state. This implies there is no additional creation of micro-cracking and increase in porosity/permeability under this condition. However, the fact that the element remains under tensile stress is extremely concerning.

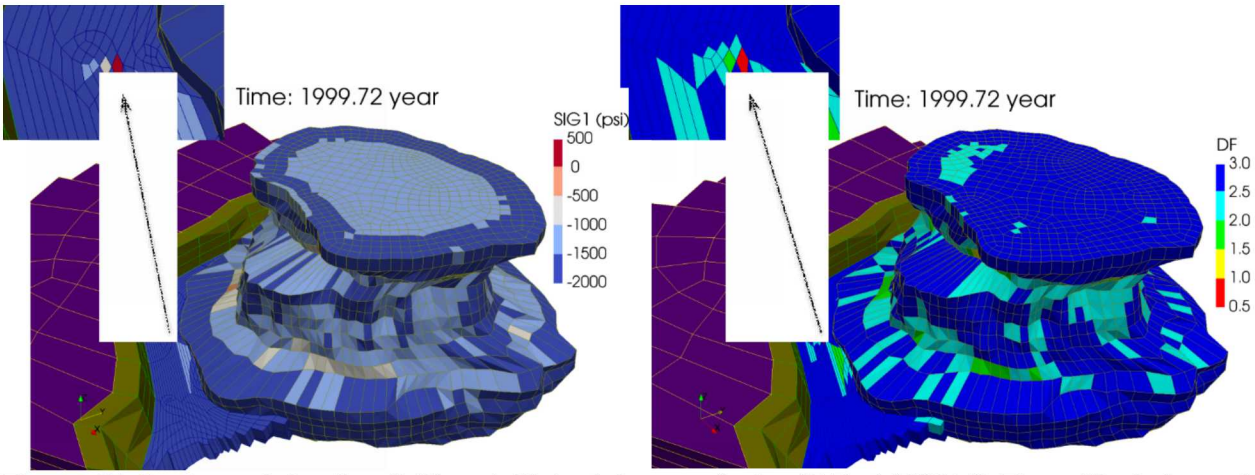

Figure 45. Contour plots of σ_1 (left) and dilatant damage factor (*DF*) at 1999.72. The critical element, which is in both a tensile and dilatant damage stress condition, is located in the salt between dome edge and BC-20 at elevation -4080 ft.

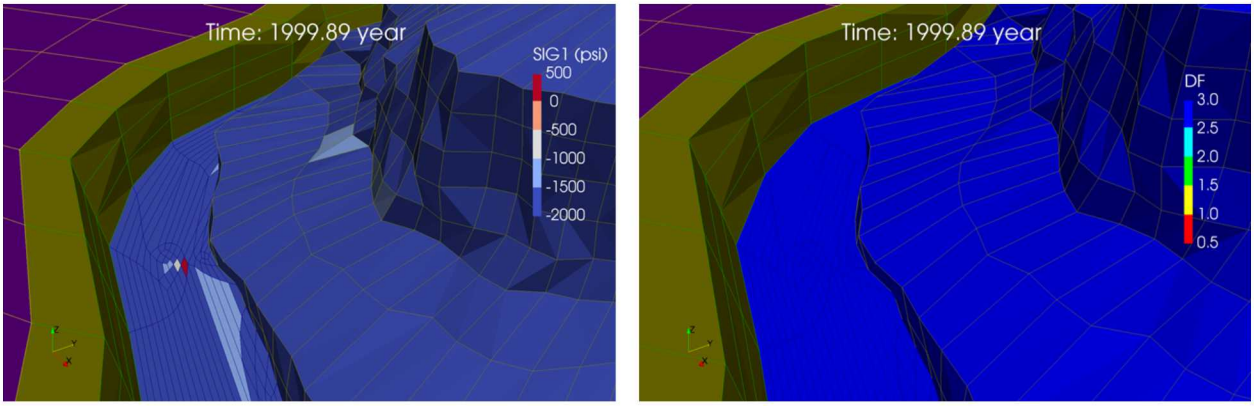

Figure 46. Contour plots of σ_1 (left) and dilatant damage factor (*DF*) at 1999.89. The critical element spotlighted in Figure 45 remains in tension (left), however the dilatant damage state has disappeared (right).

Figure 47 shows the predicted maximum σ_1, and minimum *DF* over time in the cavern skin layer surrounding BC-20 as shown Figure 48. The cavern layer skin is the one element thick layer of salt elements surrounding the cavern, comprising the roof, wall, and floor of BC-20. The cavern skin is in compression and non-dilatant states occur until the simulation ends. This is in contrast to the condition of the edge pillar that has been in tension and/or dilatancy producing states since 9/19/1999. This means that structural failure is more likely to occur in the edge pillar rather than cavern skin due to the cavern shrinkage.

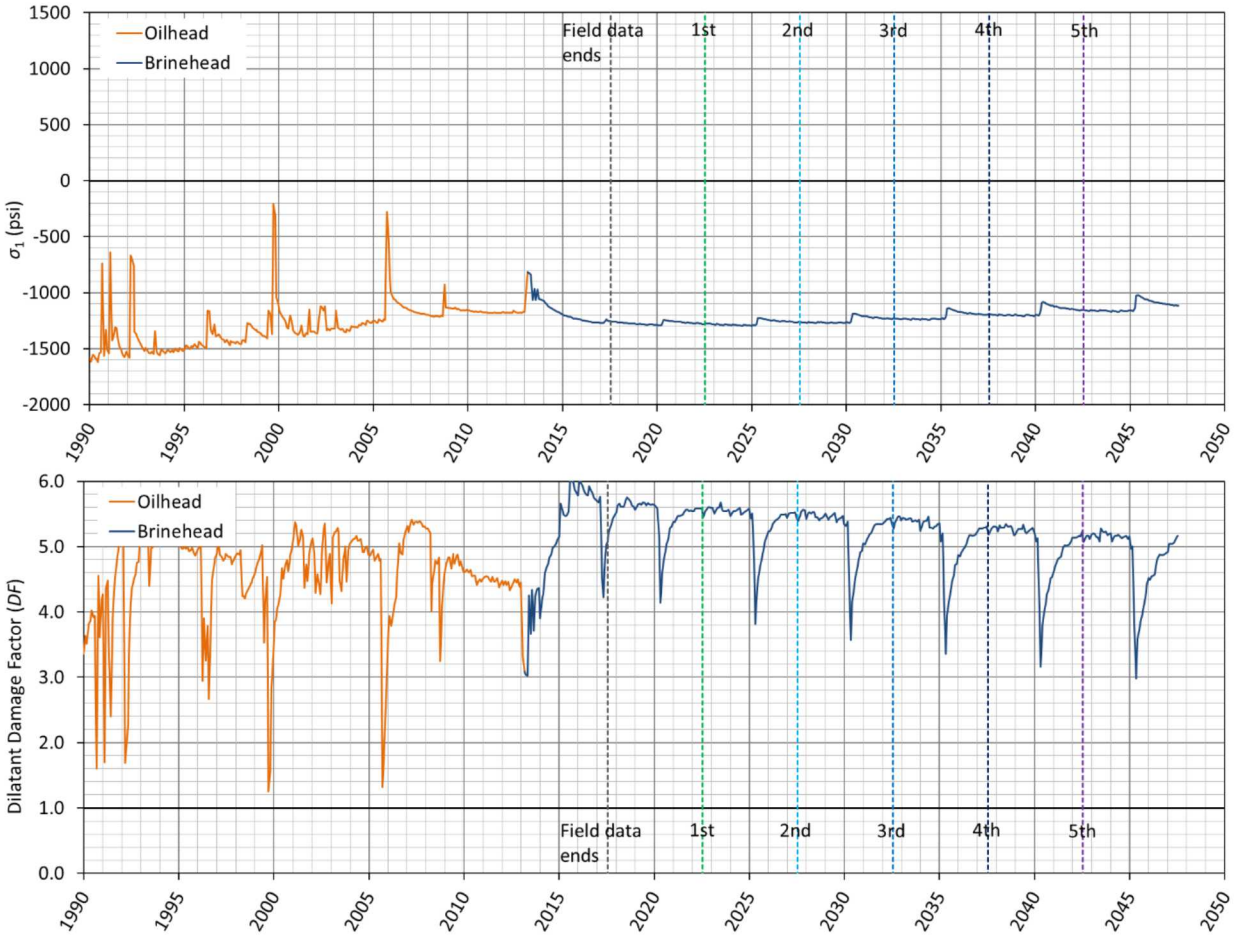

Figure 47. Predicted maximum σ_1 (top) and minimum dilatant damage factor over time in the cavern skin layer surrounding BC-20 cavity

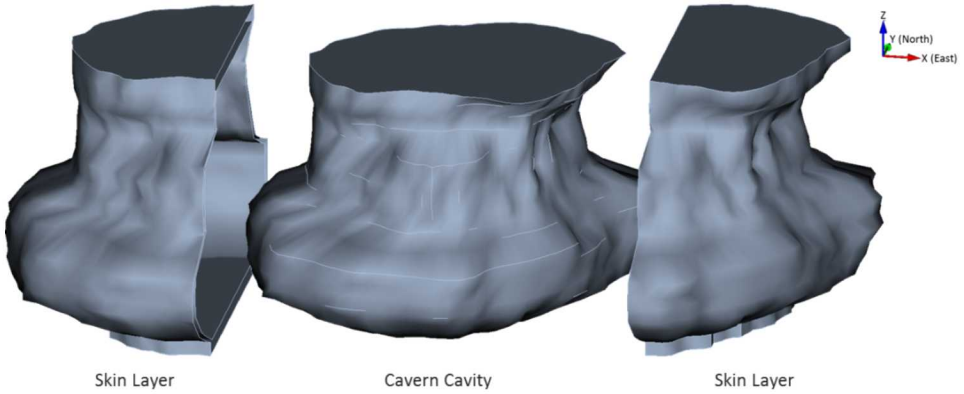

Figure 48. BC-20 cavern cavity and salt skin layer

7.3. Abandoned Cavern 4

7.3.1. Caprock Roof

Figure 49 shows the predicted maximum σ_1 over time in the caprock roof of BC-4 as shown in Figure 14. Note that the times labelled 1st, 2nd, …., 5th in the plots means six SPR cavern's assumed drawdown leach start dates, not for BC-4. In the numerical analysis, σ_1 is calculated in every element in the salt dome at each time step. The maximum σ_1 means the maximum value among all σ_1 values calculated in all elements in a specific volume (in this case the caprock roof) at a specific time. In the plot, a positive value (+) indicates a tensile stress. The caprock roof is predicted to be in compression states ($\sigma_1 < 0$) until the simulation ends (7/17/2047). However, σ_1 tends to continually increase toward zero. This implies that the roof could become structurally unstable some time after 2047. Figure 50 shows the predicted contour plots of σ_1 in 1990, 2012, 2017, and 2047. The structurally weakest area is located at the middle of the M-shape of the south side of the roof. The weakest area is still in compressive stress state until 2047. Therefore, the model indicates that the caprock roof may not collapse until 2047.

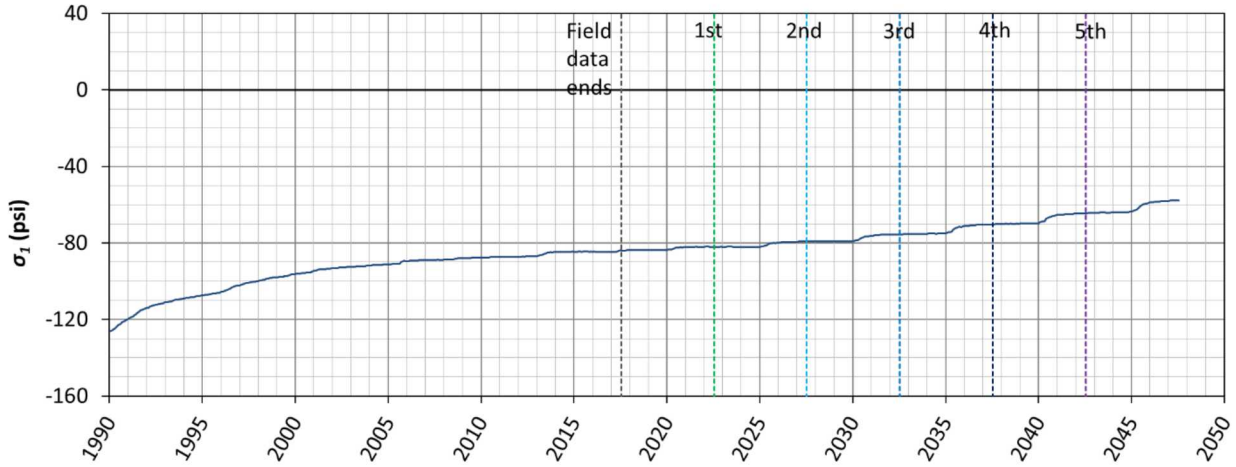

Figure 49. Predicted maximum σ_1 over time in the caprock roof of BC-4

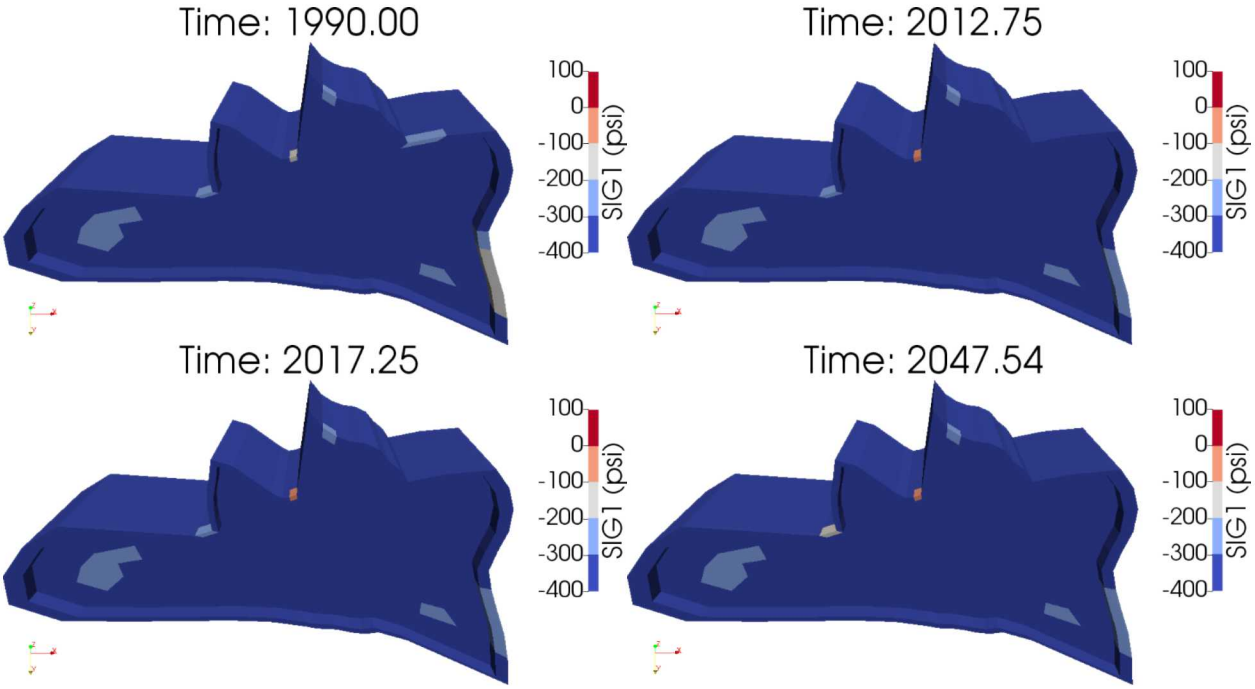

Figure 50. Contour plots of σ1 in the caprock roof as shown Figure 14 (look up view) on specific dates. Areas in tensile stress state must be shown in red (σ1>0), but the red area does not appear until 2047.54 years

7.3.2. Comparison of BC-4 with BC-7

Figure 51 shows the contour plots of σ_1 on the base of the caprock predicted for 1990, 2009, 2028, and 2047. The caprock overlying BC-4 is predicted to be in a compressive stress state ($\sigma_1 < 0$) until the simulation ends (7/17/2047), while the caprock surrounding BC-7 is predicted to be in a tensile stress state ($\sigma_1 > 0$) from the simulation starts (1/1/1990). The stress state in the roof of BC-7 is predicted to be larger than 600 psi, i.e. large tensile stresses distribute around the perimeter of BC-7. This tensile stress in caprock, in combination with the roof of BC-7 extending into the caprock and the absence of pressurization of the cavern's brine, probably induced the tensile failure on the roof of BC-7 that caused the cavern to collapse in 1954. Other caverns within the perimeter of the caprock where tensile stresses are predicted have not suffered the same fate due to a combination of the existence of a salt back above the caverns, more preferable cavern geometries, and active pressurization of the caverns. The compressive stressed area ($\sigma_1 < 0$) surrounding BC-4 in dark blue gradually decreases with time. This trend is likely to continue over the years as the BC caverns close and resulting subsidence accumulates. The computational model somewhat idealizes the condition of the caprock in the roof of BC-4, so uncertainty will always exist in its condition. Therefore, even as the model provides justifiable reason to believe that a roof collapse of BC-4 is not imminent, we need to continue monitoring the cavern roof integrity. (This need is particularly true when including the potential for salt falls, as discussed in the next section.)

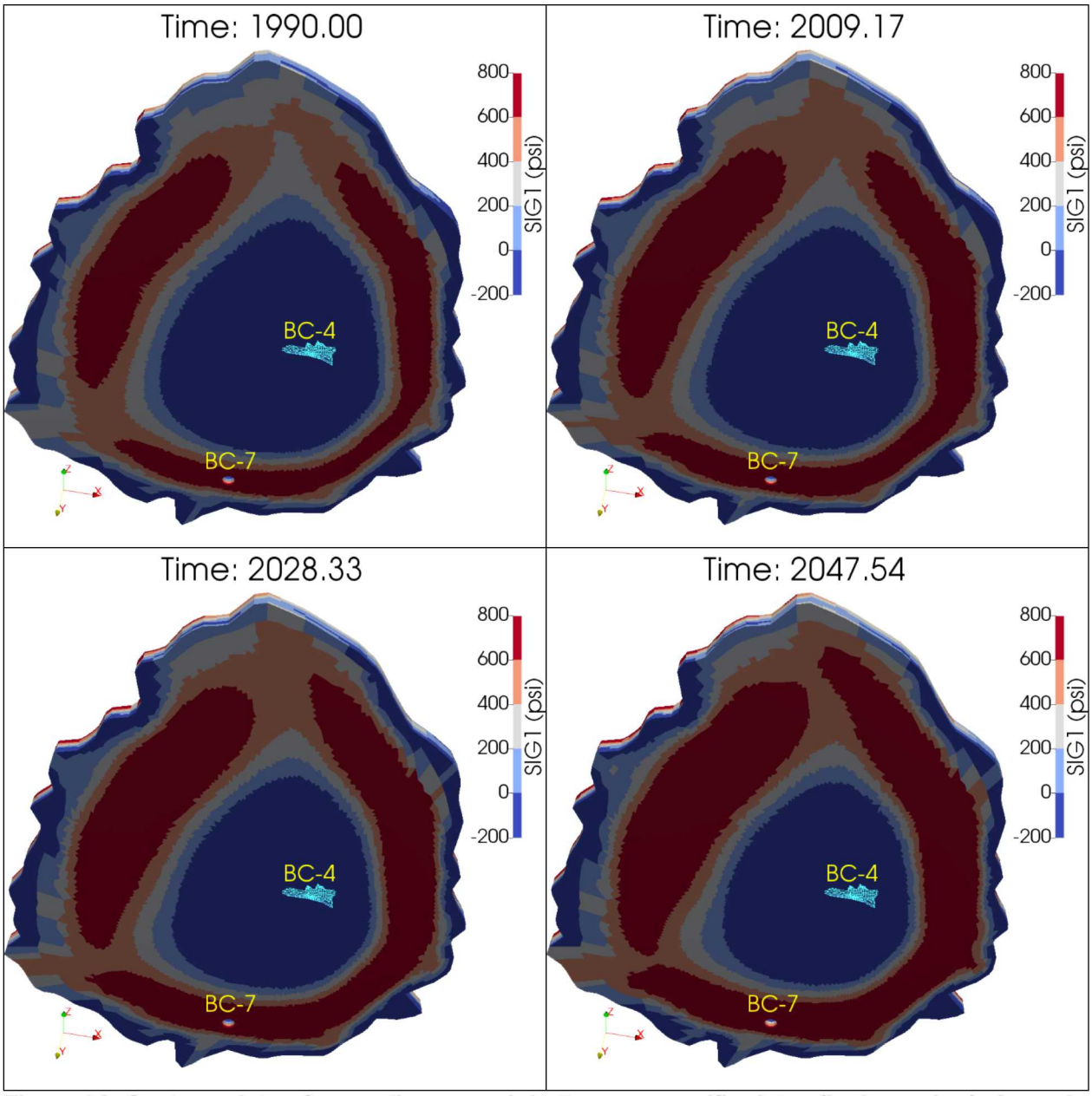

Figure 51. Contour plots of σ_1 on the caprock bottom on specific dates (look up view). Areas in compressive stress state are shown in dark blue (σ_1 < 0). The compressive stressed area surrounding BC-4 decreases with time. The area surrounding BC-7 is in tensile stress state from the simulation starts.

7.3.3. Salt Body of BC-4

Figure 52 shows the predicted volumetric decrease in storage volume in BC-4 over 57 years. The initial cavern cavity volume (meshed volume in the model) was 6.123 MMB on 1/1/1990 and is predicted to be 6.113 MMB on 7/17/2047. The cavern volume decreases by 0.16% over 57 years. Note again that the 1st, 2nd, …., 5th in the plots means six SPR cavern's assumed drawdown leach start dates, not for BC-4.

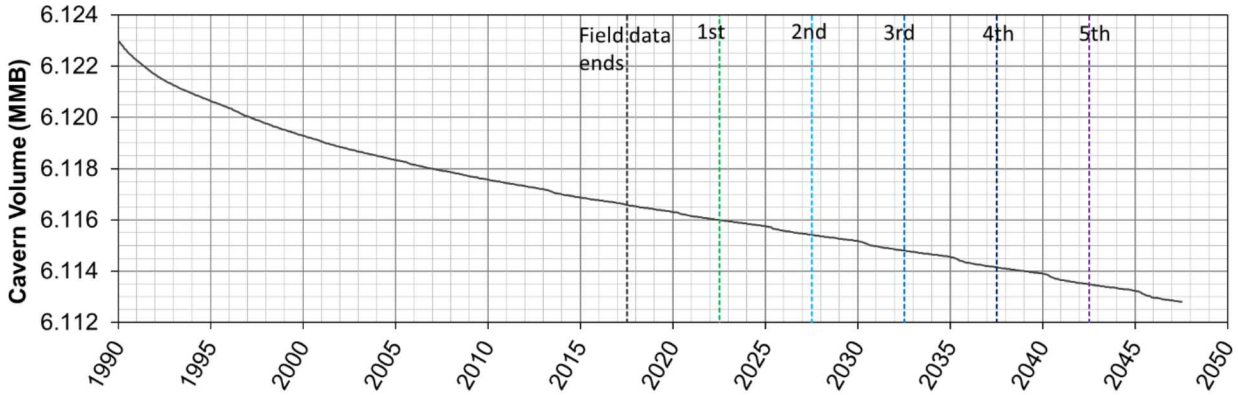

Figure 52. Predicted volumetric change of BC-4 due to salt creep closure over time

As mentioned in Section 6, there are two ways in which the salt surrounding the caverns can be damaged: by dilatant damage resulting from micro-fracturing that increases permeability and the potential for crack propagation; and by tensile stresses that produces open fractures in the salt. A quick way to evaluate the potential for damage is by the use of history plots of the extreme values of dilatant damage factor (*DF*) and maximum principal stress (σ_1) in the salt surrounding the cavern.

Figure 53 shows the predicted maximum σ_1, and minimum *DF* over time in the salt skin layers as shown in Figure 14. In the numerical analysis, σ_1 is calculated in every element in the salt dome at each time step. The maximum σ_1 means the maximum value among all σ_1 values calculated in all elements in a specific volume (the salt skin layers in this case) at a specific time. In the plot, a positive value (+) indicates a tensile stress. In the similar manner, *DF* is calculated in every element in the salt dome at each time step. The minimum *DF* means the minimum value among all *DF* values calculated in all elements in a specific volume at a specific time. When $DF \leq 1$, dilatant damage occurs.

Figure 53 (top) shows the predicted maximum σ_1 with time in the salt skins. The salt skins is predicted to have experienced tensile since the simulation starts. The predicted tensile stressed areas in red as shown Figure 54 were created in the upper cavern in 1990. The locations of the tensile stressed areas change with each specific date. The potential of tensile failure exists in the areas, i.e. the salt fall may occur at the areas.

Figure 53 (bottom) shows the predicted minimum *DF* with time in the salt skin layers. The salt skin layers are predicted to have experienced dilatant damage during the entire simulation period except 9/1/2011 6/4/2013. The predicted dilatant damaged areas in red as shown Figure 55 were created in the upper cavern in 1990, they disappear in 2012, and reappear again in 2017. The locations of the damaged areas change with each specific date like the tensile stressed areas. The potential of creation of micro-cracking and increase in porosity/permeability exists in the areas.

Those places overlapped with tensile stressed areas in Figure 54 and dilatant damaged areas in Figure 55 are under the condition of both tensile failure and micro-cracking. The possibility of a salt fall is predicted to be high there. The potential for salt falls is important for the overall integrity of the cavern. Because these salt falls will likely occur from the near-roof portions of the cavern, they may over time degrade the roof and accelerate the transition from compressive to tensile stresses in the caprock roof. The computational model does not include the effects of

salt falls in the evolution of stress around the cavern. Therefore, it is difficult to predict with certainty how and when the salt falls may eventually hasten cavern roof instability. Again, the model indicates that any sort of roof collapse for BC-4 is not imminent; however, the uncertainty due to salt falls illustrates the importance of continued monitoring of the area around BC-4 for behavior such as subsidence and tilt which may indicate a change in the cavern's integrity status.

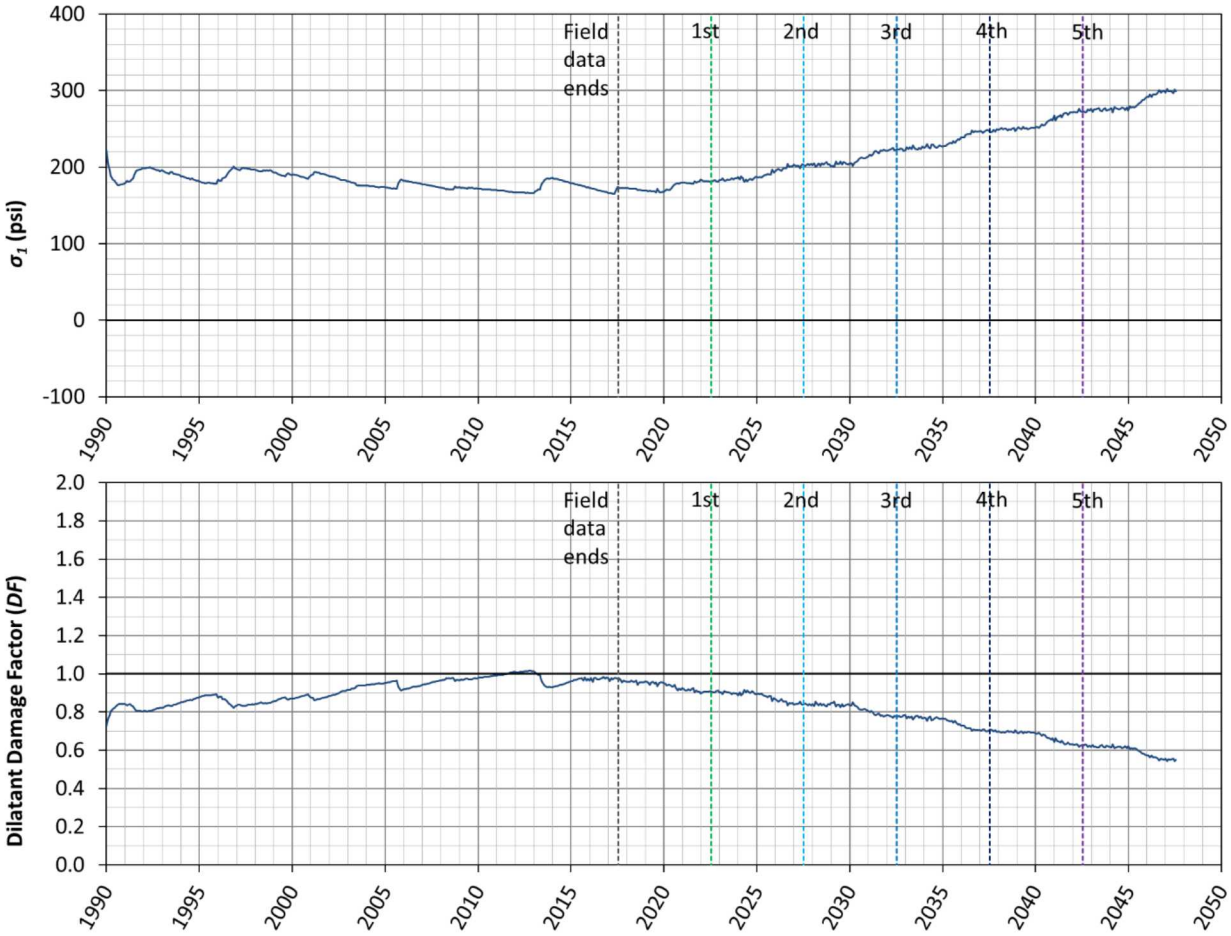

Figure 53. Predicted maximum σ_1 (top) and minimum dilatant damage factor (*DF*) over time in the salt surrounding BC-4.

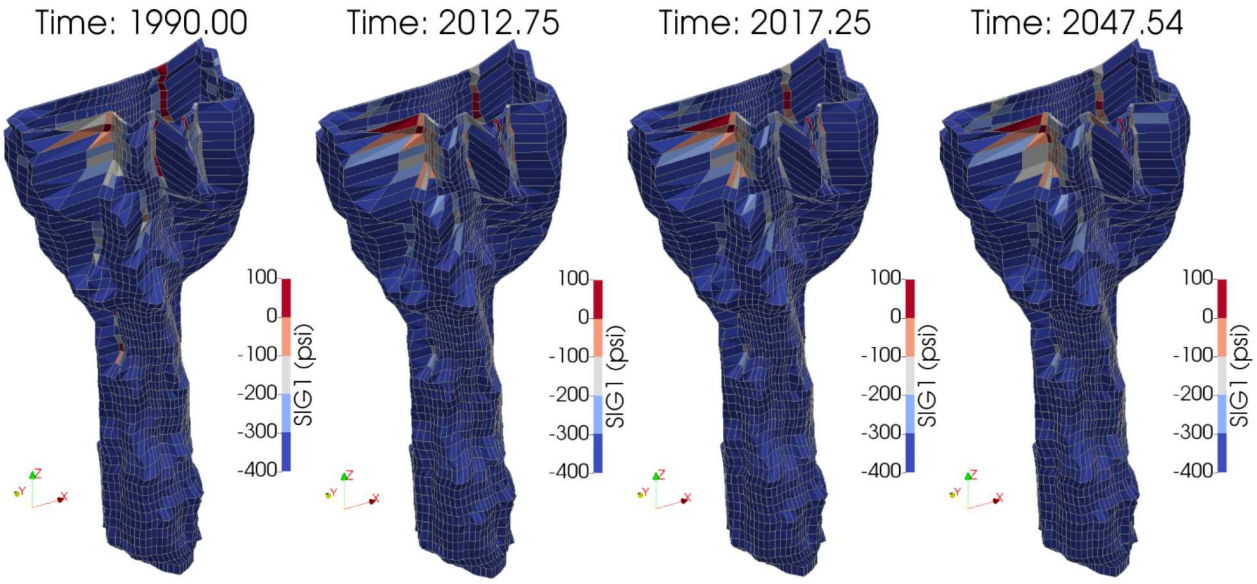

Figure 54. Contour plots of σ_1 on the skin of BC-4 on specific dates. Areas in tensile stress state are shown in red (σ_1>0)

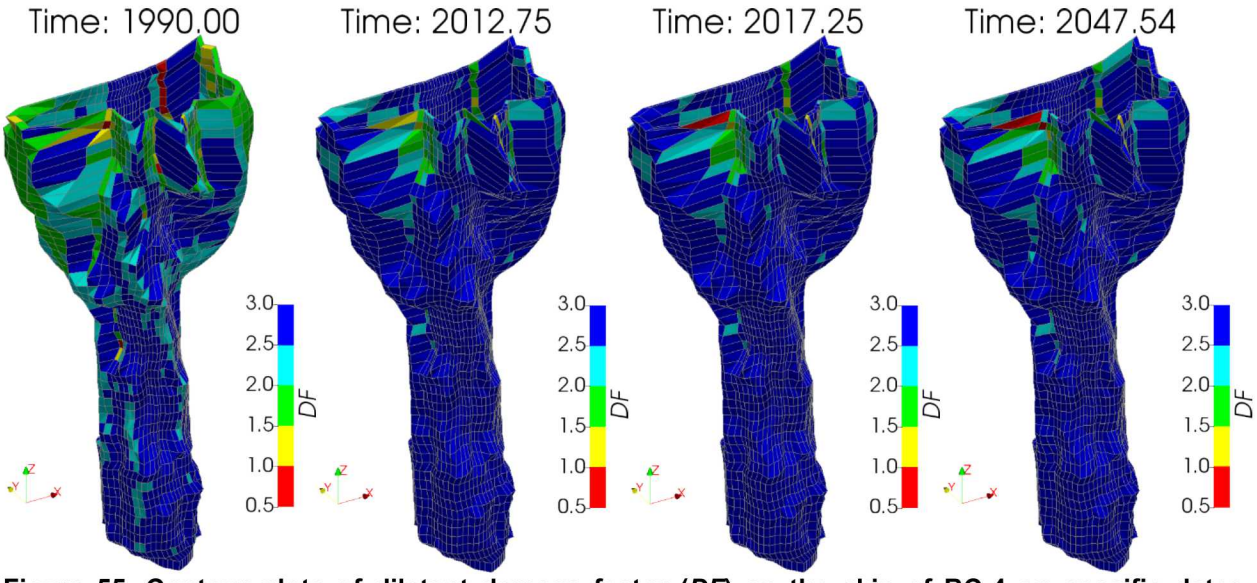

Figure 55. Contour plots of dilatant damage factor (*DF*) on the skin of BC-4 on specific dates. Areas in dilatant damaged state are shown in red (*DF* < 1)

8. SUMMARY AND CONCLUSIONS

Geotechnical concerns arise due to the close proximity of some of the caverns to each other (e.g., Caverns 15 and 17) or to the edge of salt dome (e.g., Cavern 20). There are nine abandoned caverns, one of which collapsed in 1954 (Cavern 7) and another (Cavern 4) which is believed to be in a quasi-stable condition. This report provides explanations for these geotechnical concerns.

The structural integrity of the pillar between BC-15 and 17 is examined. No salt failure due to the existence of tensile stress is expected through 2045. However, the microcrack area increases with time, especially, at the chimney area of BC-17. Both caverns are normally operated as a gallery, in which case they are depressurized simultaneously. If an unexpected unbalanced internal pressurization of two caverns occurs, the structural instability of the pillar between them may increase rapidly. Therefore, it is important to continue carefully monitoring the cavern's behavior such as an unexpected pressure drop. The analyses herein indicate that one drawdown leach could be allowed from a geomechanics perspective.

The possibility of a loss in structural integrity of BC-20 is examined in the salt between the dome edge and the cavern. BC-20 has been emptied of oil and filled fully with brine since 2/7/2013. Since that date the wellhead pressure data recorded at the brine-side wellbore, and the weight of the brine-filled column in the wellbore, is the mechanism that controls the pressure in the cavern. The results from this analysis indicate that if we keep the new normal operation brine-side wellhead pressure, the edge pillar has no predicted risk of structural instability in the form of tensile failure and/or dilatant damage. The edge pillar is predicted to have experienced tensile since September 1999 but the small tensile stressed area is predicted to disappear in 2018. Even though BC-20 is no longer used as an SPR cavern and is filled with brine rather than oil since 2/7/2013, we need to continually monitoring the cavern for signs of a loss of integrity. A sudden decrease in cavern pressure will be indicative of a brine leak. Once a leak occurs, the cavern may shrink rapidly and possibly create stress conditions conducive to a collapse. Therefore, the active wells must be tested with the mechanical integrity tests (MIT) periodically.

BC-4 is currently filled with brine and will not hold pressure at the wellhead. The cavern extends upward into the caprock and has no salt roof. The results from the analysis herein indicate that the cavern roof in the caprock layer has no predicted risk of structural stability in the form of tensile failure for up to 30 years. The computational model somewhat idealizes the condition of the caprock in the roof of BC-4, so uncertainty exists in its actual condition. Therefore, even as the model provides justifiable reason to believe that a roof collapse of BC-4 is not imminent, we need to continue monitoring the cavern roof integrity. The salt surrounding BC-4 is predicted to have experienced tensile and dilatant damaged from the start of the simulation (1990). The potential for salt falls is important for the overall integrity of the cavern. Because these salt falls will likely occur from the near-roof portions of the cavern, they may over time degrade the roof and accelerate the transition from compressive to tensile stress in the caprock roof. The uncertainty due to salt falls illustrates the importance of continued monitoring of the area around BC-4 for behavior such as subsidence and tilt which may indicate a change in the cavern's integrity status.

9. REFERENCES

Ballard, S. and Ehgartner, B.L. (2000) *CAVEMAN Version 3.0: System for SPR Cavern Pressure Analysis,* SAND2000-1751, Sandia National Laboratories, Albuquerque, NM 87185-0750.

Carmichael, R.S. (1984) *CRC Handbook of Physical Properties of Rocks*, CRC (Chemical Rubber Company) Press, Inc. Boca Raton, Fl.

Dames and Moore (1978) *Determination of Physical Properties of Salt and Caprock, Bayou Choctaw Salt Dome, Iberville Parish, Louisiana:* in PB/KKB, Inc., 1978f, *Salt Dome Geology and Cavern Stability, Bayou Choctaw, Louisiana*, Final Report, Appendix, prepared for the U.S. Department of Energy, August.

DeVries, K.L., K. D. Mellegard, and G.D. Callahan (2003) Laboratory Testing in Support of Bedded Salt Failure Criterion, RESPEC, Technical Paper of *Solution Mining Research Institute, Fall 2003 Meeting 5-8 October 2003, Chester, United Kingdom, England*.

Ehgartner, B.L. and Sobolik, S.R. (2002) *3-D Cavern Enlargement Analyses*, SAND2002-0526, Sandia National Laboratoires, Albuquerque, NM 87185-0706.

Ehgartner, B.L. (2007). *Re-examination of Bayou Choctaw Cavern 4*. Sandia National Laboratories, Albuquerque, NM, USA. U.S. Strategic Petroleum Reserve. August 8, 2007.

Hoffman, E. L. (1992) *Investigation of Analysis Assumptions for SPR Calculations*, memo to J. K. Linn, Sandia National Laboratories, Albuquerque, New Mexico, February 7, 1992.

Hogan, R.G. (1980) *Strategic Petroleum Reserve (SPR) Geological Site Characterization Report Bayou Choctaw Salt Dome*. SAND80-7140. Sandia National Laboratories, Albuquerque, NM.

Ingraham, M.D., S.T. Broome, S.J. Bauer, P.C. Barrow and G.M. Flint (2014) *Geomechanical Testing of Bayou Choctaw 102B Core for SPR Analysis*, SAND2014-1459, Sandia National Laboratories, Albuquerque, New Mexico.

LADNR (2013) *Directive on Salt Cavern Locations in Relation to Periphery of Salt Stock*. State of Louisiana. Department of Natural Resources. Baton Rouge, LA 70804-9275. January 30, 2013.

Lord, D.L., S.R. Sobolik, B.Y. Park and D.K. Rudeen (2013) *Impacts of First Water Drawdown on SPR Low P/D Caverns*, Letter Report to Gilbert Shank DOE PMO dated December 20, 2013. Geotechnology & Engineering, Sandia National Laboratories. U.S. Strategic Petroleum Reserve.

Lord, A.S., D.L. Lord, B.L, B.L. Roberts, B.Y. Park, and G. Bettin (2015) *Bayou Choctaw Abandoned Cavern 4 Stability Analysis, 2014 Update*. SAND2015-0049, Official Use Only, Law Enforcement, Sandia National Laboratories, Albuquerque, New Mexico.

LSU (2013) *Blue Ribbon Commission Initial Technical Briefing*, Presentation slides dated April 5, 2013.

Munson, D.E. (1979) *Preliminary Deformation-Mechanism Map for Salt (with Application to WIPP)*, SAND70-0079, Sandia National Laboratories, Albuquerque, New Mexico.

Munson, D.E. and P.R. Dawson (1982) *A Transient Creep Model for Salt during Stress Loading and Unloading.* SAND82-0962, Sandia National Laboratories, Albuquerque, New Mexico.

Munson, D.E., A.F. Fossum, and P.E. Senseny (1989) *Advances in Resolution of Discrepancies between Predicted and Measured in Situ WIPP Room Closures.* SAND88-2948, Sandia National Laboratories, Albuquerque, New Mexico.

Munson, D.E. (1998) *Analysis of Multistage and Other Creep Data for Domal Salts*, SAND98-2276, Sandia National Laboratories, Albuquerque, New Mexico.

Neal, J.T., T.R. Magorian, K.O. Byrne and S. Denzler (1993). *Strategic Petroleum Reserve (SPR) Additional Geological Site Characterization Report Bayou Choctaw Salt Dome, Louisiana*. SAND92-2284. Sandia National Laboratories, Albuquerque, NM.

Park, B.Y., B.L. Ehgartner, and M.Y. Lee (2006) *Three Dimensional Simulation for Bayou Choctaw Strategic Petroleum Reserve (SPR)*, SAND2006-7589, Sandia National Laboratories, Albuquerque, New Mexico.

Park, B.Y. and B.L. Ehgartner (2008) *Expansion Analyses of Strategic Petroleum Reserve (SPR) in Bayou Choctaw Salt Dome,* SAND2008-6408, Sandia National Laboratories, Albuquerque, New Mexico.

Park, B.Y. and B.L. Ehgartner (2010) *Expansion Analyses of Strategic Petroleum Reserve in Bayou Choctaw – Revised Locations,* SAND2010-3350, Sandia National Laboratories, Albuquerque, New Mexico.

Park, B. Y. and B. L. Ehgartner (2011) *Allowable Pillar to Diameter Ratio for Strategic Petroleum Reserve Caverns*. Unlimited Release SAND2011-2896, Sandia National Laboratories, Albuquerque, NM 87185. U.S. Strategic Petroleum Reserve.

Park, B.Y. (2014) Interbed Modeling to Predict Wellbore Damage for Big Hill Strategic Petroleum Reserve. *Journal of Rock Mech Rock Eng (2014) 47:1551-1561.* DOI 10.1007/s00603-014-0572-2

Park, B.Y. and B.L. Roberts (2015) *Construction of Hexahedral Elements Mesh Capturing Realistic Geometries of Bayou Choctaw SPR site*, SAND2015-7458, Sandia National Laboratories, Albuquerque, New Mexico.

Park, B.Y. (2017a) *Geomechanical Simulation of Bayou Choctaw Strategic Petroleum Reserve - Model Calibration*, SAND2017-2103, Sandia National Laboratories, Albuquerque, New Mexico.

Park, B.Y. (2017b) *Assessment of the Available Drawdowns for Oil Storage Caverns at the Bayou Choctaw SPR Site*, SAND2017-12757, Sandia National Laboratories, Albuquerque, New Mexico.

Park, B. Y., B.L. Roberts, and S.R. Sobolik (2017) Construction of hexahedral finite element mesh capturing realistic geometries of a petroleum reserve. *Journal of Finite Elements in Analysis and Design*, 135, 68–78. https://doi.org/10.1016/j.finel.2017.07.007

Park, B. Y., S.R. Sobolik, and C.G. Herrick (2018) Geomechanical Model Calibration Using Field Measurements for a Petroleum Reserve. *Journal of Rock Mechanics and Rock Engineering*, ISSN 0723-2632, https://doi.org/10.1007/s00603-017-1370-4

Price, R.H., W.R. Wawersik, O.W. Hannum, and J.A. Zirzow (1981) *Quasi-Static Rock Mechanics Data for Rock Salt from Three Strategic Petroleum Reserve Domes*, SAND81-2521, Sandia National Laboratories, Albuquerque, New Mexico, 46 pp.

Rautman, C.A., K.M. Looff, and J.B. Duffield (2009) *A Three-Dimensional Geometric Model of the Bayou Choctaw Salt Dome, Southern Louisiana, Using 3-D Seismic Data*, OUO SAND2009-1037, Sandia National Laboratories, Albuquerque, New Mexico.

Roberts, B.L. (2015) *BC dome seismic image*, E-mail from B.L. Roberts to B.Y. Park dated 2/5/2015. Sandia National Laboratories, Albuquerque, New Mexico.

Sobolik S.R., B.Y. Park, D.L. Lord, B. Roberts, and D.K. Rudeeen (2014) *Current Recommendations Regarding ECP PM-00449, Baseline Remaining Drawdowns for all SPR Caverns*. FY14 Sandia Geotechnical Support for U.S. Strategic Petroleum Reserve, Letter Report to Lisa Nicholson dated May 9, 2014., Sandia National Laboratories, Albuquerque, NM.

Todd, J.L. and K.H. Smith (1988). *Collapse Warning System for Bayou Choctaw Cavern 4*. SAND88-1510. Sandia National Laboratories, Albuquerque, NM USA.

The Aerospace Corporation (1980) *Preliminary Draft – Bayou Choctaw Cavern Foru subsidence Comparative Risk Assessment – Strategic Petroleum Reserve*, October 30, 1980, Los Angeles, California, 90009.

Intentionally left blank

DISTRIBUTION

External Distribution

Electronic copies to:

Wayne Elias (wayne.elias@hq.doe.gov)
for distribution to DOE SPR Program Office, Washington, D.C.
U.S. Department of Energy
Office of Fossil Energy
Forrestal Building
1000 Independence Ave., SW
Washington, DC 20585

Diane Willard (diane.willard@spr.doe.gov)
for distribution to DOE and FFPO SPR Project Management Office, New Orleans, LA.
U.S. Department of Energy
Strategic Petroleum Reserve Project Management Office
900 Commerce Road East
New Orleans, LA 70123

Sandia Distribution

Print copy				
0	MS0735	E. K. Webb	8860	(electronic copy)
0	MS0706	Anna C. Snider Lord	8862	(electronic copy)
0	MS1033	M. D. Ingraham	8862	(electronic copy)
10	MS0751	B. Y. Park	8862	(print and electronic copies)
0	MS0751	D. B. Hart	8865	(electronic copy)
0	MS0751	B. L. Roberts	8862	(electronic copy)
0	MS0706	D. L. Lord	8862	(electronic copy)
0	MS0751	S. R. Sobolik	8862	(electronic copy)
5	MS0750	C. L. Kirby	8862	(print and electronic copies)
0	MS0751	C. G. Herrick	8864	(electronic copy)
0	MS1395	H. D. Park	8881	(electronic copy)
0	MS0899	Technical Library	9536	(electronic copy)

Intentionally Blank


Sandia National Laboratories